

1 **Thrusts control the thermal maturity of accreted sediments**

2 Utsav Mannu^{1,4,5}, David Fernández-Blanco², Ayumu Miyakawa³, Taras Gerya⁴, and Masataka Kinoshita⁵

3 ¹Discipline of Earth Sciences, Indian Institute of Technology, Gandhinagar, India

4 ²Barcelona Center of Subsurface Imaging, Institut de Ciències del Mar (ICM-CSIC), Barcelona, Spain;

5 ³Geological Survey of Japan, AIST

6 ⁴Institute of Geophysics, ETH Zurich

7 ⁵Earthquake Research Institute, UTokyo

8 *Correspondence to:* Utsav Mannu (utsav.mannu@iitgn.ac.in)

9

10

11

12

13

14

15

16

17

Style Definition: Normal: English (United States), Don't hyphenate

Style Definition: Heading 2: Font: 11 pt, Italic, English (United States), Space Before: 0 pt, After: 0 pt, Line spacing: Double, Keep lines together, Don't hyphenate

Style Definition: Heading 3: English (United States), Don't hyphenate

Style Definition: Heading 4: English (United States), Don't hyphenate

Style Definition: Comment Reference

Style Definition: Header: English (United States), Suppress line numbers, Don't hyphenate

Style Definition: Footer: English (United States), Suppress line numbers, Don't hyphenate

Style Definition: Comment Text: English (United States), Don't hyphenate

Style Definition: Comment Subject: English (United States), Don't hyphenate

Formatted: Font: 11 pt

Formatted: Font: 11 pt

Formatted: Line spacing: Multiple 1.39 li

Formatted: Width: 8.27"

Formatted: Font: 11 pt

Formatted: Font: 11 pt, English (United Kingdom)

Formatted: Font: 11 pt

Formatted: Font: 11 pt, Spanish (Spain)

Formatted: Font: 11 pt

Formatted: Font: 11 pt

Formatted: Font: 11 pt, English (United Kingdom)

Formatted: Border: Top: (No border), Bottom: (No border), Left: (No border), Right: (No border), Between : (No border)

Formatted: Font: 11 pt

Formatted: Font color: Auto

Formatted

±1

18

19

20 **Abstract.**

21 Thermal maturity assessments of hydrocarbon-generation potential and thermal history rarely consider how upper-
22 plate structures developing during subduction influence the trajectories of accreted sediments. Our
23 thermomechanical models of subduction support that thrusts evolving under variable sedimentation rates and
24 décollement strengths fundamentally influence the trajectory, temperature, and thermal maturity of accreting
25 sediments. This is notably true for the frontal thrust, which pervasively partitions sediments along a low and a high
26 maturity path. Our findings imply that interpretations of the distribution of thermal maturity cannot be detached
27 from accounts of the length and frequency of thrusts and their controlling factors. ~~Taking~~Our approach takes these
28 factors into consideration, ~~our approach and~~ provides a robust uncertainty estimate in maximum exposure
29 temperatures as a function of vitrinite reflectance and burial depth ~~thereby reducing~~. As a result, our models reduce
30 former inconsistencies between predicted and factual thermal maturity distributions in accretionary wedges.

31

32

33

34

35

36

37

38

39

40

41

42

Formatted: Font: 11 pt, English (United Kingdom)

Formatted: Font: 11 pt

Formatted: Font: 11 pt

Formatted: Font: 11 pt

Formatted: Font: 11 pt

Formatted: Font: 11 pt, English (United Kingdom)

Formatted: Font: 11 pt

Formatted: Font color: Auto

Formatted: Border: Top: (No border), Bottom: (No border), Left: (No border), Right: (No border), Between : (No border), Tab stops: Not at 3.13" + 6.27"

43
44
45
46
47
48
49
50
51

52 **1. Introduction**

53 Organic material transforms into coal, oil, and gas at rates primarily controlled by temperature(Quigley & Maekenzie,
54 1988). This transformation, critical for the hydrocarbon industry, is also useful to study the tectonic and
55 sedimentary evolution of basins and orogens (Tissot et al., 1987; Tissot & Welte, 2013; Waples, 1981). The extent of
56 this transformation in sediments, known as thermal maturity, can be measured as vitrinite reflectance, i.e., the
57 percentage of incident light reflected from the surface of vitrinite particles in those sediments (Burnham & Sweeney,
58 1989). Thermal maturity has been used to estimate the thermal evolution of igneous intrusions (Bostick & Pawlewicz,
59 1984) and seismic slip (Rabinowitz et al., 2020), the extent of diagenesis and low-grade metamorphism (Ferreiro
60 Mählmann & Le Bayon, 2016; Totten & Blatt, 1993), porosity, and compaction in basin sediments (Schmoker & Gautier,
61 1988), as well as, and the geothermal history of accreting material during subduction (A. Sakaguchi et al., 2011;
62 Underwood et al., 1992; Yamamoto et al., 2017) (e.g., Bostick and Pawlewicz, 1984; Rabinowitz et al., 2020; Fukuchi
63 et al., 2017; Kamiya et al. 2017).

64 Inferences on the geothermal history of subduction margins based on thermal maturity depend on the
65 trajectory followed by the accreting sediments (Miyakawa et al., 2019) (Miyakawa et al., 2019). Low-temperature,
66 high-pressure metamorphic rocks in the subduction wedge are often attributed to the pressure maxima that typically

Formatted: Font: 11 pt

Formatted: Font: 11 pt

Formatted: Font: 11 pt

Formatted: Font: 11 pt

Formatted: Font: 11 pt

Formatted: Font: 11 pt

Formatted: Font: 11 pt

Formatted: Font: 11 pt

Formatted: Font: 11 pt

Formatted: Font: 11 pt

Formatted: Font: 11 pt

Formatted: Font: 11 pt, English (United Kingdom)

Formatted: Font: 11 pt

Formatted: Font: 11 pt

Formatted: Font: 11 pt

Formatted: Font color: Auto

Formatted: Border: Top: (No border), Bottom: (No border), Left: (No border), Right: (No border), Between :

(No border), Tab stops: Not at 3.13" + 6.27"

67 predate the temperature maxima in ~~accreted~~ ~~sediments~~ ~~aeereted-undergoing diagenesis~~ in the wedge (Platt, 1993);
68 (Ruh, 2020). However, ~~numerical models (Ruh, 2020b) and field observations (Giunchi & Ricard, 1999) have indicated the~~
69 existence of complicated patterns in sediment trajectories. ~~is supported by numerical models and field observations~~
70 (Giunchi & Ricard, 1999). As the orogenic wedge evolves, sediments accreting along different paths reach different
71 depths and velocities and are exposed to different regional peak temperatures. Miyakawa (2019) et al. (2019)
72 proposed to subdivide these trajectories based on their final characteristics ~~such as, like~~ thermal maturity. ~~As a~~
73 ~~result~~ ~~In this manner~~, the spatiotemporal evolution of ~~the~~ ~~sediments~~ ~~which regulate and their~~ thermal maturity is
74 ~~controlled, regulated~~ to a first-~~order~~, by the partition of incoming sediments along two ~~end-member~~ ~~endmember~~
75 pathways: (i) a deeper path leading to elevated thermal maturities ~~and constituted by underthrust material~~, the
76 **high thermal-maturity path**, and (ii) a shallower path ~~resulting in low thermal maturity~~ that typically lies closer to
77 the surface or gets frequently exhumed to near-surface levels, the **low thermal-maturity path** (Miyakawa et al., 2019).
78
79 ~~Although a number of researchers~~ ~~Previous studies~~ have ~~studied~~ ~~used~~ numerical and analogue approaches to
80 ~~study the diversity of particle paths by trajectories of sedimentary particles, and their~~ ~~Pressure-Temperature~~ ~~spatial and~~
81 ~~pressure-temperature~~ evolution, as a function of changes in ~~accreted and~~ erosion, sedimentation, or décollement
82 strength. The trajectory followed by ~~underthrust~~ sedimentary units is primarily determined by orogenic wedge
83 dynamics and its controlling forces (Plat, 1986). Although these ~~sediments, in presence of surface processes,~~
84 ~~distribution of~~ may only be exhumed near the backstop of the wedge, the trajectories of other accreted sediments
85 generally deflect toward the surface under the influence of erosion (Konstantinovskaia and Malavieille, 2005). In
86 fact, sedimentary particle trajectories gradually shift from deflection toward the ~~surface~~ ~~processes~~, near the front of
87 accretion to final exhumation near the wedge backstop (Wenk and Huhn, 2013). Still, even under-thrust
88 ~~sediments, which would co-relate to high-maturity paths in our study, have variable~~ ~~pressure-temperature paths~~

Formatted: Font: 11 pt, Font color: Text 1

Formatted: Font: 11 pt, Font color: Text 1

Formatted: Font: 11 pt

Formatted: Font: 11 pt

Formatted: Font: 11 pt

Formatted: Font: 11 pt

Formatted: Font: 11 pt

Formatted: Font: 11 pt

Formatted: Font: 11 pt

Formatted: Font: 11 pt

Formatted: Font: 11 pt

Formatted: Font: 11 pt

Formatted: Font: 11 pt

Formatted: Font: 11 pt

Formatted: Font: 11 pt

Formatted: Font: 11 pt

Formatted: Font: 11 pt

Formatted: Font: 11 pt

Formatted: Font: 11 pt, English (United Kingdom)

Formatted: Font: 11 pt, Font color: Text 1

Formatted: Font: 11 pt, Font color: Text 1

Formatted: Font: 11 pt, Font color: Text 1

Formatted: Font: 11 pt, Font color: Text 1

Formatted: Font: 11 pt, Font color: Black

Formatted: Font: 11 pt, Font color: Text 1

Formatted: Font: 11 pt, Font color: Text 1

Formatted: Font: 11 pt, Font color: Text 1

Formatted: Font color: Auto

Formatted: Border: Top: (No border), Bottom: (No border), Left: (No border), Right: (No border), Between : (No border), Tab stops: Not at 3.13" + 6.27"

89 (Ruh, 2020a). It is important to highlight that the majority of past studies have explored a snapshot of sediment
90 trajectories, assuming that the general nature of trajectories remains relatively fixed with time or is stationary, in
91 both analytical and numerical models(Hori & Sakaguchi, 2011; Elena-Konstantinovskaia & Malavieille, 2005; Platt, 1986;
92 Ruh, 2020a; Wenk & Huhn, 2013), its nature. However, the intrinsic connection between thermal maturity and the
93 comprehensive thermal exposure along the entire trajectory necessitates an in-depth investigation into the dynamic
94 and transitory nature of sediment trajectories.

Formatted: Font: 11 pt, Font color: Black

95 Although there is general consensus on the rate and extent of sediment trajectory transition from horizontal
96 to vertical during accretion, the dynamic perturbations in sediment dynamics have yet to be adequately examined.
97 For instance, while most studies show a great degree of correlation or lack thereof with its pre-accreted state has not
98 been suitably investigated between the initial depth of incoming sediments and their final position in the wedge (e.g.,
99 Mulugeta and Koyi, 1992; Willett, 1992), a dynamic fluctuation in this correlation due to thrusting can result in
100 non-stationary exhumation paths for accreting sediments in a wedge (e.g., Konstantinovskaia and Malavieille,
101 2005; Miyakawa et al., 2019). Much remains to be explored regarding how the partition of high- and low thermal
102 maturity paths and the general translation of how sediments occur travel inside the wedge natural wedges, given the
103 conventional assumption that accreting sediments remain at the same relative depth (Hori & Sakaguchi, 2011) and
104 translate along the adjacent "layers" without vertical mixing throughout the tectonic evolution of the wedge (Luján
105 et al., 2010; S. Willett et al., 1993) to yield this diversity of sediment paths. To (Hori and Sakaguchi, 2011).

Formatted: Font: 11 pt, Font color: Text 1

Formatted: Font: 11 pt, Not Bold, Font color: Text 1

Formatted: Font: 11 pt, Font color: Text 1

Formatted: Font: 11 pt, Font color: Text 1

Formatted: Font: 11 pt, Font color: Text 1

Formatted: Font: 11 pt, Font color: Text 1

Formatted: Font: 11 pt, Font color: Text 1

Formatted: Font: 11 pt, Font color: Text 1

Formatted: Font: 11 pt, Font color: Text 1

106 Our assessment identifies a primary gap in existing research: the prediction and mapping of the initial
107 sediment influx to their final location in the orogenic wedge. More specifically, the challenge lies in determining
108 which portions of incoming sediment will predominantly constitute the core of the wedge and which will reside at
109 comparatively shallower depths. Given that the maximum exposure temperature estimation from the thermal

Formatted: Font color: Auto

Formatted: Border: Top: (No border), Bottom: (No border), Left: (No border), Right: (No border), Between : (No border), Tab stops: Not at 3.13" + 6.27"

maturity is inherently reliant on the path of sediments inside the wedge, information on path diversity would inherently constrain the uncertainty in maximum exposure temperature used for the identification of paleothermal structures of subduction zones. Moreover, to better understand the time-depth paths of wedge sediments, their dependence on the initial state of undeformed sediments, and thus their thermal maturity, the factors that control the evolution of subduction-accretion systems, like sedimentation, erosion, and décollement strength (Mannu et al., 2016; Simpson, 2010), ought to be considered. (Mannu et al., 2016; Simpson, 2010).

Here, we explore in detail the impact that a realistic account of accretion in a subduction wedge has on the thermal maturity of its sediments. We simulate subduction-accretion using 2D finite-difference thermomechanical models incorporating empirical thermal conductivity values from the Nankai accretionary margin. We track the evolution of thermal maturity by computing vitrinite reflectance (R_o) on each marker and throughout the model, using three well-established methods of R_o computation, on each marker in the model as the wedge accretion develops by accretion the wedge under different sedimentation rates and décollement strengths. These factors notably alter the trajectories and thermal maturities of incoming sediments. Particularly, thrusts define sharp thermal maturity boundaries leading to stark differences in the thermal maturity of sediments that accrete in different thrust blocks, even when they follow similar trajectories and lay nearby.

2. Geological settings and model generalization

We use a generalized model for the subduction of an oceanic plate under a continental plate, with explicit integration of key parameters from the Nankai subduction margin off the Kii island in southwest Japan. The Nankai subduction margin is a product of the ongoing, northwest-directed subduction of the Philippine Sea Plate beneath the Amurian Plate at a convergence rate of 4.1-6.5 cm/yr (Seno et al., 1993; Miyazaki and Heki, 2001; DeMets et

Formatted: Font: 11 pt, Font color: Text 1

Commented [um1]: In Response to R1C13

Formatted: Font: 11 pt, Font color: Text 1

Formatted: Font: 11 pt, Font color: Text 1

Formatted: Font: 11 pt

Formatted: Font: 11 pt

Formatted: Font: 11 pt

Formatted: Font: 11 pt

Formatted: Font: 11 pt

Formatted: Font: 11 pt

Formatted: Font: 11 pt

Commented [um2]: In response to R1C2, R2C11

Formatted: Font color: Auto

Formatted: Border: Top: (No border), Bottom: (No border), Left: (No border), Right: (No border), Between : (No border), Tab stops: Not at 3.13" + 6.27"

131 al., 2010). Past studies posit the initiation of this subduction within the Nankai region at circa 6 Ma (Kimura et al.,
132 2014). The accretionary wedge adjacent to the Nankai margin is marked by the accretion of extensive sediment
133 layers (>1 km), predominantly formed by overlying younger trench sediments atop Shikoku Basin sediments. Mean
134 sedimentation rates of ~0.4 mm/yr for this area are calculated from sediment data onland and may largely reach the
135 trench through submarine channels (Korup et al., 2014).

Commented [um3]: In Response to R1C11

136 Another reason to select the Nankai subduction margin is that it is a particularly well-studied accretionary margin
137 regarding its paleo-thermal history and thermal maturity distribution. For example, Underwood et al. (1993) and
138 Sakaguchi (1999) used thermal maturity estimates from Shimanto accretionary wedge in the Nankai subduction
139 margin to suggest that ridge subduction can explain the resulting paleo-heat flow. Following this, Ohmori (1997),
140 published a distribution of thermal maturity and maximum exposure temperature for the Shimanto accretionary
141 wedge identifying out-of-sequence activity in the region. The accretionary wedge adjacent to the Kumano forearc
142 basin in the Nankai subduction margin has also been the subject of the NanTroSEIZE (Nankai Trough Seismogenic
143 Zone) project, which drilled C0002 borehole during the 2012 Integrated Ocean Discovery Program Expedition 338.
144 C0002 borehole is located approximately km southwest of Japan's Kii Peninsula in the Kumano Basin, within the
145 Nankai accretionary margin, and extends 3,348 meters below the seafloor. Having data on both thermal maturity
146 and thermal conductivity from the same borehole in subduction wedges is quite uncommon. To our knowledge, the
147 C0002 borehole, located next to the Kumano forearc basin, is the only place where such data can be found in an
148 accretionary wedge. Because of this unique characteristic, the C0002 borehole serves as an excellent dataset for
149 validation purposes. We modify the thermal conductivity computation for sediments and décollement (see Table
150 1) to match the empirical relationship between depth and thermal conductivity, as measured on core samples in the
151 borehole C0002 (Sugihara et al., 2014).

Formatted: Font color: Auto

Formatted: Border: Top: (No border), Bottom: (No border), Left: (No border), Right: (No border), Between : (No border), Tab stops: Not at 3.13" + 6.27"

152 While these adjustments render our models somewhat specific to the Nankai accretionary wedge, we propose that
153 the thermal conductivity values and trend are representative of patterns typically observed in forearc basins and
154 accretionary wedges across the globe, making it broadly applicable to general subduction margins. For instance, in
155 our simulations, the sediment thermal conductivity within our wedge steadily increases with depth from 0.96-4.0,
156 which is within the range of thermal conductivity estimates for comparable depth in other subduction zones, such
157 as the Hikurangi subduction margin, Japan Trench, and Taiwan subduction zone (Fig. S1, Henrys et al. 2003, Lin
158 et al. 2014, Chi and Reed, 2008). As a result, we compare our simulation results not only to thermal maturity values
159 in the Nankai accretionary margin but also to those of the Miura-Boso plate subduction margin in central Japan
160 and the fold and thrust belts of the Western Foothills complex in western Taiwan.

161 3. Methods

162 We employ I2VIS, a conservative (Gerya, 2019) finite-difference 2-D thermomechanical subduction-accretion
163 model with visco-plastic/brittle rheology (Gerya & Yuen, 2003)(Gerya and Yuen, 2003a, 2003b). The code solves
164 the governing equations for the conservation of mass, momentum, and heat as well as the advection equation with
165 a non-diffusive marker-in-cell scheme (Gerya, 2019) constrained by thermal conductivity values inferred from
166 Nankai accretionary wedge (Sugihara et al., 2014). Our numerical approach has several advantages over earlier
167 models attempts to simulate thermal maturity in an accretionary wedge (Miyakawa et al., 2019), such as a more
168 realistic geothermal profile, variable particle paths, and thermal evolution. The supplementary material contains
169 following sections, we provide information regarding the governing equations, the modified thermal conductivity
170 formulations based on the C0002 borehole in the Nankai accretionary wedge, boundary conditions, the rheological
171 model, model setup (Fig. S1) and surface processes (Fig. S2), and the computation of thermal maturity.

Commented [um4]: In Response to RIC8

Commented [um5]: Updated methods section in Response to RIC21

Formatted: Font: 11 pt

Formatted: Font: 11 pt

Formatted: Font: 11 pt

Commented [um6]: In Response to RIC16

Formatted: Font: 11 pt

Formatted: Font: 11 pt

Formatted: Font: 11 pt

Formatted: Font: 11 pt

Formatted: Font: 11 pt

Formatted: Font: 11 pt

Formatted: Font: 11 pt, Font color: Text 1

Formatted: Font: 11 pt, Font color: Text 1

Commented [um7]: In Response to R2C31

Formatted: Font: 11 pt, Font color: Text 1

Formatted: Font: 11 pt, Font color: Text 1

Formatted: Font: 11 pt, English (United Kingdom)

Formatted: Font color: Auto

Formatted: Border: Top: (No border), Bottom: (No border), Left: (No border), Right: (No border), Between : (No border), Tab stops: Not at 3.13" + 6.27"

172 23.1 An improved Governing equations

173 The mass conservation is described by the continuity equation with the Boussinesq approximation of
174 incompressibility.

$$175 \quad \frac{\partial v_x}{\partial x} + \frac{\partial v_y}{\partial y} = 0 \quad (eq. 1)$$

176 and the equation for conservation of momentum with an incompressibility assumption is expressed in the 2D-
177 stokes equation, for the x-axis and y-axis, respectively.

$$178 \quad \frac{\partial \sigma_{xx}}{\partial x} + \frac{\partial \sigma_{xy}}{\partial y} = \frac{\partial P}{\partial x} \quad (eq. 2)$$

$$179 \quad \frac{\partial \sigma_{yy}}{\partial y} + \frac{\partial \sigma_{xy}}{\partial x} = \frac{\partial P}{\partial x} - g\rho(T, P, C, M) \quad (eq. 3)$$

180 Where density $\rho(T, P, C, M)$ depends on temperature (T), pressure (P), composition (C), and mineralogy (M).

181 The thermal equation used in the model is as follows:

$$182 \quad \rho C_p \frac{DT}{Dt} = \frac{\partial q_x}{\partial x} + \frac{\partial q_y}{\partial y} + H_r + H_a + H_s + H_l \quad (eq. 4)$$

183 where,

$$184 \quad q_x = -k(T, C, Z) \frac{\partial T}{\partial x}, \quad q_y = -k(T, C, Z) \frac{\partial T}{\partial y} \quad (eq. 5)$$

$$185 \quad H_a = T\alpha \frac{DP}{Dt}, \quad H_s = \sigma_{xx}\epsilon_{xx} + \sigma_{yy}\epsilon_{yy} + \sigma_{xx}\epsilon_{xy} \quad (eq. 6)$$

Commented [um8]: In Response to R1C2

Formatted: Font color: Auto

Formatted: Border: Top: (No border), Bottom: (No border), Left: (No border), Right: (No border), Between : (No border), Tab stops: Not at 3.13" + 6.27"

186 Where $\frac{D}{Dt}$ is the Lagrangian time derivative, and x and y denote the horizontal and vertical coordinates, respectively;
187 $\sigma_{xx}, \sigma_{xy}, \sigma_{yy}$ are components of the deviatoric stress tensor; $\dot{\epsilon}_{xx}, \dot{\epsilon}_{xy}, \dot{\epsilon}_{yy}$ are components of the strain rate tensor;
188 P is pressure; T is temperature; q_x, q_y are the components of heat flux in the horizontal and vertical direction; ρ is
189 density; g is the vertical gravitational acceleration; C_p is the isobaric heat capacity; $H_r, H_a, H_s, H_{l\pm}$ denote the
190 radioactive, adiabatic, shear and latent heat production, respectively. $k(T, C, Z)$ is the thermal conductivity, a
191 function of composition, depth, and temperature (Table 1).

192 ~~In order to accurately assess thermal maturity calculation~~

Formatted: Font: Not Italic, Font color: Text 1

193 ~~Given that assessments of~~, it is crucial to consider the temperature distribution, which necessitates a realistic
194 ~~thermal conductivity profile when modeling thermal maturity are inherently reliant on the distribution of~~
195 ~~temperature inside the wedge, any attempt to model thermal maturity needs a realistic temperature~~
196 ~~gradient in the wedge. We~~. Many geodynamic models assume that thermal conductivity decreases as temperature
197 increases, following a defined relationship (e.g., Clauser and Huenges, 1995). These models typically predict a
198 decrease in thermal conductivity with depth within accretionary wedges, as geothermal profiles tend to increase in
199 temperature with depth. However, empirical data reveal a different trend: thermal conductivity increases with
200 depth, primarily due to sediment porosity influencing shallow thermal conductivity (Henry et al. 2003, Lin et al.
201 2014). Additionally, the thermal conductivity values calculated using the Clauser and Huenges model (1995) are
202 significantly higher than those observed at shallow depths (< 3 km). To address these disparities, we incorporate
203 ~~this by modifying the thermal conductivity computation for sediments and décollement (see Table 1 and~~
204 ~~section 1 in the provided supplementary text) to match the observed empirical relationship between depth~~
205 and thermal conductivity, as measured on core samples in the borehole IODP Site C0002 (Sugihara et al.,

Formatted: Font: 11 pt, Font color: Text 1

Commented [um9]: In Response to R1C17

Formatted: Font: 11 pt, Font color: Text 1

Formatted: Font: 11 pt, Font color: Text 1

Formatted: Font color: Auto

Formatted: Border: Top: (No border), Bottom: (No border), Left: (No border), Right: (No border), Between : (No border), Tab stops: Not at 3.13" + 6.27"

206 2014; Tobin et al., 2015). Both for the same accretionary wedge is scarce to find, and to our knowledge,
207 the C0002 borehole in Nankai accretionary wedge along the Kumano forearc basin is the only place with
208 available datasets from the IODP Site C0002 borehole in the Nankai accretionary wedge into our simulations. By
209 adjusting the thermal conductivity formulation for sediments based on temperature and depth, we aim to replicate
210 the empirical relationship observed in the core samples taken from the borehole at IODP Site C0002 (Sugihara et
211 al., 2014) and account for the decrease in thermal conductivity near the surface caused by increased porosity. We
212 modify the thermal conductivity formulation for sediments as a function of temperature and depth as follows.

$$k_{sed} = k_0 + \frac{807}{T + 77} \left(1 - \exp\left(\frac{-Z^2}{1.3e^7}\right) \right) \quad (eq. 6)$$

214 $k_0 = 0.96$ and 1.5 for the wedge sediment and décollement respectively. The larger thermal conductivity of the
215 décollement emulates higher heat transfer in shear zones due to fluid advection (Fig. S1).

216 3.2 Rheological model

217 The expression for effective creep viscosities (η_{eff}) is computed as follows

$$\eta_{disl} = 0.5(\epsilon_{II})^{\frac{1}{n}-1} A_D^{\frac{1}{n}} h^m \exp\left(-\frac{E_a + V_a P}{nRT}\right) \quad (eq. 7)$$

$$\eta_{diff} = 0.5 \frac{A_D}{S^{n-1}} \exp\left(-\frac{E_a + V_a P}{RT}\right) \quad (eq. 8)$$

$$\eta_{eff} = \left(\frac{1}{\eta_{disl}} + \frac{1}{\eta_{diff}} \right)^{-1} \quad (eq. 9)$$

Commented [um10]: In Response to R2C15

Commented [um11]: In Response to R1C47

Commented [um12]: In Response to R1C2

Formatted: Font color: Auto

Formatted: Border: Top: (No border), Bottom: (No border), Left: (No border), Right: (No border), Between : (No border), Tab stops: Not at 3.13" + 6.27"

221 where P is pressure (Pa), T is the temperature (K), R is the gas constant (8.314 J/K/mol), h is grain size (m) and
222 A_D, n, m, E_a and V_a are experimentally determined rheological parameters: A_D is the material constant
223 ($\text{Pa}^{-n}\text{s}^{-1}\text{m}^{-m}$), n is the stress exponent, m is the grain size exponent, E_a is activation energy (J/mol), V_a is activation
224 volume (J/Pa), and S is a stress factor for diffusion creep. As dislocation creep does not depend on grain size,
225 therefore, we assume $h^m = 1 \cdot \epsilon_{II}$ is the second invariant of strain tensor computed as

$$\epsilon_{II} = \sqrt{\frac{\dot{\epsilon}_{ij} \cdot \dot{\epsilon}_{ij}}{2}} \quad (\text{eq. 10})$$

227 The model uses visco-plastic rheology to account for both thermal conductivity and thermal maturity values
228 for an brittle rheology of the shallower and colder rigid lithosphere and deeper, hotter ductile lithosphere and
229 asthenosphere. Using the plastic yield threshold as per the Drucker-Prager criterion we limit effective viscosity as

$$\eta_{eff} \leq \frac{P \cdot \sin \varphi \cdot (1 - \lambda) + C \cdot \cos \varphi}{2\epsilon_{II}} \quad (\text{eq. 11})$$

231 Where c is cohesion and φ is an effective internal angle of friction or $\mu = \tan \varphi$ where is the coefficient of internal
232 friction and λ the fluid pressure ratio.

233 3.3 Boundary conditions

234 A free-slip boundary condition is implemented on all boundaries, except on the lower boundary, which is passable
235 in the vertical direction. Where we implement, an external free slip condition similar to where a free slip condition
236 is satisfied at an external boundary such that

Formatted: Font: 11 pt, Font color: Text 1

Commented [um13]: In Response to R1C6

Commented [um14]: In Response to R1C2

Formatted: Font color: Auto

Formatted: Border: Top: (No border), Bottom: (No border), Left: (No border), Right: (No border), Between : (No border), Tab stops: Not at 3.13" + 6.27"

237
$$\frac{\partial V_x}{\partial x} = 0, \text{ and } \frac{\partial V_y}{\partial y} = \frac{V_y}{\Delta Y_{external}} \quad (\text{eq. 10})$$

238 Where, V_x and V_y , are the velocities in the horizontal and vertical directions at the boundary, $\Delta Y_{external}$ is the depth
239 that lies outside the modeling domain, and where free slip condition is maintained. Similarly, we set thermally
240 insulating boundary conditions on all sides except the lower one where the external thermal boundary condition is
241 implemented.

242 3.4. Surface processes

243 The rock-water/air boundary is simulated by an adaptive irregular grid that is advected horizontally and vertically
244 and is coupled to the thermomechanical grid which controls the tectonic change of the surface. Apart from the
245 tectonic changes, surface processes prescribed in the model can also change the topography. The surface process
246 in the model is controlled by the conversion of rock markers to air/water and vice versa. All sedimentation in the
247 model happens as a focused deposition of sediments from sea to land in morphological depressions (e.g., trench)
248 is modelled as follows (Fig. S2)

249
$$Y_{new} = Y_{old} + K * Y_{fill} \quad (\text{eq. 11})$$

250 Where, $K = \min \left(\frac{V_{budget}}{V_{basin}}, 1 \right)$

251 The shape of the basin and the resolution of the surface grid can lead to overfilling or underfilling when using the
252 equation mentioned above to fill the basin. To address this issue, we calculate the volume of deposited sediments
253 and adjust for any deficit or overflow in the subsequent step. This ensures that, over time, the total amount of
254 sedimentation remains consistent with the prescribed value. However, it is challenging to ensure that all sediments

Commented [um15]: In Response to R1C2

Formatted: Font color: Auto

Formatted: Border: Top: (No border), Bottom: (No border), Left: (No border), Right: (No border), Between : (No border), Tab stops: Not at 3.13" + 6.27"

255 added in a particular step are accommodated within the basins, especially in models with high sedimentation rates
256 where significant runoff occurs. Therefore, the sedimentation rates mentioned in this study are computed as
257 effective sedimentation rates after the model runs, rather than being predetermined. We perform multiple models
258 runs (approximately 100) with sedimentation rates uniformly distributed in the range of 0.1-0.9 mm/yr. From these
259 runs, we select models that exhibit appropriate sedimentation rates. This selection process ensures that the average
260 sedimentation rates across all our models (ranging from 0.1-0.9 mm/yr) fall within the observed sedimentation rates
261 in our chosen natural equivalent, the Nankai accretionary wedge (Fukuehi et al., 2017), in the southwestern
262 subduction margin of Japan (Korup et al., 2014). For more specific information about the model run and prescribed
263 sedimentary conditions, please refer to Table 2

264 3.5 Thermal maturity calculation

265 The model computes the % R_oR_a of each marker to estimate the thermal maturity of sediments during the model run
266 using three widely used methods of thermal maturity modelling Easy% R_oR_a (Burnham & Sweeney, 1989,
267 Sweeney and Burnham 1990), Simple% R_oR_a (Suzuki et al., 1993) and Basin% R_oR_a (Nielsen et al., 2017; AH2017).
268 All the models presented here employ a simplified parallel Arrhenius reaction model, which accommodates an
269 array of activation energies for every component of the kerogen, allowing it to estimate thermal maturity under
270 varying temporal and thermal scales. The Easy% R_o model by Sweeney and Burnham (1990) can be described using
271 the following equations:

$$272 \quad x_i(t) = x_{oi} \exp\left(-\int A \exp\left(-\frac{E_{ai}}{RT(t)}\right) dt\right) \quad (eq. 12)$$

$$273 \quad X(t) = \sum_{i=1}^N x_i(t) \quad eq. 13$$

Formatted: Font: 11 pt, Font color: Text 1

Commented [um16]: In Response to R1C7

Commented [um17]: In Response to R1C2 and R2C4, R2C5

Formatted: Font: 11 pt, Font color: Text 1

Formatted: Font: 11 pt, Font color: Text 1

Formatted: Font: 11 pt, Font color: Text 1

Formatted: Font: 11 pt, Font color: Text 1

Formatted: Font: 11 pt, Font color: Text 1

Formatted: Font: 11 pt, Font color: Text 1

Formatted: Font: 11 pt, Font color: Text 1

Commented [um18]: In Response to R2C3

Formatted: Font color: Auto

Formatted: Border: Top: (No border), Bottom: (No border), Left: (No border), Right: (No border), Between : (No border), Tab stops: Not at 3.13" + 6.27"

$$F(t) = X(t = 0) - X(t) \quad (eq. 14)$$

$$\%R_o = \%R_{o0} \exp(3.7F) \quad (eq. 15)$$

Where, x_{oi} are weights of reactions for i^{th} component of the kerogen also described as the stoichiometric coefficient, A is the pre-exponential factor, E_{ai} is the activation energy of the i^{th} component of the kerogen, R is the gas constant, $T(t)$ is the temperature history, F is the amount of fixed carbon as a percentage and $\%R_{o0}$ is the vitrinite reflectance of the immature unaltered sediment. Sweeney and Burnham (1990) provided a set of 20 activation energies (E_{ai}) and the stoichiometric coefficient (x_{oi}) listed in Table 3. All thermal models used in this study use the same method of vitrinite reflectance computation albeit with different sets of activation energies, stoichiometric coefficient, pre-exponential factor and $\%R_{o0}$. Table 3 provides a comprehensive list of all these parameters.

All these approaches for computing $\%R_oR_a$ yield similar trends albeit with different absolute values. In the interest of clarity, we have mostly illustrated Easy $\%R_oR_a$, which is the most extensively used method for Vitrinite Reflectance computation. Hence, in the interest of clarity, we have mostly illustrated Easy $\%R_o$, which is the most extensively used method of Vitrinite Reflectance computation. Hence, and hereafter we refer Easy $\%R_oR_a$ as simply $\%R_oR_a$, unless explicitly stated. $\%R_oR_a$ is set to 0.2 $\%R_{o0}$ in sediment markers at the start of the model till 2.5 Myr, while $\%R_oR_a$ in markers for other rocks, air, and water is undefined at all times. After 2.5 Myr, the model computes $\%R_oR_a$ on each marker as a function of temperature (T), time (t), and amount of fixed carbon as a percentage ($f_c - F$). The initial $\%R_oR_a$ of newly deposited sediments is computed using an assumed water-sediment interaction temperature assumed to be the same as the thermocline. The thermocline used in the model has been estimated using the data obtained and made freely available by International Argo Program and the national programs that contribute to it for the region near Nankai (Argo, 2022). is set to 0.2 in sediment markers (Fig. S3; <https://argo.ucsd.edu>, <https://www.ocean-ops.org>).

Commented [um19]: R2C6

Formatted: Font: 11 pt, Font color: Text 1

Formatted: Font: 11 pt, Font color: Text 1

Formatted: Font: 11 pt, Font color: Text 1

Formatted: Font: 11 pt, Font color: Text 1

Formatted: Font: 11 pt, Font color: Text 1

Formatted: Font: 11 pt, Font color: Text 1, Subscript

Formatted: Font: 11 pt, Font color: Text 1

Formatted: Font: 11 pt, Font color: Text 1

Commented [um20]: In Response to RIC19

Formatted: Font: 11 pt, Font color: Text 1

Formatted: Font: 11 pt, Font color: Text 1

Formatted: Font: 11 pt, Font color: Text 1, Subscript

Formatted: Font: 11 pt, Font color: Text 1

Formatted: Font: 11 pt, Font color: Text 1

Formatted: Font: 11 pt, Font color: Text 1

Formatted: Font: 11 pt, Font color: Text 1

Formatted: Font: 11 pt, Font color: Text 1

Formatted: Font: 11 pt, Font color: Text 1

Commented [um21]: In Response to RIC3

Formatted: Font color: Auto

Formatted: Border: Top: (No border), Bottom: (No border), Left: (No border), Right: (No border), Between : (No border), Tab stops: Not at 3.13" + 6.27"

3.6 Model Set-up

The modelling domain is 3500 km wide and 350 km deep and is discretized into 3484×401 nodes populated with ~125 million markers (Fig. 1). The high resolution of 220 m (horizontal) \times 130 m (vertical) that we assign at the site of accretionary wedge evolution, decreases steadily toward the edges of the modelling domain to a minimum resolution of 3000 m \times 3200 m. The simulation consists of an oceanic plate converging with a velocity of ~5 cm/yr and subducting beneath a continental plate (Fig. 1). The oceanic plate consists of a 1-km-thick upper oceanic crust and a 7-km-thick lower crust. The thickness of the oceanic lithosphere depends on its age which is set to 20 Myr at the start of the model till 2.5 Myr, while R_0 in markers for other rocks, air, and water is undefined at all times. After 2.5 Myr, the model computes R_0 on each marker as a function of temperature (T), time (t), and amount of fixed carbon as a percentage (f_c). The initial R_0 of newly deposited sediments is computed using a water-sediment interaction temperature assumed to be the same as the thermocline. The thermocline used in the model has been estimated using the data obtained and made freely available by International Argo Program and the national programs that contribute to it for the region near Nankai (Fig. S3, Argo, 2022). —simulation (Turcotte and Schubert, 2002). The initial age of the oceanic lithosphere corresponds to the age of the subducting lithosphere in the Nankai subduction margin (Zhao et al. 2021). Displacement along the megathrust, at the contact between subducting oceanic plate and the overriding continental plate, occurs in a relatively weak basal layer in accretionary wedges across the globe (Byrne and Fisher, 1990). We simulate this with a predefined configuration at the interplate, with a 350-meter-thick weak décollement below a sediment layer that is a km thick. The wedge forms above this interphase by the accretion of sediments against the continental plate. The continental plate consists of an upper and lower continental crust with thicknesses of ~20 km and ~15 km, respectively, and is underlain by a mantle lithosphere of ~25 km. We use a thin (10 km) "sticky air" layer to overlay the top face of the rock strata inside the model which is a fluid with a low viscosity of 5×10^{17} Pa·s, and a low density, similar to air (white in Fig. 1) or water (light blue in Fig. 1) (Cramer et al., 2012). The transition between the lithosphere and asthenosphere is prescribed to occur at 1300°C. A weak layer is emplaced

±616

Commented [um22]: In Response to R1C2

Formatted: Space Before: 0 pt, After: 0 pt

Commented [um23]: In Response to R2C17

Formatted: Font: 11 pt, Font color: Text 1

Commented [um24]: In Response to R1C20

Formatted: Font color: Auto

Formatted: Border: Top: (No border), Bottom: (No border), Left: (No border), Right: (No border), Between : (No border), Tab stops: Not at 3.13" + 6.27"

318 at the junction of both plates, which fails mechanically and leads to subduction initiation. All sediments (light and
319 dark brown in Fig. 1) are rheologically identical, but colours are alternated in time to allow tracking the
320 development of different geological structures. Readers are referred to Table 1 for the rheological and thermal
321 properties of all the materials used. Note that in our models, we refer to the measure all distances from the point
322 where the continental and oceanic plates initially and is situated 1850 km from the right boundary of the modelling
323 area. The terms "landward" and "seaward" indicate the relative direction towards the continental plate or the oceanic
324 plate, respectively. The "Backstop" refers to the edge of the continental plate that buttresses the wedge and acts
325 akin to an indenter for the accretionary wedge. The "forearc high" represents the highest point in the forearc zone,
326 which includes both the accretionary wedge and the forearc basin.

327 2.2

328 3.7 Experimental Strategy

329 Here, we present a total of 10 models that vary in their effective basal friction or their effective sedimentation rate
330 to discern patterns of thermal maturity evolution in wedge sediments. Models $M_0^2, M_0^7, M_0^{12}, M_0^{17}, M_0^{22}, M_0^{4.5} -$
331 $M_0^{14.5}$ have no sedimentation and effective internal angle values for the décollement of $\phi = \phi_0 = 24.5^\circ, 7^\circ,$
332 $9.5^\circ, 12^\circ, 17^\circ$ and $22^\circ, 14.5^\circ$ respectively. The chosen range of effective décollement strength is well within the range
333 of values postulated by several studies for the Nankai accretionary wedge (Tesei et al., 2015). The rest of the models
334 shown here, $M_{0.1}^{12}, M_{0.3}^{12}, M_{0.5}^{12}, M_{0.7}^{12}$ and $M_{0.9}^{12}$ (Tesei et al., 2015). The rest of the models ($M_{0.1}^{9.5} - M_{0.9}^{9.5}$) and have a
335 medium-strength décollement and variable effective sedimentation rate ranging from 0.1 to 0.9 mm/yr.
336 Sedimentation occurs only at the trench in all of the models presented in this study, sedimentation is limited to the
337 trench, extending from the sea to land. Restricting sedimentation to the trench allows us to observe and
338 analyse the length and frequency of thrust sheets, enabling comprehensive investigation of their role in determining
339 sediment trajectories. With these models, we evaluate the particle trajectory and $\%R_0R_A$ of accreting sediments as

Commented [um25]: In Response to R2C26

Formatted: Font: 11 pt, Font color: Text 1

Commented [um26]: In Response to R1C2

Formatted: Font: 11 pt

Formatted: Font: 11 pt

Formatted: Font: 11 pt

Formatted: Font: 11 pt

Formatted: Font: 11 pt

Formatted: Font: 11 pt

Formatted: Font: 11 pt

Formatted: Font: 11 pt

Formatted: Font: 11 pt

Formatted: Font: 11 pt

Formatted: Font: 11 pt

Formatted: Font: 11 pt

Commented [um27]: In Response to R1C23

Formatted: Font: 11 pt

Formatted: Font: 11 pt

Formatted: Font: 11 pt

Formatted: Font color: Auto

Formatted: Border: Top: (No border), Bottom: (No border), Left: (No border), Right: (No border), Between : (No border), Tab stops: Not at 3.13" + 6.27"

361 probably due to the penetration of weaker décollement material into high shear zones, resulting in faults that are
362 weaker than the strain-softened wedge material.

363

364 Models without trench sedimentation grow solely by accretion of incoming seafloor sediments, with frequent

365 nucleation of frontal thrusts. Models with weaker décollements develop ~~thrusts~~ thrust sheets that are lengthier and but

366 remain active for shorter periods. This is clear when comparing, for models with increasingly strong décollement

367 $M_0^2 - M_0^{22}$ ($M_0^{4.5}, M_0^7, M_0^{9.5}, M_0^5, M_0^{14.5}$), the average distance between first and second frontal thrusts are $15.5 \pm$

368 7.0 km, 12.1 ± 3.6 km, 8.8 ± 3.3 km, 8.7 ± 2.1 km and 8.0 ± 1.8 km, respectively. Increasing sedimentation rate

369 also leads to an increase in thrust sheet length from 7.3 ± 1.1 km in $M_{0.1}^{12}$ to 13.8 ± 7.8 km in $M_{0.9}^{12}$ for model $M_{0.1}^{9.5}$ to

370 13.8 ± 7.8 km in model $M_{0.9}^{9.5}$.

371

372 In models with similar basal friction, models with higher sedimentation rates have lengthier thrust sheets that

373 remain active for longer periods (Table 2). Steeper surface slopes with increased décollement strengths and change

374 in thrust sheet length with sedimentation and décollement strength are well-known effects that have been

375 confirmed by previous numerical (Mannu et al., 2016; Wang & He, 1999) and analytical (Malavieille & Trullenque, 2009;

376 Storti & Mcclay, 1995) models and analytical (Malavieille and Trullenque, 2009; Storti and Mcclay, 1995) models.

377 All the reported values are mean \pm Standard Deviation values recorded between 2.5-7.5 Myr in individual models.

378 All models exhibit a temperature gradient that corresponds well with the temperature profile observed in the

379 boreholes at IODP Site C0002 in the Kumano forearc basin, on top of the Nankai accretionary wedge (Fig. S4, S14).

380

Formatted: Font: 11 pt

Formatted: Font: 11 pt

Formatted: Font: 11 pt

Formatted: Font: 11 pt, Font color: Text 1

Formatted: Font: 11 pt, Font color: Text 1

Formatted: Font: 11 pt

Commented [um31]: In Response to R2C24

Formatted: Font: 11 pt

Formatted: Font: 11 pt

Formatted: Font: 11 pt

Formatted: Font: 11 pt, English (United Kingdom)

Formatted: Font color: Auto

Formatted: Border: Top: (No border), Bottom: (No border), Left: (No border), Right: (No border), Between : (No border), Tab stops: Not at 3.13" + 6.27"

381 **4.1 Thermal maturity of the wedge**

382 Sediments are more thermally mature in wedges that have a higher sedimentation rate or décollement strength. For
383 example, the mean $\%R_oR_q$ of simulations for wedges with the highest sedimentation (M_0^{12}) is 12% higher (0.75)
384 than in those without sedimentation ($M_0^{4.5}$; Table 2, Fig. 3). Similarly, simulations of wedges with the
385 strongest décollement have the highest mean $\%R_oR_q$ (0.94) of all the simulations presented in this study.

386 Thermal maturity values increase with depth and landward distance from the trench to the forearc high
387 irrespective of the décollement strength, sedimentation rates and method of thermal maturity computation (Fig. 4).
388 As a result, sediments at the core of the wedge consistently reach the highest maturity (3.4). The absolute value of $\%R_oR_q$
389 and the rate at which thermal maturity values increase landward from the trench are larger for wedges with high
390 décollement strength (Fig. 2A). In 4A). For wedges with characterized by the same décollement strength but higher
391 trench sedimentation, we observe that the rate of thermal maturity increase increases in a landward direction from
392 the trench remain very similar and remains consistent across these wedges (Fig. 2B4B). Comparing the values of $\%R_oR_q$
393 (Fig. 2) R_oR_q along an arbitrary horizontal marker at the depth of trench in several models emphasizes this
394 result; the model with the highest décollement strength attains thereaches a maximum $\%R_oR_q$ of 1.25, and has the
395 highest rate of landward increase in thermal maturity (Fig. 2A4A). However, all models with similar décollement
396 strength but different sedimentation do not visibly vary in their rate or magnitude of landward increase in thermal
397 maturity. All models show a decrease in thermal maturity landward of the forearc high, commonly of 0.2 $\%R_oR_q$.
398 Other interesting observations that we explore below are the increased thermal maturity occurring in the vicinity
399 of thrusts (e.g. Fig 1) and the reversal in sediment maturity around out-of-sequence thrust (e.g. Fig 1) active over
400 longer times visible across several models (e.g. Fig 3).

Formatted: Font color: Text 1

Formatted

Formatted: Font: 11 pt

Formatted

Formatted

Commented [um32]: In Response to R1C36

Formatted

Commented [um33]: In Response to R2C28hl

Formatted

Formatted: Font color: Auto

Formatted: Border: Top: (No border), Bottom: (No border), Left: (No border), Right: (No border), Between : (No border), Tab stops: Not at 3.13" + 6.27"

442 extreme values of $\%R_0$. We observe that the typical uncertainty in maximum exposure temperature increases
443 with an increase in values of $\%R_0$ with $\sim 15^\circ\text{C}$ interval at $\%R_0=0.2$ compared to $\sim 33^\circ\text{C}$ interval at
444 $\%R_0=3$, (both for 95% confidence interval, Fig. 4b). Furthermore, we observe that incorporating
445 information about the present normalized depth of the sediments w.r.t the thickness of the wedge (as represented by
446 different colours (Y_n) significantly aids in Fig 4a) greatly helps to further constrain the maximum exposure
447 temperature. For instance, although the overall uncertainty at $\%R_0=1$, is $\sim 23^\circ\text{C}$, for sediments with a normalized
448 depth Y_n of 0.2-0.4, the uncertainty greatly reduces to only $\sim 10.5^\circ\text{C}$. Thus, the range of thermal maturity values for
449 sediments clearly has a large correlation with their trajectories.

Formatted

Commented [um36]: In Response to R1C41

Formatted

450 **4.4 3.4 Comparison of Easy $\%R_0$, Simple $\%R_0$ and Basin $\%R_0$**

451 Finally as our models produced three sets The usage of $\%R_0$ using Easy $\%R_0$ (referred to as $\%R_0$ throughout our study),
452 Simple $\%R_0$ and Basin $\%R_0$, it also gives $\%R_0$ in our models provides us with a unique distinct perspective on the
453 comparative (dis)advantages of each method in estimating thermal maturity values. The non-uniqueness of
454 maximum exposure temperatures for the same values of $\%R_0$ arises from the variation in sediment trajectory and
455 thermal exposure. This diversity among sediment markers results in multiple markers attaining the same level of
456 thermal maturity. We refer to the range of maximum exposure temperatures corresponding to similar $\%R_0$ values
457 as the uncertainty in maximum exposure temperatures. Uncertainty for all three models increases with increasing
458 $\%R_0$ from $\sim 20-25^\circ\text{C}$ at ~ 0.3 which rises to $\sim 35^\circ\text{C}$ at $\%R_0=3.5$ (Fig. 4b, 6b). Easy $\%R_0$ is probably the most
459 well best-recognised method of thermal maturity computation and yields the best constraint on uncertainty for very
460 small changes around the values less than nearing <1 values. For the values of $\%R_0$ between 1 and 3, all models
461 yield very similar uncertainty, with Simple $\%R_0$ yielding the most constrained exposure temperatures (Fig. 4b,
462 6b). However, beyond $\%R_0=3$, the Simple $\%R_0$ becomes highly unreliable, with uncertainty in exposure

Commented [um37]: In Response to R1C46

Formatted: Subscript

Formatted: Outline numbered + Level: 2 + Numbering Style: 1, 2, 3, ... + Start at: 4 + Alignment: Left + Aligned at: 0" + Indent at: 0.25"

Formatted

Commented [um38]: In Response to R1C44

Formatted

Commented [um39]: In Response to R1C45

Formatted

Formatted: Font color: Auto

Formatted: Border: Top: (No border), Bottom: (No border), Left: (No border), Right: (No border), Between : (No border), Tab stops: Not at 3.13" + 6.27"

463 temperatures as high as 55°C at $R_0 = 4$. Easy R_0 yields a reasonable uncertainty range of ~37°C till
464 $R_0 = 4.4$, but and starts to be unreliable above this value. Basin R_0 remains consistent until a very
465 high value of $R_0 \sim 6$, and thus provides the best constraint on the widest range of values of thermal
466 maturity (Fig. 4b, 6b).

468 4.5. Discussion

469 Our models achieve realistic thermal maturity distributions thanks to unique computational advantages over models in the
470 previous studies (Mannu et al., 2016, 2017; Miyakawa et al., 2019), despite several relevant assumptions. Models are simplified
471 by assuming no elasticity, predefined décollement, no erosion, and using simple and uniform rheology, and either has an
472 insufficient resolution or lack empirical relations to simulate the compaction of sediments and processes of multiscale fluid
473 flow. Although these assumptions hinder a wholesale comparison between our simulations and natural examples of
474 accretionary wedges, we are confident of the thermal maturity patterns of our models. Our estimated R_0 values for the model
475 $M_{0.1}^{12} - M_{0.9}^{12}$ are in very good agreement with the R_0 values measured for the borehole C0002 Nankai accretionary wedge
476 (used for thermal conductivity values) by Fukuchi et al. 2009 (Figure 5). Moreover, the temperature estimated from the
477 observed thermal maturity of a timeframe of 1-2 Myr in the borehole, also strongly correlates with the trend and the range of
478 95% Confidence interval of T vs R_0 estimated in our models (Fig S7). Furthermore, our models also correlate with the
479 patterns of P-wave velocity for Nankai (Górszczyk et al., 2019; Nakanishi et al., 2018) and Hikurangi (Arai et al., 2020)
480 margins (Dewing & Sanei, 2009). Models compute realistic thermal maturity distributions thanks to several key improvements.
481 Firstly, our models calculate temperature gradients that evolve at long time intervals and thus closely replicate accretionary
482 wedges in nature (Fig. S2). This enables the simulation of realistic temperature profiles based on thermal conductivity values
483 derived empirically from natural accretionary wedges, as in our case, the Nankai margin (Sugihara et al., 2014). Secondly, our
484 simulations account for the effects that thermal and isostatic feedback from the oceanic lithosphere have on the evolution of
485 the wedge by simulating plate subduction at a large scale rather than just the accretionary wedge (Miyakawa et al., 2019).

Formatted: Font: 11 pt

Formatted: Font: 11 pt, Subscript

Formatted: Font: 11 pt

Formatted: Font: 11 pt

Formatted: Font: 11 pt

Formatted: Font: 11 pt

Formatted: Font: 11 pt, Subscript

Formatted: Font: 11 pt

Formatted: Font: 11 pt

Formatted: Font: 11 pt

Formatted: Font: 11 pt

Formatted: Font: 11 pt

Formatted: Font: 11 pt

Formatted: Don't keep lines together

Formatted: Font color: Auto

Formatted: Border: Top: (No border), Bottom: (No border), Left: (No border), Right: (No border), Between : (No border), Tab stops: Not at 3.13" + 6.27"

486 Finally, our method calculates the vitrinite reflectance of sediments on each marker of the model. This capacity to accurately
487 estimate thermal maturity in each marker informs the research questions of this study and allows inferences beyond those of
488 depth-dependent thermal maturity distributions.

489 The thermal maturity of the wedge increases landward, as signalled by the landward increase in %R₀ (Fig. 1). This
490 has been observed in natural accretionary wedges such as Miura–Boso plate subduction margin (Yamamoto et al., 2017), fold
491 and thrust belts—Western Foothills complex in western Taiwan (Arita–Sakaguchi et al., 2007) and other numerical models of
492 accretion (Miyakawa et al., 2019), resulting from the long-term deformation of older accreted sediments and the backstop-
493 forced exhumation in the wedge. Our models show that the rate of landward rise in thermal maturity is faster for thicker wedges
494 (Fig. 2). This is the case for wedges with high basal strength (M_0^{22}), for sediments in thicker wedges deform more prominently
495 than those in their thinner counterparts. Simulations also show that sediments reach deeper levels in thicker wedges and that
496 this increases the overall thermal maturity of the wedge. Also, increased exhumation rates and steeper thermal maturity
497 gradients occur in the wedge interior, as the continental backstop deflects sediment trajectories upwards during accretion (Fig.
498 2). As a result, for the geometry of the backstop used in our models, backstop forced exhumed material is, on average,
499 thermally more mature.

500 Our models expose two relevant cases where the increase of thermal maturity with depth or landward is relevantly
501 altered: on-fault increase and fault-block inversion. Our models attest to the steep rise in thermal maturity of sediments at fault
502 sites (Fig. 1). This is well documented in nature, as for boreholes C0004 (Sakaguchi et al., 2011). However, on-fault increases
503 in thermal maturity are comparatively smaller in our simulations and lack the marked increase in %R₀ observed at fault sites
504 in nature. This is primarily due to our models developing wider fault zones than their natural equivalents and the subsequent
505 acceleration in the thermal diffusion occurring in simulated thrusts. During fault-block inversions, the positive gradient of
506 thermal maturity with depth is inverted by thrusting relatively mature sediments over less mature sediments (Underwood et al.,
507 1992). This is known from natural observations, as along the Fukase Fault in Shimanto accretionary wedge (Ohmori et al.,

Formatted: Font color: Auto

Formatted: Border: Top: (No border), Bottom: (No border), Left: (No border), Right: (No border), Between : (No border), Tab stops: Not at 3.13" + 6.27"

1997) and underneath the forearc basin in Nankai accretionary wedge (Fukuchi et al., 2017), and previous modelling efforts (Miyakawa et al., 2019).

Collation of the above implies that the thermal maturity of accretionary wedges results from the general increase of thermal maturity (i) with depth and (ii) landward, as well as from its (iii) modification by thrust faults. Our models suggest that the thermomechanical models presented in this study provide (a) an explanation for the trend in thermal maturity observed in accretionary wedges, (b) a new venue to explore the uncertainty in the estimation of maximum exposure temperature using vitrinite reflectance, and (c) an estimate of the minimum lateral distance between the trench and the location of a paleo-thermal anomaly on the subduction plate for it to be identified after accretion.

5.1 Thermal maturity distribution and importance of thrusting in wedges

Collectively, our results support a general increase of thermal maturity with depth and landward in accretionary wedges. The thermal maturity increase with depth is primarily the result of progressively larger exposures to higher temperatures as depth of burial increases. On the contrary, the landward increase in thermal maturity is caused by the long-term deformation of sediments accumulated at older times and the exhumation of sediments that were underthrust as they meet the backstop. Our models demonstrate that the rate of landward thermal maturity increase is faster for thicker wedges, both for the case of sediment near the surface and deep inside the wedge (Fig. 4). This can be attributed to a larger proportion of sediments being exposed to higher temperatures over an extended duration within thicker wedges, but validating this result with natural observations remains challenging, given the very limited availability of thermal maturity data across natural wedges. Accretionary wedges in our models can be simplified as a system where the subducting oceanic plate acts as the primary heat source, while the seafloor acts as a heat sink. The heat generated through other sources such as shear heating, radioactivity, and advection is relatively insignificant compared to the heat originating from the younger oceanic plate. In our simulations, we

Commented [um40]: In Response to R1C10

Formatted: Font color: Auto

Formatted: Border: Top: (No border), Bottom: (No border), Left: (No border), Right: (No border), Between : (No border), Tab stops: Not at 3.13" + 6.27"

530 consider a relatively younger and hotter oceanic plate of approximately 20 Myr, which is consistent with the
531 accretionary wedge in the Nankai region adjacent to the Kumano forearc basin (Zhao et al., 2021). Given that the
532 convergence rate remains constant across all models, the heat received from the oceanic plate should remain
533 relatively similar. However, as the wedge thickness increases, the temperature gradient between the boundaries of
534 the wedge must become gentler, resulting in a larger portion of the wedge experiencing elevated temperatures.
535 Moreover, frequent advection from the subduction channel also results in elevated temperatures in the core of the
536 wedge. Finally, models with thicker wedges typically exhibit higher décollement strength, leading to increased
537 shear heating at the base of the wedge. Observational studies conducted by Yamano et al. (1992) on the thermal
538 structure of the Nankai accretionary prism have further highlighted that the landward increase in prism thickness
539 is the most significant factor contributing to temperature variations within the wedge. Consequently, the sustained
540 higher temperatures within thicker wedges over time would lead to a higher rate of landward thermal maturity.

541 Our models show two cases where the above-mentioned trend in thermal maturity is relevantly altered, which we
542 nominate "on-fault increase" and "fault-block inversion". For instance, Fig. 3 shows a steep rise in the thermal
543 maturity of sediments at fault sites. Thermal maturity inversions by thrusting, which are commonplace in
544 accretionary contexts, are the primary cause of thermal maturity differentiation among wedges with initially similar
545 geothermal gradients. In other words, the similar paleo-thermal structures. During fault-block inversions, the positive
546 gradient of thermal maturity with depth is inverted as relatively mature sediments are thrust over less mature
547 sediments (Underwood et al., 1992). The strong differentiation in the trajectory of sediments led by thrusting has a
548 larger influence over thermal maturity than their burial depth or their in-wedge location. This novel inference has
549 probably remained concealed thus far due to the large number of parameters that condition thrust development,
550 frequency, length, and thermal state. Influencing parameters to include sedimentation, erosion, basal friction and relief,
551 pore pressure and fluid state, wedge length and thickness, taper angle, and many others (Dominguez et al., 2000; E-

Commented [um41]: In Response to R1C56 and R2C4, R2C39

Formatted: Indent: First line: 0"

Formatted: Font: 11 pt, Font color: Text 1

Formatted: Font: 11 pt, Font color: Text 1

Formatted: Font: 11 pt, Font color: Text 1

Formatted: Font: 11 pt, Font color: Text 1

Formatted: Font color: Auto

Formatted: Border: Top: (No border), Bottom: (No border), Left: (No border), Right: (No border), Between : (No border), Tab stops: Not at 3.13" + 6.27"

552 Konstantinovskaia, 2005; Mannu et al., 2016; Ruh, 2017; Simpson, 2010; H. J. Tobin & Saffer, 2009). It is nevertheless
553 important to note that the frequency of faults in a wedge can be impacted by many other factors, including hinterland
554 sedimentation(Simpson, 2010; Storti & Mcclay, 1995), erosion(E. Konstantinovskaia, 2005; S. D. Willett, 1999), and seafloor
555 topography(Dominguez et al., 2000). Below, we discuss how thrusts not only alter the thermal evolution of accreting sediments
556 but are, in fact, the primary control of their thermal maturity, and the lack of high-resolution thermal maturity data. ▲

Formatted: Font: 11 pt, Font color: Text 1

~~Thermal maturity correlates with sediment depth weakly near faults and more strongly away from them.~~
558 The distance of sediment from frontal thrust dictates the trajectory of sediment grains, and as a result, the pressure-temperature
559 conditions to which they are exposed. In this study, we have considered solely how décollement strength and the rate of trench
560 sedimentation vary the frequency, architecture, and overall behaviour of thrusts, and the frontal thrust, as the wedge evolves.
561 ~~Our results show the need to consider all factors influencing fault frequency when inferring the geothermal history~~
562 ~~of contractional terrains by means of thermal maturity.~~ Fortunately, this predictive exercise should be relatively
563 straightforward, for the impact of these external factors on the fault structure of wedges has been established(Fillon et al.,
564 2012; Mannu et al., 2016, 2017; Mugnier et al., 1997; Simpson, 2010; Storti & Mcclay, 1995), and the effect of each of these
565 factors can be accounted for when assessing the trajectory of sediments and the distribution of thermal maturity in accretionary
566 wedges.

Formatted: Font: 11 pt, Font color: Text 1

567 Sediment mixing in subduction wedges is primarily controlled by thrusting. Previous studies have reached seemingly
568 contradicting outcomes when using numerical(Miyakawa et al., 2019; Wenk & Huhn, 2013; S. Willett et al., 1993) and
569 analogue(E. Konstantinovskaia, 2005; Mulugeta & Koyi, 1992) approaches to analyze sediment trajectories as a function of
570 changes in erosion, sedimentation, or décollement strength. While some studies showed that the rate and extent of a transition
571 by which sediment trajectories change from generally horizontal to increasingly vertical during accretion change consistently
572 with the initial depth of incoming sediments(Mulugeta & Koyi, 1992; S. Willett, 1992), others predicted different crossover
573 paths for sediments accreting over a range of décollement strengths(E. Konstantinovskaia, 2005). Our models show that both
574 are valid results and that changes in trajectory patterns leading to path crossovers are controlled by the horizontal distance of

Formatted: Font color: Auto

Formatted: Border: Top: (No border), Bottom: (No border), Left: (No border), Right: (No border), Between : (No border), Tab stops: Not at 3.13" + 6.27"

575 ~~sediments from the frontal thrust. Starting at a threshold distance from the trench, sediments at different depths follow~~
576 ~~laminar paths along different trajectories within the wedge. Laminar-type trajectories can be reproduced in a broad~~
577 ~~range of simulations and are particularly common in models with low sedimentation and décollement strengths.~~
578 ~~However, the depth-dependence of sedimentary paths varies periodically as a function of distance from the trench~~
579 ~~of specific sedimentary packages (Fig. 3,6). This effect, which is particularly marked in the neighbourhood of the frontal~~
580 ~~thrust, explains the crossover paths for incoming sedimentary packages at similar depths and different horizontal locations, as~~
581 ~~shown by Konstantinovskaia et al. 2005. Therefore, thrust faults in the wedge act as the primary agent controlling whether~~
582 ~~sediments sustain depth-controlled laminar flow or mix.~~

Formatted: Font: 11 pt, Font color: Text 1

583 The thermal maturity that incoming sediments reach also varies periodically as a function of thrust frequency.

Formatted: Font: 11 pt, Font color: Text 1

584 ~~Although previous research considered non-laminar sediment trajectories as chaotic (Mary et al., 2013), and the wide variety~~
585 ~~of trajectories shown in our models seem to agree with this (Fig. 3, Fig S4), patterns emerge when we correlate~~

Formatted: Font: 11 pt, Font color: Text 1

586 the lateral and vertical position of incoming sediments ~~with and~~ their eventual thermal maturity, ~~we can deduce that~~
587 ~~the overall movement of sediments in the wedge is predominantly layered but not stationary over time.~~ Changes in

Formatted: Font: 11 pt, Font color: Text 1

Formatted: Font: 11 pt, Font color: Text 1

588 the depth of the thermal maturity boundary are less frequent and have larger amplitudes with increased décollement
589 strength, and especially, increased sedimentation rates (Fig. 45). The periodicity in the thermal maturity boundary

Formatted: Font: 11 pt, Font color: Text 1

Formatted: Font: 11 pt, Font color: Text 1

590 marks the periodic oscillation of the predominant trajectory followed by incoming sediments, i.e., ~~between~~
591 accretion (low thermal maturity path) and ~~underthrusting~~ ~~under-thrusting~~ (high-thermal maturity path). As a result,

Formatted: Font: 11 pt, Font color: Text 1

Formatted: Font: 11 pt, Font color: Text 1

592 it should also strongly correlate with the periodicity observed in the evolution of forearc topography (Menant et al.,

Formatted: Font: 11 pt, Font color: Text 1

593 ~~2020) (Menant et al., 2020) and the frequency of thrust formation as such in our models. This is expected, given that~~

Formatted: Font: 11 pt, Font color: Text 1

594 ~~thrusts are active over longer mean times, and they thus channel material toward the décollement more efficiently,~~

Formatted: Font: 11 pt, Font color: Text 1

Formatted: Font: 11 pt, Font color: Text 1

595 in wedges with stronger décollement or increased sedimentation. While sediments at internal and higher structural

Formatted: Font color: Auto

596 positions of the wedge are translated ~~towards~~ ~~toward~~ the surface and have a lower thermal maturity, sediments at

Formatted: Border: Top: (No border), Bottom: (No border), Left: (No border), Right: (No border), Between : (No border), Tab stops: Not at 3.13" + 6.27"

597 external and lower structural positions are translated ~~towards~~toward the décollement and have a relatively higher
598 maturity. The entire cycle is repeated with the formation of new in-sequence thrust.

Formatted: Font: 11 pt, Font color: Text 1

Commented [um42]: In Response to R2C46

599 This is a relevant observation, for it typifies the causality of particular sediment grains following a high or
600 low maturity path, a long-standing unanswered question (Miyakawa et al., 2019). (Miyakawa et al., 2019). We
601 corroborate this observation by analyzing the terminal thermal maturity of sediments across a frontal thrust active
602 at a younger age. ~~For An~~ example, ~~by showing in Fig. 7 shows~~ the thermal maturity of sediments at ~7.5 Myr across
603 a thrust active at ~4 Myr, ~~as in Fig. 7~~. Whereas this occurs for all thrusts in the wedge, the frontal thrust is particularly
604 pronounced in partitioning sediments into the high and low maturity paths.

Formatted: Font: 11 pt, Font color: Text 1

Formatted: Font: 11 pt, Font color: Text 1

Formatted: Font: 11 pt, Font color: Text 1

Formatted: Font: 11 pt, Font color: Text 1

Formatted: Font: 11 pt, Font color: Text 1

Formatted: Font: 11 pt, Font color: Text 1

605 ~~Geothermal~~ Thermal maturity correlates with sediment depth weakly near faults and more strongly away from them.
606 The distance of sediment from the frontal thrust dictates the trajectory of sediment grains, and as a result, the
607 pressure-temperature conditions to which they are exposed.

Formatted: Font: 11 pt, Font color: Text 1

608 Our results show the need to consider all factors influencing fault frequency when inferring the geothermal history
609 of contractional terrains by means of thermal maturity. In this study, we have considered solely how décollement
610 strength and the rate of trench sedimentation vary the frequency, architecture, and overall behavior of thrusts, and
611 the frontal thrust, as the wedge evolves. Fortunately, this predictive exercise should be relatively straightforward,
612 for the impact of these external factors on the fault structure of wedges has been established (Fillon et al., 2012;
613 Mannu et al., 2016, 2017; Mugnier et al., 1997; Simpson, 2010; Storti and Mcclay, 1995), and the effect of each of
614 these factors can be accounted for when assessing the trajectory of sediments and the distribution of thermal
615 maturity in accretionary wedges. It is nevertheless important to note that the frequency of faults in a wedge can be
616 impacted by many other factors, including hinterland sedimentation (Storti and Mcclay, 1995; Simpson, 2010;

Formatted: Font: 11 pt, Font color: Text 1

Formatted: Font color: Auto

Formatted: Border: Top: (No border), Bottom: (No border), Left: (No border), Right: (No border), Between : (No border), Tab stops: Not at 3.13" + 6.27"

617 Fernández-Blanco et al. 2020), erosion (Konstantinovskaia, 2005; Willett, 1992), and seafloor topography
618 (Dominguez et al., 2000).

619 5.2. Implications

620 ~~information stored in the incoming sediments can only be retrieved if sediments are at appropriate~~
621 ~~locations with respect to emergent thrusts. We illustrate this using two runs of the same model and tracking an~~
622 ~~artificial thermal anomaly imposed on incoming sediments at two different locations (Fig. 7). This hypothetical~~
623 ~~thermal anomaly can be conceptualized as any alteration of the thermal maturity profile of incoming sediments, for~~
624 ~~example, elevated heat flows by an antecedent magmatic intrusion. While the change in %R₀ associated with the short-~~
625 ~~lived thermal anomaly results in abnormally high values of thermal maturity in both sediment packages, it can only be retrieved~~
626 ~~for the end-model run of sediments located further from the trench (those in the right panel, Fig. 7b). Contrarily, the end-~~
627 ~~model run of sediments closer to the trench (those in the left panel, Fig. 7a) shows no signs of discontinuity in the~~
628 ~~thermal maturity distribution of the wedge. This is because we deliberately placed the thermal anomaly at sites that~~
629 ~~evolve at two structural locations during the model run, i.e., above and below a yet undeveloped frontal thrust (Fig.~~
630 ~~7). The sediment sector affected by the thermal anomaly closer to the trench is overthrust by the frontal thrust~~
631 ~~and remains in a footwall location thereafter (Fig. 7a). In contrast, the homologous sedimentary package further~~
632 ~~away from the trench is accreted by the frontal thrust and remains in a hanging wall location (Fig. 7b). Thus, the~~
633 ~~preservation of the record of an antecedent thermal anomaly is only possible in the former case. We further note~~
634 ~~that, in our simulations, the entire vertical column of sediments records the thermal anomaly, while in nature, the~~
635 ~~anomaly may affect only sediments at the deeper locations of the sedimentary pile, which are in turn the sediments~~
636 ~~that most likely to follow a high maturity path. We thus regard the possibility of retrieving such antecedent~~
637 ~~geothermal information as minimal.~~

Commented [um43]: In Response to RIC10

Formatted: Font: 11 pt

Formatted: Font: 11 pt

Formatted: Font: 11 pt

Formatted: Font: 11 pt

Formatted: Font: 11 pt

Formatted: Font: 11 pt

Formatted: Font: 11 pt

Formatted: Font color: Auto

Formatted: Border: Top: (No border), Bottom: (No border), Left: (No border), Right: (No border), Between : (No border), Tab stops: Not at 3.13" + 6.27"

638 The main implications of this contribution emerge from its predictive power. Our approach can predict to a precise
639 degree the thermal maturity of sediments and the uncertainty associated with the maximum exposure temperature
640 in accretionary contexts with known structuration. More accurate quantification of the thermal evolution
641 and thermal state of accreted sediments reduces the uncertainties attached to the location of temperature-led
642 transformations of organic material into hydrocarbons in subduction margins and other accretionary contexts. Such
643 increased accuracy in the distribution of thermally mature sediments may also be applied for improved assessments
644 of the evolution in time of any other geothermal process, including seismic slip, magmatic and metamorphic extent,
645 porosity, compaction, and diagenesis of sediments, and the reconstruction of convergent margins in general (Bostick
646 & Pawlewicz, 1984; Ferreiro Mählmann & Le Bayon, 2016; Rabinowitz et al., 2020; A. Sakaguchi et al., 2011; Totten & Blatt,
647 1993; Underwood et al., 1992). (Bostick and Pawlewicz, 1984; Mählmann and Le Bayon, 2016; Rabinowitz et al.,
648 2020; Sakaguchi et al., 2011; Totten and Blatt, 1993; Underwood et al., 1992).

649 Our simulations also imply that the paleo-thermal information stored in the incoming sediments can only be
650 retrieved if sediments are at appropriate locations with respect to emergent thrusts. We illustrate this using two runs
651 of the same model and tracking an artificial thermal anomaly imposed on incoming sediments at two different
652 locations (Fig. 8). This hypothetical thermal anomaly can be conceptualized as any alteration of the thermal
653 maturity profile of incoming sediments, for example, elevated heat flows by an antecedent magmatic intrusion.
654 While the change in %Ro associated with the short-lived thermal anomaly results in abnormally high values of
655 thermal maturity in both sediment packages, it can only be retrieved for the end-model run of sediments located
656 further from the trench (those in the right panel, Fig. 8B). Contrarily, the end-model run of sediments closer to the
657 trench (those in the left panel, Fig. 8A) shows no signs of discontinuity in the thermal maturity distribution of the
658 wedge. This is because we deliberately placed the thermal anomaly at sites that evolve at two structural locations
659 during the model run, i.e., above and below a yet-undeveloped frontal thrust (Fig. 8). The sediment sector affected

Formatted: Font: 11 pt

Formatted: Font: 11 pt

Formatted: Font: 11 pt

Formatted: Font: 11 pt

Formatted: Font: 11 pt, English (United Kingdom)

Formatted: Font: 11 pt

Formatted: Font: 11 pt

Formatted: Font: 11 pt

Formatted: Font: 11 pt

Commented [um44]: In Response to R1C51

Formatted: Font: 11 pt

Formatted: Font: 11 pt

Formatted: Font color: Auto

Formatted: Border: Top: (No border), Bottom: (No border), Left: (No border), Right: (No border), Between : (No border), Tab stops: Not at 3.13" + 6.27"

660 by the thermal anomaly closer to the trench is overthrust by the frontal thrust and remains in a footwall location
661 thereafter (Fig. 8a). In contrast, the homologous sedimentary package further away from the trench is accreted by
662 the frontal thrust and remains in a hanging-wall location (Fig. 8b). Thus, the preservation of the record of an
663 antecedent thermal anomaly is only possible in the former case. We further note that, in our simulations, the entire
664 vertical column of sediments records the thermal anomaly, while in nature, the anomaly may affect only sediments
665 at the deeper locations of the sedimentary pile, which are in turn the sediments that most likely to follow a high-
666 maturity path. We thus regard the possibility of retrieving such antecedent geothermal information as minimal.

667 Finally, among the three methods of R_o/R_a computation, Easy R_o/R_a and Basin R_o/R_a are clearly more consistent
668 and well-constrained on a wide range of thermal maturity/maturities in comparison to Simple R_o/R_a , which seems
669 to be particularly useful for a smaller range of thermal maturity values. This simply illustrates the fact that while
670 Easy R_o/R_a and Basin R_o/R_a computation deals with several parallel reactions related to the maturity of kerogen
671 (and hence multiple activation energies), the Simple R_o/R_a is based on best-fitted single activation energy, and
672 hence yields large confidence intervals at the extreme R_o/R_a values. Additionally, the inclusion of the higher
673 activation energy reactions in Basin R_o/R_a makes it the best-suited formulation for sediments at the deeper and
674 shear zone sediments which usually get saturated using Easy R_o/R_a .

675 5.3 Comparisons to previous numerical studies

676 The thermomechanical models presented in this study offer a dynamic representation of trajectories within the
677 wedge. Although the averaged trends in thermal structure and sediment trajectories remain consistent, there are
678 short-term dynamic fluctuations near the frontal thrust. These fluctuations contribute to a diverse range of sediment
679 paths along the depth of the incoming sediments. Miyakawa et al. (2019) conducted a similar study, modeling
680 vitrinite reflectance using Simple R_o and a stationary thermal field, which also resulted in an increase in thermal

Formatted: Font: 11 pt

Formatted: Font: 11 pt

Formatted: Font: 11 pt

Formatted: Font: 11 pt

Formatted: Font: 11 pt

Formatted: Font: 11 pt, Not Superscript/ Subscript

Formatted: Font: 11 pt

Formatted: Font: 11 pt

Formatted: Font: 11 pt

Formatted: Font: 11 pt

Formatted: Font: 11 pt

Formatted: Font: 11 pt

Formatted: Font: 11 pt

Formatted: Font: 11 pt, Not Superscript/ Subscript

Formatted: Font: 11 pt

Formatted: Font: 11 pt

Formatted: Font: 11 pt, Not Superscript/ Subscript

Formatted: Font: 11 pt

Formatted: Font: 11 pt

Formatted: Font: 11 pt

Formatted: Font: 11 pt, Not Superscript/ Subscript

Formatted: Font: 11 pt

Formatted: Font: 11 pt

Formatted: Font: 11 pt

Formatted: Font: 11 pt, English (United Kingdom)

Commented [um45]: In Response to R1C9 and R1C55

Commented [um46]: In Response to R1C10

Commented [um47]: In Response to R2C44

Formatted: Font color: Auto

Formatted: Border: Top: (No border), Bottom: (No border), Left: (No border), Right: (No border), Between : (No border), Tab stops: Not at 3.13" + 6.27"

681 maturity towards the continent and thermal maturity inversions due to thrusting. However, the use of Simple%R_o
682 led to premature saturation and the disappearance of thermal maturity variations at a shallower depth in their model.

683 We can compare our findings with other geodynamic models that examine the thermal structure of the wedge,
684 although there are only a limited number of numerical models of thermal maturity in wedges. Pajang et al. (2022)
685 recently investigated the distribution of the brittle-ductile transition in wedges and proposed a region dominated by
686 viscous shear near the backstop, with the wedge core reaching temperatures of 450°C and typically containing
687 forearc basins. Although trench sedimentation in our model does not result in the formation of forearc basins, the
688 overall flattening of the wedge slope and the high vitrinite reflectance in the core align with consistent structures.
689 Moreover, the presence of highly mature sediments in the wedge core suggests compacted sediments with greater
690 strength and higher P-wave velocity. Although empirical studies have shown a strong correlation between V_p and
691 thermal maturity estimates for depths of up to 4 km (Baig et al., 2016, Mallick et al. 1995), the exact nature of this
692 correlation may vary depending on the specific location. Nevertheless, the patterns of thermal maturity values in
693 the wedge core in our models also correspond to the patterns of P-wave velocity observed in the Nankai and
694 Hikurangi margins (Górszczyk et al., 2019; Nakanishi et al., 2018; Dewing and Sanei, 2009; Arai et al., 2020).

695 Two modes of sediment trajectory evolution, from incoming sediment to their position inside the wedge, are
696 generally considered; depth dependence sediment trajectories, as observed in studies by Mulugeta and Koyi, (1992)
697 and Hori and Sakaguchi (2011), and crossover exhumation pathways, as illustrated by Konstantinovskaia et al.
698 (2005) and Miyakawa (2019). We consider the latter as non-stationary sediment trajectories that vary with time
699 and cut across sediment trajectories of sediments previously located at the same spatial position. Our models show
700 that both modes of sediment trajectories are valid, and that changes in trajectory patterns leading to path crossovers
701 are controlled by the horizontal distance of sediments from the frontal thrust. Starting at a threshold distance from

Commented [um48]: In Response to R2C34

Commented [um49]: In Response to R1C50

Commented [um50]: In Response to R2C42

Formatted: Font: 11 pt, Font color: Text 1

Formatted: Font color: Auto

Formatted: Border: Top: (No border), Bottom: (No border), Left: (No border), Right: (No border), Between : (No border), Tab stops: Not at 3.13" + 6.27"

702 the trench, sediments at different depths follow laminar paths along different trajectories within the wedge.
703 Laminar-type trajectories can be reproduced in a broad range of simulations and are particularly common in models
704 with low sedimentation and décollement strengths. However, the depth dependence of sedimentary paths varies
705 periodically as a function of distance from the trench of specific sedimentary packages (Fig. 5). This effect, which
706 is particularly marked in the neighbourhood of the frontal thrust, explains the crossover paths for incoming
707 sedimentary packages at similar depths but different horizontal locations (Konstantinovskaia et al. 2005).
708 Therefore, thrust faults in the wedge act as the primary agent controlling whether sediments sustain depth-
709 controlled laminar flow or sediment mixing.

710 **5.4 Comparisons to natural wedges**

711 Our models achieve thermal maturity distributions that are in good agreement with their natural analogues, despite
712 several relevant assumptions. Our models are very simplified with regard to their natural analogues, with
713 assumptions such as no elasticity, predefined décollement, no erosion, and simple and uniform rheology. Also, our
714 models have an insufficient resolution for small-scale fault activity and lack empirical relations to simulate the
715 compaction of sediments and multiscale fluid flow. Although these assumptions hinder a wholesale comparison
716 between our simulations and natural examples of accretionary wedges, we still find an acceptable agreement
717 between our model and natural observations, primarily due to simulations that have a temperature evolution
718 assimilating empirical data and a fine spatiotemporal resolution. Our estimated R_o values for the model are in
719 very good agreement with those measured for the borehole C0002 Nankai accretionary wedge by Fukuchi et al.
720 2009 (Fig. 9). The maximum exposure temperature estimated from the observed thermal maturity for the C0002
721 borehole also strongly correlates with maximum temperatures recorded on markers in the model with similar
722 thermal maturity with 95% confidence (Fig. S17). However, our result is reliant on the empirical thermal
723 conductivity profiles estimated for the C0002 borehole, which does not show any large thermal discontinuity

3535

Commented [um51]: In Response to R1C8 , R1C49, R1C58, R2C37

Commented [um52]: In Response to R1C10

Formatted: Font color: Auto

Formatted: Border: Top: (No border), Bottom: (No border), Left: (No border), Right: (No border), Between : (No border), Tab stops: Not at 3.13" + 6.27"

724 between the forearc basin and inner wedge that has been observed in fossil accretionary wedges (e.g., Underwood
725 et al. 1989).

726 Landward increase in thermal maturity is well documented in studies of the Japan trench, at the Miura–Boso plate
727 subduction margin, the fold and thrust belts Western Foothills complex in western Taiwan, the Mesozoic
728 accretionary prism in the Franciscan subduction complex in northern California, as well as Cretaceous Shimanto
729 accretionary complex in Nankai subduction margin (Yamamoto et al. 2017; Sakaguchi et al. 2007; Underwood et
730 al. 1989; Sakaguchi, 1999). The natural wedges mentioned above display vitrinite reflectance values with
731 maximum %R_o values ranging from 0.2 to 4.0 near the surface, which is generally much higher than the near-
732 surface %R_o values observed in our models. Underwood et al. (1989) suggested that this discrepancy is likely due
733 to the ongoing process of progressive exhumation and erosion, leading to the exposure of deeper sections of the
734 accretionary prism over time. As a result, younger wedges, such as those found in the Miura–Boso plate subduction
735 margin, exhibit a much closer resemblance to the %R_o values near the surface of our our models.

736 On-fault increases in vitrinite reflectance are well also documented in nature, as for boreholes C0004 and C0007,
737 which sample the megasplay fault in Nankai accretionary margin (Sakaguchi et al., 2011). The vitrinite reflectance
738 data from the megasplay and frontal thrusts in Nankai indicate the faults reach a temperature well in excess of
739 300°C during an earthquake, much larger than the background thermal field. Therefore, on-fault increases in
740 thermal maturity are comparatively smaller in our simulations and lack the marked increase in %R_o observed at
741 fault sites in nature. We consider this is due to a discrepancy in the rate of change of thermal diffusion occurring
742 in simulated thrusts, given that our models develop much wider fault zones than their natural equivalents. For
743 instance, the location of megasplay fault in C0007 borehole exhibits an unevenness within the high-reflectance
744 zone with a maximum %R_o ~1.9 (Sakaguchi et al., 2011). This is in line with the prediction by Fulton and Harris
745 (2012) about the impact of fault thickness on change in vitrinite reflectance. Natural observations also exhibit a

Formatted: Font color: Auto

Formatted: Border: Top: (No border), Bottom: (No border), Left: (No border), Right: (No border), Between : (No border), Tab stops: Not at 3.13" + 6.27"

746 much higher incidence of on-fault increase in thermal maturity compared to our simulations, given that our models
747 do not have sufficient spatial resolution to capture the large number of thin faults that develop inside the wedge.
748 Natural examples of fault-block inversion have been well-documented in natural settings, providing evidence of
749 past thrust activity preserved in the shallower sections of the Nankai accretionary wedge. Sakaguchi (1999) reported
750 the presence of step increments of thermal maturity, similar to increments in vitrinite reflectance in Fig. 3 and 4
751 across the faults. Other examples are the fault block inversion along the Fukase Fault in the Shimanto accretionary
752 wedge (Ohmori et al., 1997) and the inversion beneath the forearc basin in the Nankai accretionary wedge (Fukuchi
753 et al., 2017).

Commented [um53]: In Response to R2C40

754 Our study highlights that paleo-thermal anomalies that extend laterally beyond the average thrust spacing have a
755 significantly higher likelihood of being retained in the final thermal maturity record of the wedge. This allows
756 several inferences. For example, the subduction of the Cretaceous ridge, as identified by Underwood et al. (1993)
757 and Sakaguchi (1999), must have caused a substantial alteration in thermal maturity during the Kula-Pacific
758 subduction in order to be discernible in vitrinite reflectance records. Likewise, we can anticipate the preservation
759 of the paleo-thermal anomaly near Ashizuri in the southern Nankai wedge, which has high thrust frequency, in
760 contrast to that at the Muroto transect, where thrust sheets are widely spaced. In the case of the accretionary wedge
761 adjacent to the Boso peninsula, Kamiya et al. (2017) proposed the emplacement of an ophiolite complex beneath
762 the Miura group. Our findings indicate that the preservation of the thermal-advection heating event coincided with
763 a decrease in trench sedimentation. This likely led to an increase in the thrust frequency, which facilitated the
764 preservation of the thermal-advection heating event in the thermal maturity data.

Formatted: Font: 11 pt

Formatted: Font: 11 pt, Not Bold, Font color: Text 1

Formatted: Font: 11 pt

Formatted: Font color: Auto

Formatted: Border: Top: (No border), Bottom: (No border), Left: (No border), Right: (No border), Between : (No border), Tab stops: Not at 3.13" + 6.27"

6. Conclusion

766 This study demonstrates how contractional faults alter the paths of sediments as they accrete and how this
767 fundamentally controls the distribution of the thermal maturity of sediments in accretionary wedges and emphasizes

768 the role that sedimentation rate and interplate contact strength have in such distribution. The increased resolution
769 of our approach leads to findings that have relevant implications. For example, the geothermal history that can be
770 retrieved from the thermal maturity of sediments in drills, i.e., at the shallow wedge, provides, at best, an incomplete
771 record that is skewed towards the thermal evolution of sediments near the trench. Coevally, relevant sectors of
772 sediments located further seaward, when not subducted, follow high-maturity paths that overprint their antecedent
773 thermal history. Finally, this study also provides a first-order uncertainty measure for the thermal maturity of
774 sediments based on the diversity in their trajectory.

Formatted: Font: 11 pt, English (United Kingdom)

776 **Competing interests**

777 The authors declare that they have no conflict of interest.

Formatted: Font: 11 pt

Formatted: Font: 11 pt, English (United Kingdom)

Formatted: Font: 11 pt

778 **References**

Formatted: Font: 11 pt, English (United Kingdom)

Formatted: Font: 11 pt

Formatted: Font: Not Bold

779 Arai, R., Kodaira, S., Henrys, S., Bangs, N., Obana, K., Fujie, G., et al. (2020). Three-dimensional P-wave velocity
780 structure of the northern Hikurangi margin from the NZ3D experiment: Evidence for fault-bound anisotropy. *Journal of*
781 *Geophysical Research, [Solid Earth]*, 125(12). <https://doi.org/10.1029/2020jb020433>

782 Argo. (2022). Argo float data and metadata from Global Data Assembly Centre (Argo GDAC) [Data set]. SEANOE.
783 <https://doi.org/10.17882/42182>

784 Bostick, N. H., & Pawlewicz, M. J. (1984). Paleotemperatures based on vitrinite reflectance of shales and limestone in
785 igneous dike aureoles in the Upper Cretaceous Pierre shale, Walsenburg, Colorado. Retrieved from
786 <http://archives.datapages.com/data/rmag/SourceRocks84/bostick.pdf>

787 Burg, J. P., & Gerya, T. V. (2005). The role of viscous heating in Barrovian metamorphism of collisional orogens:
788 thermomechanical models and application to the Lepontine Dome in the Central Alps. *Journal of Metamorphic*
789 *Geology*, 23(2), 75–95.

Formatted: Font color: Auto

Formatted: Border: Top: (No border), Bottom: (No border), Left: (No border), Right: (No border), Between : (No border), Tab stops: Not at 3.13" + 6.27"

790 Burnham, A. K., & Sweeney, J. J. (1989). A chemical kinetic model of vitrinite maturation and reflectance.
791 *Geochimica et Cosmochimica Acta*, 53(10), 2649–2657.

792 Byrne, T., & Fisher, D. (1990). Evidence for a weak and overpressured décollement beneath sediment-dominated
793 accretionary prisms. *Journal of Geophysical Research*. <https://doi.org/10.1029/jb095ib06p09081>

794 Davis, D., Suppe, J., & Dahlen, F. A. (1983). Mechanics of fold and thrust belts and accretionary wedges. *Journal of*
795 *Geophysical Research*. <https://doi.org/10.1029/JB088iB02p01153>

796 Dewing, K., & Sanei, H. (2009). Analysis of large thermal maturity datasets: Examples from the Canadian Arctic
797 Islands. *International Journal of Coal Geology*, 77(3), 436–448.

798 Dominguez, S., Malavieille, J., & Lallemand, S. E. (2000). Deformation of accretionary wedges in response to
799 seamount subduction: Insights from sandbox experiments. *Tectonics*, 19(1), 182–196.

800 Ferreira Mählmann, R., & Le Bayon, R. (2016). Vitrinite and vitrinite-like solid bitumen reflectance in thermal
801 maturity studies: Correlations from diagenesis to incipient metamorphism in different geodynamic settings.
802 *International Journal of Coal Geology*, 157, 52–73.

803 Fillon, C., Huisman, R. S., & van der Beek, P. (2012). Syntectonic sedimentation effects on the growth of fold and
804 thrust belts. *Geology*, 41(1), 83–86.

805 Fukuchi, R., Yamaguchi, A., Yamamoto, Y., & Ashi, J. (2017). Paleothermal structure of the Nankai inner
806 accretionary wedge estimated from vitrinite reflectance of cuttings. *Geochemistry, Geophysics, Geosystems*, 18(8),
807 3185–3196.

808 Gerya, T. (2019). *Introduction to Numerical Geodynamic Modelling*. Cambridge University Press.

809 Gerya, T. V., & Yuen, D. A. (2003). Characteristics-based marker-in-cell method with conservative finite-differences
810 schemes for modeling geological flows with strongly variable transport properties. *Physics of the Earth and Planetary*
811 *Interiors*, 140(4), 293–318.

812 Giunchi, C., & Ricard, Y. (1999). High-pressure/low-temperature metamorphism and the dynamics of an accretionary
813 wedge. *Geophysical Journal International*, 136(3), 620–628.

814 Górszczyk, A., Operto, S., Schenini, L., & Yamada, Y. (2019). Crustal-scale depth imaging via joint full-waveform

Formatted: Font color: Auto

Formatted: Border: Top: (No border), Bottom: (No border), Left: (No border), Right: (No border), Between : (No border), Tab stops: Not at 3.13" + 6.27"

815 inversion of ocean bottom seismometer data and pre-stack depth migration of multichannel seismic data: a case study
816 from the eastern Nankai Trough. *Solid Earth*, 10(3), 765–784.

817 Hori, T., & Sakaguchi, H. (2011). Mechanism of décollement formation in subduction zones. *Geophysical Journal*
818 *International*, 187(3), 1089–1100.

819 Konstantinovskaia, E. (2005). Erosion and exhumation in accretionary orogens: Experimental and geological
820 approaches. *Geochemistry, Geophysics, Geosystems*. Retrieved from
821 <https://agupubs.onlinelibrary.wiley.com/doi/abs/10.1029/2004GC000794>

822 Konstantinovskaia, E., & Malavieille, J. (2005). Erosion and exhumation in accretionary orogens: Experimental and
823 geological approaches. *Geochemistry, Geophysics, Geosystems*. <https://doi.org/10.1029/2004gc000794>

824 Korup, O., Hayakawa, Y., Codilean, A. T., Matsushi, Y., Saito, H., Oguchi, T., & Matsuzaki, H. (2014). Japan's
825 sediment flux to the Pacific Ocean revisited. *Earth Science Reviews*, 135, 1–16.

826 Luján, M., Rossetti, F., Storti, F., Ranalli, G., & A. Socquet. (2010). Flow trajectories in analogue viscous orogenic
827 wedges: Insights on natural orogens. *Tectonophysics*, 484(1), 119–126.

828 Malavieille, J., & Trullenque, G. (2009). Consequences of continental subduction on forearc basin and accretionary
829 wedge deformation in SE Taiwan: Insights from analogue modeling. *Tectonophysics*, 466(3), 377–394.

830 Mannu, U., Ueda, K., Willett, S. D., Gerya, T. V., & Strasser, M. (2016). Impact of sedimentation on evolution of
831 accretionary wedges: Insights from high-resolution thermomechanical modeling. *Tectonics*.
832 <https://doi.org/10.1002/2016tc004239>

833 Mannu, U., Ueda, K., Willett, S. D., Gerya, T. V., & Strasser, M. (2017). Stratigraphic signatures of forearc basin
834 formation mechanisms. *Geochemistry, Geophysics, Geosystems*, 18(6), 2388–2410.

835 Mary, B. C. L., Maillot, B., & Leroy, Y. M. (2013). Deterministic chaos in frictional wedges revealed by convergence
836 analysis. *International Journal for Numerical and Analytical Methods in Geomechanics*.
837 <https://doi.org/10.1002/nag.2177>

838 Menant, A., Angiboust, S., Gerya, T., Lacassin, R., Simoes, M., & Grandin, R. (2020). Transient stripping of
839 subducting slabs controls periodic forearc uplift. *Nature Communications*, 11(1), 1823.

Formatted: Font color: Auto

Formatted: Border: Top: (No border), Bottom: (No border), Left: (No border), Right: (No border), Between : (No border), Tab stops: Not at 3.13" + 6.27"

840 Miyakawa, A., Kinoshita, M., Hamada, Y., & Otsubo, M. (2019). Thermal maturity structures in an accretionary wedge
841 by a numerical simulation. *Progress in Earth and Planetary Science*, 6(1), 8.

842 Mugnier, J. L., Baby, P., Colletta, B., Vinour, P., Bale, P., & Leturmy, P. (1997). Thrust geometry controlled by
843 erosion and sedimentation: A view from analogue models. *Geology*, 25(5), 427–430.

844 Mulugeta, G., & Koyi, H. (1992). Episodic accretion and strain partitioning in a model sand wedge. *Tectonophysics*,
845 202(2), 319–333.

846 Nakanishi, A., Takahashi, N., Yamamoto, Y., Takahashi, T., Citak, S. O., Nakamura, T., et al. (2018). Three-
847 dimensional plate geometry and P-wave velocity models of the subduction zone in SW Japan: Implications for
848 seismogenesis. *Geology and Tectonics of Subduction Zones: A Tribute to Gaku Kimura: Geological Society of America
849 Special Paper*, 534, 69–86.

850 Ohmori, K., Taira, A., Tokuyama, H., Sakaguchi, A., Okamura, M., & Aihara, A. (1997). Paleothermal structure of the
851 Shimanto accretionary prism, Shikoku, Japan: Role of an out-of-sequence thrust. *Geology*, 25(4), 327–330.

852 Platt, J. P. (1986). Dynamics of orogenic wedges and the uplift of high-pressure metamorphic rocks. *GSA Bulletin*,
853 97(9), 1037–1053.

854 Platt, J. P. (1993). Exhumation of high-pressure rocks: a review of concepts and processes. *Terra Nova*, 5(2), 119–133.

855 Quigley, T. M., & Mackenzie, A. S. (1988). The temperatures of oil and gas formation in the sub-surface. *Nature*,
856 333(6173), 549–552.

857 Rabinowitz, H. S., Savage, H. M., Polissar, P. J., Rowe, C. D., & Kirkpatrick, J. D. (2020). Earthquake slip surfaces
858 identified by biomarker thermal maturity within the 2011 Tohoku-Oki earthquake fault zone. *Nature Communications*,
859 11(1), 533.

860 Ranalli, G. (1995). *Rheology of the Earth*. Springer Science & Business Media.

861 Ruh, J. B. (2017). Effect of fluid pressure distribution on the structural evolution of accretionary wedges. *Terra Nova*,
862 29(3), 202–210.

863 Ruh, J. B. (2020a). Numerical modeling of tectonic underplating in accretionary wedge systems. *Geosphere*, 16(6),
864 1385–1407.

4141

Formatted: Font color: Auto

Formatted: Border: Top: (No border), Bottom: (No border), Left: (No border), Right: (No border), Between : (No border), Tab stops: Not at 3.13" + 6.27"

865 Ruh, J. B. (2020b). Numerical modelling of tectonic underplating in accretionary wedges (p. 5607).

866 Sakaguchi, A., Yanagihara, A., Ujiie, K., Tanaka, H., & Kameyama, M. (2007). Thermal maturity of a fold–thrust belt
867 based on vitrinite reflectance analysis in the Western Foothills complex, western Taiwan. *Tectonophysics*, *443*(3), 220–
868 232.

869 Sakaguchi, A., Chester, F., Curewitz, D., Fabbri, O., Goldsby, D., Kimura, G., et al. (2011). Seismic slip propagation to
870 the updip end of plate boundary subduction interface faults: Vitrinite reflectance geothermometry on Integrated Ocean
871 Drilling Program NanTro SEIZE cores. *Geology*. <https://doi.org/10.1130/g31642.1>

872 Schmoker, J. W., & Gautier, D. L. (1988). Sandstone porosity as a function of thermal maturity. *Geology*, *16*(11),
873 1007–1010.

874 Simpson, G. D. H. (2010). Formation of accretionary prisms influenced by sediment subduction and supplied by
875 sediments from adjacent continents. *Geology*, *38*(2), 131–134.

876 Storti, F., & Meclay, K. (1995). Influence of syntectonic sedimentation on thrust wedges in analogue models.
877 [https://doi.org/10.1130/0091-7613\(1995\)023<0999](https://doi.org/10.1130/0091-7613(1995)023<0999)

878 Sugihara, T., Kinoshita, M., Araki, E., Kimura, T., Kyo, M., Namba, Y., et al. (2014). Re-evaluation of temperature at
879 the updip limit of locked portion of Nankai megasplay inferred from IODP Site C0002 temperature observatory. *Earth*,
880 *Planets and Space*. <https://doi.org/10.1186/1880-5981-66-107>

881 Tesei, T., Laeroix, B., & Colletini, C. (2015). Fault strength in thin skinned tectonic wedges across the smectite-illite
882 transition: Constraints from friction experiments and critical tapers. *Geology*, *43*(10), 923–926.

883 Tissot, B. P., & Welte, D. H. (2013). *Petroleum Formation and Occurrence*. Springer Science & Business Media.

884 Tissot, B. P., Pelet, R., & Ungerer, P. H. (1987). Thermal History of Sedimentary Basins, Maturation Indices, and
885 Kinetics of Oil and Gas Generation. *AAPG Bulletin*, *71*(12), 1445–1466.

886 Tobin, H., Hirose, T., Saffer, D., Toezko, S., Maeda, L., Kubo, Y., et al. (2015). Site C0002. *Proceedings of the IODP*.
887 <https://doi.org/10.2204/iodp.proc.348.103.2015>

888 Tobin, H. J., & Saffer, D. M. (2009). Elevated fluid pressure and extreme mechanical weakness of a plate boundary
889 thrust, Nankai Trough subduction zone. *Geology*, *37*(8), 679–682.

4242

Formatted: Font color: Auto

Formatted: Border: Top: (No border), Bottom: (No border), Left: (No border), Right: (No border), Between : (No border), Tab stops: Not at 3.13" + 6.27"

890 Totten, M. W., & Blatt, H. (1993). Alterations in the non-clay mineral fraction of pelitic rocks across the diagenetic to
891 low-grade metamorphic transition, Ouachita Mountains, Oklahoma and Arkansas. *Journal of Sedimentary Research*,
892 63(5), 899–908.

893 Underwood, M. B., Laughland, M. M., Byrne, T., Hibbard, J. P., & DiTullio, L. (1992). Thermal evolution of the
894 Tertiary Shimanto Belt, Muroto Peninsula, Shikoku, Japan. *The Island Arc*. [https://doi.org/10.1111/j.1440-](https://doi.org/10.1111/j.1440-1738.1992.tb00064.x)
895 [1738.1992.tb00064.x](https://doi.org/10.1111/j.1440-1738.1992.tb00064.x)

896 Wang, K., & He, J. (1999). Mechanics of low-stress forearcs: Nankai and Cascadia. *Journal of Geophysical Research*,
897 *[Solid Earth]*, 104(B7), 15191–15205.

898 Waples, D. W. (1981). *Organic Geochemistry for Exploration Geologists*. Springer Netherlands.

899 Wenk, L., & Huhn, K. (2013). The influence of an embedded viscoelastic–plastic layer on kinematics and mass
900 transport pattern within accretionary wedges. *Tectonophysics*, 608, 653–666.

901 Willett, S. (1992). Dynamic and kinematic growth and change of a Coulomb wedge. *McClay, K. R.*, 19–31.

902 Willett, S., Beaumont, C., & Fullsack, P. (1993). Mechanical model for the tectonics of doubly vergent compressional
903 orogens. *Geology*. [https://doi.org/10.1130/0091-7613\(1993\)021<0371:MMFTTO>2.3.CO](https://doi.org/10.1130/0091-7613(1993)021<0371:MMFTTO>2.3.CO)

904 Willett, S. D. (1999). Orogeny and orography: The effects of erosion on the structure of mountain belts. *Journal of*
905 *Geophysical Research*, 104, 28957.

906 Yamamoto, Y., Hamada, Y., Kamiya, N., Ojima, T., Chiyonobu, S., & Saito, S. (2017). Geothermal structure of the
907 Miura–Boso plate subduction margin, central Japan. *Tectonophysics*, 710–711, 81–87.

908

909 1. Arai, R., Kodaira, S., Henrys, S., Bangs, N., Obana, K., Fujie, G., ... & NZ3D Team. (2020). Three-dimensional P
910 wave velocity structure of the Northern Hikurangi margin from the NZ3D experiment: Evidence for fault-bound
911 anisotropy. *Journal of Geophysical Research: Solid Earth*, 125(12), e2020JB020433.

Formatted: Font color: Auto

Formatted: Border: Top: (No border), Bottom: (No border), Left: (No border), Right: (No border), Between : (No border), Tab stops: Not at 3.13" + 6.27"

- 912 2. Baig, I., Faleide, J. I., Jahren, J., & Mondol, N. H. (2016). Cenozoic exhumation on the southwestern Barents Shelf:
913 Estimates and uncertainties constrained from compaction and thermal maturity analyses. *Marine and Petroleum*
914 *Geology*, 73, 105-130.
- 915 3. Bostick, N. H., & Pawlewicz, M. J. (1984). Paleotemperatures based on vitrinite reflectance of shales and limestone
916 in igneous dike aureoles in the Upper Cretaceous Pierre shale, Walsenburg, Colorado.
- 917 4. Burnham, A. K., & Sweeney, J. J. (1989). A chemical kinetic model of vitrinite maturation and reflectance. *Geo-*
918 *chimica et Cosmochimica Acta*, 53(10), 2649-2657.
- 919 5. Chi, W. C., & Reed, D. L. (2008). Evolution of shallow, crustal thermal structure from subduction to collision: An
920 example from Taiwan. *Geological Society of America Bulletin*, 120(5-6), 679-690.
- 921 6. Clauser, C., & Huenges, E. (1995). Thermal conductivity of rocks and minerals. *Rock physics and phase relations:*
922 *a handbook of physical constants*, 3, 105-126.
- 923 7. Davis, D., Suppe, J., & Dahlen, F. A. (1983). Mechanics of fold-and-thrust belts and accretionary wedges. *Journal*
924 *of Geophysical Research: Solid Earth*, 88(B2), 1153-1172.
- 925 8. DeMets, C., Gordon, R. G., & Argus, D. F. (2010). Geologically current plate motions. *Geophysical journal inter-*
926 *national*, 181(1), 1-80.
- 927 9. Dewing, K., & Sanei, H. (2009). Analysis of large thermal maturity datasets: Examples from the Canadian Arctic
928 Islands. *International Journal of Coal Geology*, 77(3-4), 436-448.
- 929 10. Dominguez, Stephane, Jacques Malavieille, and Serge E. Lallemand. "Deformation of accretionary wedges in re-
930 sponse to seamount subduction: Insights from sandbox experiments." *Tectonics* 19.1 (2000): 182-196.
- 931 11. Fernández-Blanco, D., Mannu, U., Cassola, T., Bertotti G., & Willett SD (2020). Sedimentation and viscosity con-
932 trols on forearc high growth. *Basin Research*. <https://doi.org/10.1111/bre.12518>
- 933 12. Fillon, C., & van der Beek, P. (2012). Post-orogenic evolution of the southern Pyrenees: Constraints from inverse
934 thermo-kinematic modelling of low-temperature thermochronology data. *Basin Research*, 24(4), 418-436.

Formatted: Font color: Auto

Formatted: Border: Top: (No border), Bottom: (No border), Left: (No border), Right: (No border), Between : (No border), Tab stops: Not at 3.13" + 6.27"

- 935 13. Fukuchi, M., Nii, T., Ishimaru, N., Minamino, A., Hara, D., Takasaki, I., ... & Tsuda, M. (2009). Valproic acid in-
936 duces up-or down-regulation of gene expression responsible for the neuronal excitation and inhibition in rat cortical
937 neurons through its epigenetic actions. *Neuroscience research*, 65(1), 35-43.
- 938 14. Fukuchi, R., Yamaguchi, A., Yamamoto, Y., & Ashi, J. (2017). Paleothermal structure of the Nankai inner accre-
939 tionary wedge estimated from vitrinite reflectance of cuttings. *Geochemistry, Geophysics, Geosystems*, 18(8), 3185-
940 3196.
- 941 15. Gerya, T. V., & Yuen, D. A. (2003). Characteristics-based marker-in-cell method with conservative finite-differ-
942 ences schemes for modeling geological flows with strongly variable transport properties. *Physics of the Earth and*
943 *Planetary Interiors*, 140(4), 293-318.
- 944 16. Gerya, T. V., & Yuen, D. A. (2003). Rayleigh–Taylor instabilities from hydration and melting propel ‘cold plumes’
945 at subduction zones. *Earth and Planetary Science Letters*, 212(1-2), 47-62.
- 946 17. Górszczyk, A., Operto, S., Schenini, L., & Yamada, Y. (2019). Crustal-scale depth imaging via joint full-waveform
947 inversion of ocean-bottom seismometer data and pre-stack depth migration of multichannel seismic data: a case
948 study from the eastern Nankai Trough. *Solid Earth*, 10(3), 765-784.
- 949 18. Heki, K., Miyazaki, S. I., Takahashi, H., Kasahara, M., Kimata, F., Miura, S., ... & An, K. D. (1999). The Amurian
950 Plate motion and current plate kinematics in eastern Asia. *Journal of Geophysical Research: Solid Earth*, 104(B12),
951 29147-29155.
- 952 19. Henrys, S. A., Ellis, S., & Uruski, C. (2003). Conductive heat flow variations from bottom-simulating reflectors on
953 the Hikurangi margin, New Zealand. *Geophysical Research Letters*, 30(2).
- 954 20. Hori, T., & Sakaguchi, H. (2011). Mechanism of décollement formation in subduction zones. *Geophysical Journal*
955 *International*, 187(3), 1089-1100.
- 956 21. Kamiya, N., Yamamoto, Y., Wang, Q., Kurimoto, Y., Zhang, F., & Takemura, T. (2017). Major variations in vit-
957 rinite reflectance and consolidation characteristics within a post-middle Miocene forearc basin, central Japan: A
958 geodynamical implication for basin evolution. *Tectonophysics*, 710, 69-80.

Formatted: Font color: Auto

Formatted: Border: Top: (No border), Bottom: (No border), Left: (No border), Right: (No border), Between : (No border), Tab stops: Not at 3.13" + 6.27"

- 959 [22. Kimura, G., Hashimoto, Y., Kitamura, Y., Yamaguchi, A., & Koge, H. \(2014\). Middle Miocene swift migration of](#)
960 [the TTT triple junction and rapid crustal growth in southwest Japan: A review. *Tectonics*, 33\(7\), 1219-1238.](#)
- 961 [23. Konstantinovskaia, E., & Malavieille, J. \(2005\). Erosion and exhumation in accretionary orogens: Experimental and](#)
962 [geological approaches. *Geochemistry, Geophysics, Geosystems*, 6\(2\).](#)
- 963 [24. Konstantinovskaya, E., & Malavieille, J. \(2011\). Thrust wedges with décollement levels and syntectonic erosion: A](#)
964 [view from analog models. *Tectonophysics*, 502\(3-4\), 336-350.](#)
- 965 [25. Korup, O., Hayakawa, Y., Codilean, A. T., Matsushi, Y., Saito, H., Oguchi, T., & Matsuzaki, H. \(2014\). Japan's](#)
966 [sediment flux to the Pacific Ocean revisited. *Earth-Science Reviews*, 135, 1-16.](#)
- 967 [26. Lin, W., Fulton, P. M., Harris, R. N., Tadai, O., Matsubayashi, O., Tanikawa, W., & Kinoshita, M. \(2014\). Thermal](#)
968 [conductivities, thermal diffusivities, and volumetric heat capacities of core samples obtained from the Japan Trench](#)
969 [Fast Drilling Project \(JFAST\). *Earth, Planets and Space*, 66\(1\), 1-11.](#)
- 970 [27. Maehlmann, R. F., & Le Bayon, R. \(2016\). Vitrinite and vitrinite like solid bitumen reflectance in thermal maturity](#)
971 [studies: Correlations from diagenesis to incipient metamorphism in different geodynamic settings. *International*](#)
972 [Journal of Coal Geology](#), 157, 52-73.
- 973 [28. Malavieille, J., & Trullenque, G. \(2009\). Consequences of continental subduction on forearc basin and accretionary](#)
974 [wedge deformation in SE Taiwan: Insights from analogue modeling. *Tectonophysics*, 466\(3-4\), 377-394.](#)
- 975 [29. Mallick, R. K., & Raju, S. V. \(1995\). Thermal maturity evaluation by sonic log and seismic velocity analysis in](#)
976 [parts of Upper Assam Basin, India. *Organic Geochemistry*, 23\(10\), 871-879.](#)
- 977 [30. Mannu, U., Ueda, K., Willett, S. D., Gerya, T. V., & Strasser, M. \(2016\). Impact of sedimentation on evolution of](#)
978 [accretionary wedges: Insights from high-resolution thermomechanical modeling. *Tectonics*, 35\(12\), 2828-2846.](#)
- 979 [31. Mannu, U., Ueda, K., Willett, S. D., Gerya, T. V., & Strasser, M. \(2017\). Stratigraphic signatures of forearc basin](#)
980 [formation mechanisms. *Geochemistry, Geophysics, Geosystems*, 18\(6\), 2388-2410.](#)
- 981 [32. Menant, A., Angiboust, S., Gerya, T., Lacassin, R., Simoes, M., & Grandin, R. \(2020\). Transient stripping of sub-](#)
982 [ducting slabs controls periodic forearc uplift. *Nature communications*, 11\(1\), 1823.](#)

Formatted: Font color: Auto

Formatted: Border: Top: (No border), Bottom: (No border), Left: (No border), Right: (No border), Between : (No border), Tab stops: Not at 3.13" + 6.27"

- 983 [33. Miyakawa, A., Kinoshita, M., Hamada, Y., & Otsubo, M. \(2019\). Thermal maturity structures in an accretionary](#)
984 [wedge by a numerical simulation. *Progress in Earth and Planetary Science*, 6\(1\), 1-13.](#)
- 985 [34. Mugnier, J. L., Baby, P., Colletta, B., Vinour, P., Bale, P., & Leturmy, P. \(1997\). Thrust geometry controlled by](#)
986 [erosion and sedimentation: A view from analogue models. *Geology*, 25\(5\), 427-430.](#)
- 987 [35. Mulugeta, G., & Koyi, H. \(1992\). Episodic accretion and strain partitioning in a model sand wedge. *Tectonophysics*,](#)
988 [202\(2-4\), 319-333.](#)
- 989 [36. Nakanishi, A., Takahashi, N., Yamamoto, Y., Takahashi, T., Citak, S. O., Nakamura, T., ... & Kaneda, Y. \(2018\).](#)
990 [Three-dimensional plate geometry and P-wave velocity models of the subduction zone in SW Japan: Implications](#)
991 [for seismogenesis.](#)
- 992 [37. Nielsen, S. B., Clausen, O. R., & McGregor, E. \(2017\). basin% Ro: A vitrinite reflectance model derived from ba-](#)
993 [sin and laboratory data. *Basin Research*, 29, 515-536.](#)
- 994 [38. Ohmori, K., Taira, A., Tokuyama, H., Sakaguchi, A., Okamura, M., & Aihara, A. \(1997\). Paleothermal structure of](#)
995 [the Shimanto accretionary prism, Shikoku, Japan: Role of an out-of-sequence thrust. *Geology*, 25\(4\), 327-330.](#)
- 996 [39. Pajang, S., Khatib, M. M., Heyhat, M., Cubas, N., Bessiere, E., Letouzey, J., ... & Le Pourhiet, L. \(2022\). The dis-](#)
997 [tinct morphologic signature of underplating and seamounts in accretionary prisms, insights from thermomechanical](#)
998 [modeling applied to Coastal Iranian Makran. *Tectonophysics*, 845, 229617.](#)
- 999 [40. Platt, J. P. \(1986\). Dynamics of orogenic wedges and the uplift of high-pressure metamorphic rocks. *Geological*](#)
1000 [society of America bulletin, 97\(9\), 1037-1053.](#)
- 1001 [41. Rabinowitz, H. S., Savage, H. M., Polissar, P. J., Rowe, C. D., & Kirkpatrick, J. D. \(2020\). Earthquake slip surfaces](#)
1002 [identified by biomarker thermal maturity within the 2011 Tohoku-Oki earthquake fault zone. *Nature communica-*](#)
1003 [tions, 11\(1\), 533.](#)
- 1004 [42. Ruh, J. B. \(2020\). Numerical modeling of tectonic underplating in accretionary wedge systems. *Geosphere*, 16\(6\),](#)
1005 [1385-1407.](#)

Formatted: Font color: Auto

Formatted: Border: Top: (No border), Bottom: (No border), Left: (No border), Right: (No border), Between : (No border), Tab stops: Not at 3.13" + 6.27"

- 1006 [43. Sakaguchi, A. \(1999\). Thermal maturity in the Shimanto accretionary prism, southwest Japan, with the thermal](#)
1007 [change of the subducting slab: fluid inclusion and vitrinite reflectance study. *Earth and Planetary Science Letters*,](#)
1008 [173\(1-2\), 61-74.](#)
- 1009 [44. Sakaguchi, A., Chester, F., Curewitz, D., Fabbri, O., Goldsby, D., Kimura, G., ... & Yamaguchi, A. \(2011\). Seismic](#)
1010 [slip propagation to the updip end of plate boundary subduction interface faults: Vitrinite reflectance geothermome-](#)
1011 [try on Integrated Ocean Drilling Program NanTro SEIZE cores. *Geology*, 39\(4\), 395-398.](#)
- 1012 [45. Seno, T., Stein, S., & Gripp, A. E. \(1993\). A model for the motion of the Philippine Sea plate consistent with](#)
1013 [NUVEL-1 and geological data. *Journal of Geophysical Research: Solid Earth*, 98\(B10\), 17941-17948.](#)
- 1014 [46. Simpson, Guy DH. "Formation of accretionary prisms influenced by sediment subduction and supplied by sedi-](#)
1015 [ments from adjacent continents." *Geology* 38.2 \(2010\): 131-134.](#)
- 1016 [47. Storti, F., & McClay, K. \(1995\). Influence of syntectonic sedimentation on thrust wedges in analogue models. *Geol*](#)
- 1017 [48. Sugihara, T., Kinoshita, M., Araki, E., Kimura, T., Kyo, M., Namba, Y., ... & Thu, M. K. \(2014\). Re-evaluation of](#)
1018 [temperature at the updip limit of locked portion of Nankai megasplay inferred from IODP Site C0002 temperature](#)
1019 [observatory. *Earth, Planets and Space*, 66\(1\), 1-14.](#)
- 1020 [49. Suzuki, N., Matsubayashi, H., & Waples, D. W. \(1993\). A simpler kinetic model of vitrinite reflectance. *AAPG bul-*](#)
- 1021 [letin](#), 77(9), 1502-1508.
- 1022 [50. Sweeney, J. J., & Burnham, A. K. \(1990\). Evaluation of a simple model of vitrinite reflectance based on chemical](#)
1023 [kinetics. *AAPG bulletin*, 74\(10\), 1559-1570.](#)
- 1024 [51. Tesei, T., Cruciani, F., & Barchi, M. R. \(2021\). Gravity-driven deepwater fold-and-thrust belts as Critical Coulomb](#)
1025 [Wedges: Model limitations and the role of friction vs. fluid pressure. *Journal of Structural Geology*, 153, 104451.](#)
- 1026 [52. Totten, M. W., & Blatt, H. \(1993\). Alterations in the non-clay-mineral fraction of pelitic rocks across the diagenetic](#)
1027 [to low-grade metamorphic transition, Ouachita Mountains, Oklahoma and Arkansas. *Journal of Sedimentary Re-*](#)
1028 [search](#), 63(5), 899-908.
- 1029 [53. Turcotte, D. L., & Schubert, G. \(2002\). *Geodynamics*. Cambridge university press.](#)

Formatted: Font color: Auto

Formatted: Border: Top: (No border), Bottom: (No border), Left: (No border), Right: (No border), Between : (No border), Tab stops: Not at 3.13" + 6.27"

- 1030 54. Underwood, M. B., Moore, G. F., Taira, A., Klaus, A., Wilson, M. E., Fergusson, C. L., ... & Steurer, J. (2003).
1031 Sedimentary and tectonic evolution of a trench-slope basin in the Nankai subduction zone of southwest Japan. *Journal of Sedimentary Research*, 73(4), 589-602.
- 1032
- 1033 55. Underwood, M. B., O'Leary, J. D., & Strong, R. H. (1988). Contrasts in thermal maturity within terranes and across
1034 terrane boundaries of the Franciscan Complex, northern California. *The Journal of Geology*, 96(4), 399-415.
- 1035 56. Underwood, M. B. (1989). Temporal changes in geothermal gradient, Franciscan subduction complex,
1036 northern California. *Journal of Geophysical Research: Solid Earth*, 94(B3), 3111-3125.
- 1037 57. Wenk, L., & Huhn, K. (2013). The influence of an embedded viscoelastic-plastic layer on kinematics and mass
1038 transport pattern within accretionary wedges. *Tectonophysics*, 608, 653-666.
- 1039 58. Willett, S. D. (1992). Dynamic and kinematic growth and change of a Coulomb wedge. In *Thrust tectonics* (pp. 19-
1040 31). Dordrecht: Springer Netherlands.
- 1041 59. Yamano, M., Foucher, J. P., Kinoshita, M., Fisher, A., Hyndman, R. D., Leg, O. D. P., & Party, S. S. (1992). Heat
1042 flow and fluid flow regime in the western Nankai accretionary prism. *Earth and Planetary Science Letters*, 109(3-
1043 4), 451-462.
- 1044 60. Zhao, D., Wang, J., Huang, Z., & Liu, X. (2021). Seismic structure and subduction dynamics of the western Japan
1045 arc. *Tectonophysics*, 802, 228743.

Formatted: Font: 11 pt

Formatted: Font color: Auto

Formatted: Border: Top: (No border), Bottom: (No border), Left: (No border), Right: (No border), Between : (No border), Tab stops: Not at 3.13" + 6.27"

Table 3: Parameters for Easy% R_o , Simple% R_o and Basin% R_o vitrinite reflectance model.

S. No.	Stoichiometric Coefficient for Easy% R_o (X_{0i_Easy})	Activation Energy for Easy% R_o (kJ/mol) (E_{ai_Easy})	Stoichiometric Coefficient for Simple% R_o (X_{0i_Simple})	Activation Energy(E) for Simple% R_o (E_{ai_Simple})	Stoichiometric Coefficient for Basin% R_o (X_{0i_Basin})	Activation Energy(E) for Basin% R_o (kJ/mol) (E_{ai_Simple})
<u>1</u>	<u>0.0300</u>	<u>142256</u>	<u>1</u>	<u>1.38e5</u>	<u>0.0185</u>	<u>142256</u>
<u>2</u>	<u>0.0300</u>	<u>150624</u>			<u>0.0143</u>	<u>150624</u>
<u>3</u>	<u>0.0400</u>	<u>158992</u>			<u>0.0569</u>	<u>158992</u>
<u>4</u>	<u>0.0400</u>	<u>167360</u>			<u>0.0478</u>	<u>167360</u>
<u>5</u>	<u>0.0500</u>	<u>175728</u>			<u>0.0497</u>	<u>175728</u>
<u>6</u>	<u>0.0500</u>	<u>184096</u>			<u>0.0344</u>	<u>184096</u>
<u>7</u>	<u>0.0600</u>	<u>192464</u>			<u>0.0344</u>	<u>192464</u>
<u>8</u>	<u>0.0400</u>	<u>200832</u>			<u>0.0322</u>	<u>200832</u>
<u>9</u>	<u>0.0400</u>	<u>209200</u>			<u>0.0282</u>	<u>209200</u>
<u>10</u>	<u>0.0700</u>	<u>217568</u>			<u>0.0062</u>	<u>217568</u>
<u>11</u>	<u>0.0600</u>	<u>225936</u>			<u>0.1155</u>	<u>225936</u>
<u>12</u>	<u>0.0600</u>	<u>234304</u>			<u>0.1041</u>	<u>234304</u>
<u>13</u>	<u>0.0600</u>	<u>242672</u>			<u>0.1023</u>	<u>242672</u>
<u>14</u>	<u>0.0500</u>	<u>251040</u>			<u>0.076</u>	<u>251040</u>
<u>15</u>	<u>0.0500</u>	<u>259408</u>			<u>0.0593</u>	<u>259408</u>
<u>16</u>	<u>0.0400</u>	<u>267776</u>			<u>0.0512</u>	<u>267776</u>
<u>17</u>	<u>0.0300</u>	<u>276144</u>			<u>0.0477</u>	<u>276144</u>
<u>18</u>	<u>0.0200</u>	<u>284512</u>			<u>0.0086</u>	<u>284512</u>
<u>19</u>	<u>0.0200</u>	<u>292880</u>			<u>0.0246</u>	<u>292880</u>
<u>20</u>	<u>0.0100</u>	<u>301248</u>			<u>0.0096</u>	<u>301248</u>
$A_{Easy} = 1e13$ and $\%R_{o0} = 0.2$, $A_{Simple} = 1e13$ and $\%R_{o0} = 0.2$, $A_{Basin} = 9.7029e12$ and $\%R_{o0} = 0.2104$						

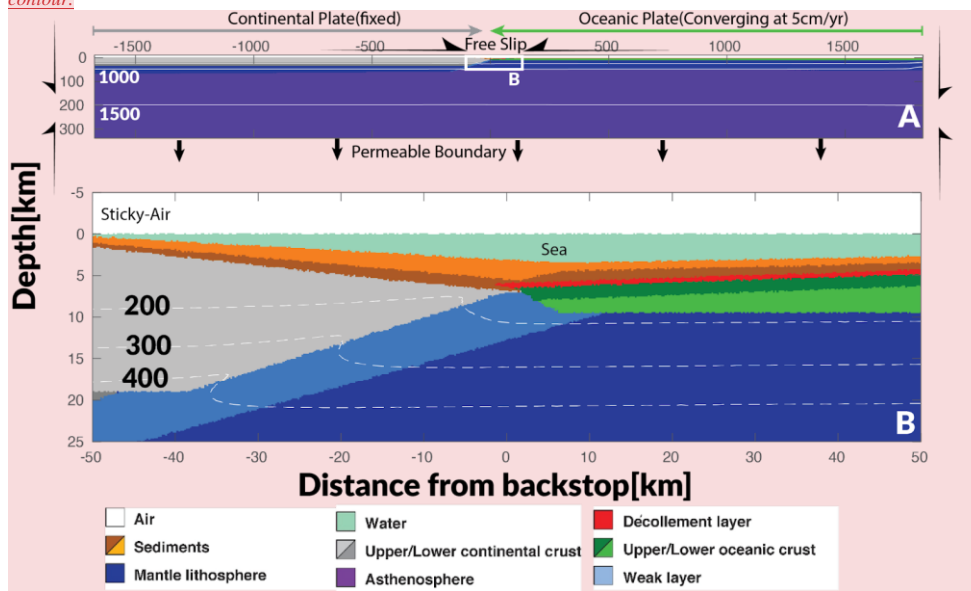
Formatted: Font color: Auto

Formatted: Border: Top: (No border), Bottom: (No border), Left: (No border), Right: (No border), Between : (No border), Tab stops: Not at 3.13" + 6.27"

1063 **List of Figures**

1064 **Fig. 1:**

1065 Initial model setup. A. The lithological and geothermal map of the whole computational domain with boundary conditions. B.
1066 The zoomed lithological and geothermal map of the inset illustrates the junction of continental and oceanic plates. The colors
1067 represent different lithology of the materials used in the models, with upper and lower crust represented by light and dark
1068 grey, upper and lower oceanic crust represented by dark and light green. The arrows around the computational domain
1069 represent the imposed boundary conditions, while the white contour lines (dashed in the zoomed panel) show the geothermal
1070 gradients used for the initial model. The numbers on the white contour lines represent the temperature values in °C for the
1071 contour.



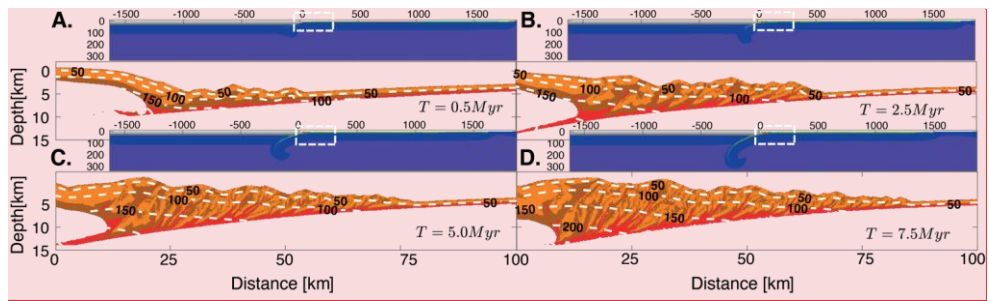
Formatted: Font: 11 pt

Formatted: Font color: Auto

Formatted: Border: Top: (No border), Bottom: (No border), Left: (No border), Right: (No border), Between : (No border), Tab stops: Not at 3.13" + 6.27"

5454

1080 **Fig. 2:**
1081 *Typical thermomechanical evolution of the accretionary wedge for model M_0^7 at (a) 0.5*
1082 *Myr (b) 2.5 Myr (c) 5.0 Myr (d) 7.5 Myr. Similar Figures for other models have been illustrated in supplementary images. The*
1083 *colormap for the panels is same as Figure 1.*
1084



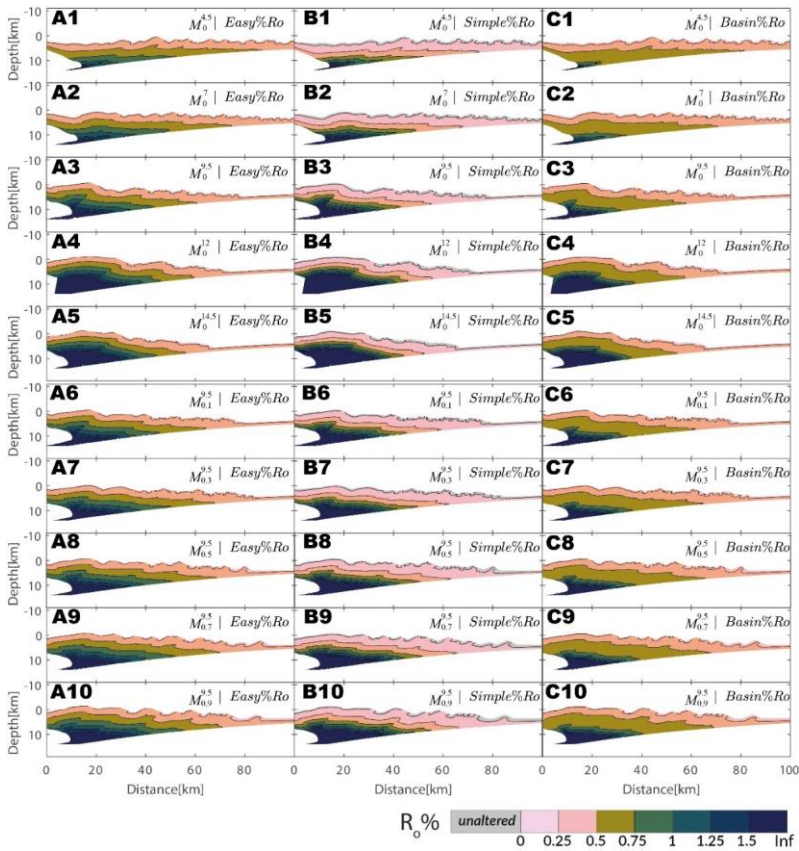
Commented [um56]: In Response to R2C14

Formatted: Font color: Auto

Formatted: Border: Top: (No border), Bottom: (No border), Left: (No border), Right: (No border), Between : (No border), Tab stops: Not at 3.13" + 6.27"

§§§§

Fig. 3: Distribution of thermal maturity for different models at $\sim 7.56.0$ Myr (3.5 Myr of thermal maturation). Panels A1-A5 show the thermal maturity distribution (computed using Easy%Ro) in subduction wedges of models as a function of décollement strength $M_0^2 - M_0^{22}$, respectively. A6-A10 show the thermal maturity distribution in subduction wedges of models function of sedimentation rate $M_{0.1}^{12} - M_{0.9}^{12}$, respectively. The grey color of the markers indicate that no thermal maturity change in these sediments have not occurred. B1-B10 and C1-C10 similarly show the thermal maturity distribution in subduction wedges computed using Simple%Ro and Basin%Ro, respectively.



Formatted: No Spacing

Formatted: Font: 10 pt, English (United Kingdom), Subscript

Formatted: Font: 10 pt, English (United Kingdom), Subscript

Formatted: Font color: Auto

Formatted: Border: Top: (No border), Bottom: (No border), Left: (No border), Right: (No border), Between : (No border), Tab stops: Not at 3.13" + 6.27"

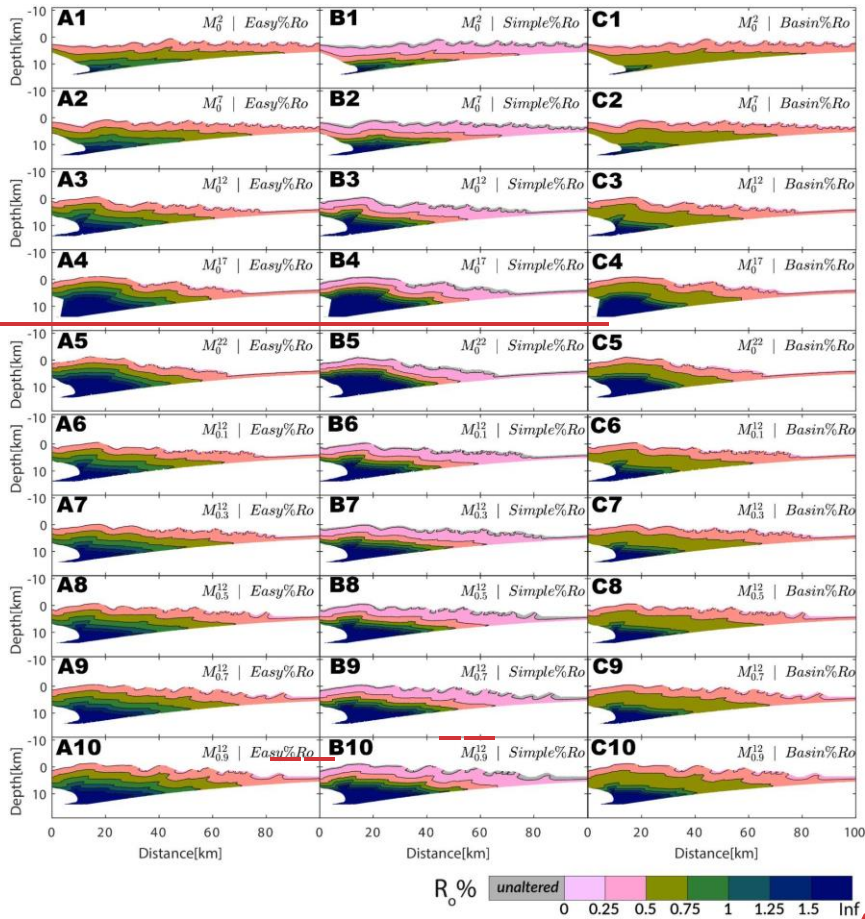


Fig. 2-4:

The variation of % R_o for ana horizon at the trench depth of each model as indicated by the orange band in the inset at 7.5

Myr. Panel **A1** and **A2** shows all the models with different decollement strength (M_0^2 , M_0^{22}) strength. Panel **B1** and **B2** shows

all the models with different sedimentation rates ($M_{0.1}^{12}$, $M_{0.9}^{12}$). Horizons in panel **A1** and **B1** are located at 1 km depth from the surface, while in panel **A2** and **B2** the horizons are horizontal zones located at the trench depth. The horizontal distance

5757

Formatted: Font: 11 pt

Formatted: Font: 10 pt, English (United Kingdom), Subscript

Formatted: No Spacing

Formatted: Font color: Auto

Formatted: Border: Top: (No border), Bottom: (No border), Left: (No border), Right: (No border), Between : (No border), Tab stops: Not at 3.13" + 6.27"

118
119

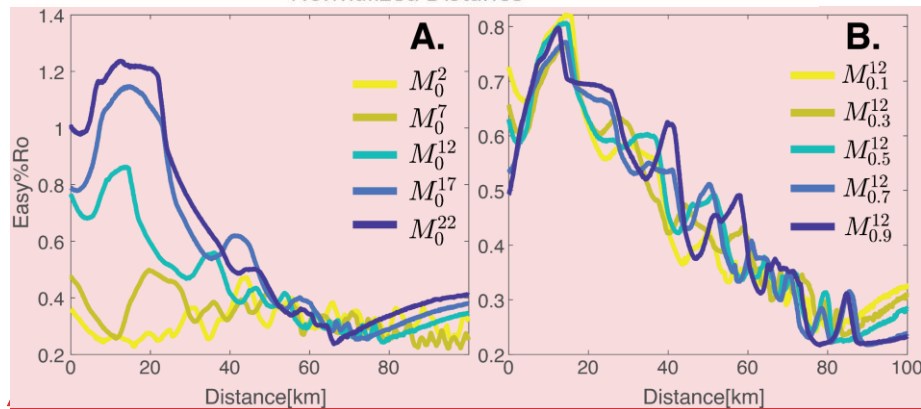
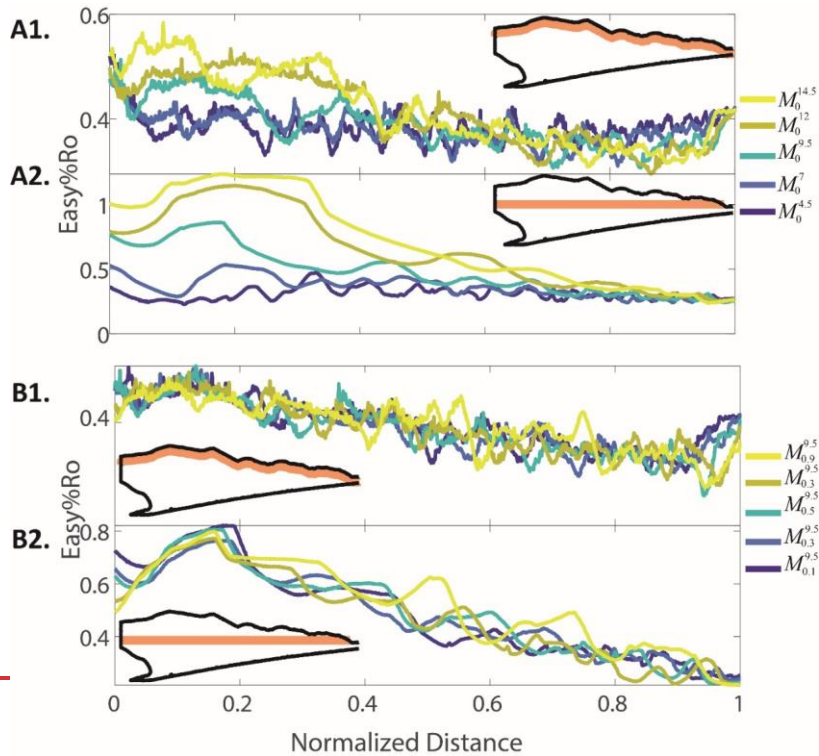
from the backstop is normalized by the wedge length. Horizontal distance 0 represents the fixed backstop and 1 represents the trench.

Commented [um57]: In Response to R2C27, R2C38

5858

Formatted: Font color: Auto

Formatted: Border: Top: (No border), Bottom: (No border), Left: (No border), Right: (No border), Between : (No border), Tab stops: Not at 3.13" + 6.27"



Commented [um58]: In Response to R2C45(Fig 4)

Formatted: Font color: Auto
Formatted: Border: Top: (No border), Bottom: (No border), Left: (No border), Right: (No border), Between : (No border), Tab stops: Not at 3.13" + 6.27"

5959

121
122
123
124
125
126
127
128
129
130
131
132

Fig. 3-5:

Map of thermal maturity at 7.5 Myr mapped to sediments at 2.5 Myr. Panel A1-A5, B1-B5 show the mapping for models M_0^{22} and $M_{0.1}^{12}$, $M_{0.9}^{12}$ respectively. The vertical axis (distance from the oceanic plate) has been corrected for the bending of the plate. The horizontal axis represents the distance of sediments from the trench. The grey colour of the markers indicates that these sediments have been eroded/reworked due to slope failure. The broken black line represents the mean $\%R_0$ attained sediment at a given distance from the trench. λ represents the horizontal periodicity in mean $\%R_0$ for the given model.

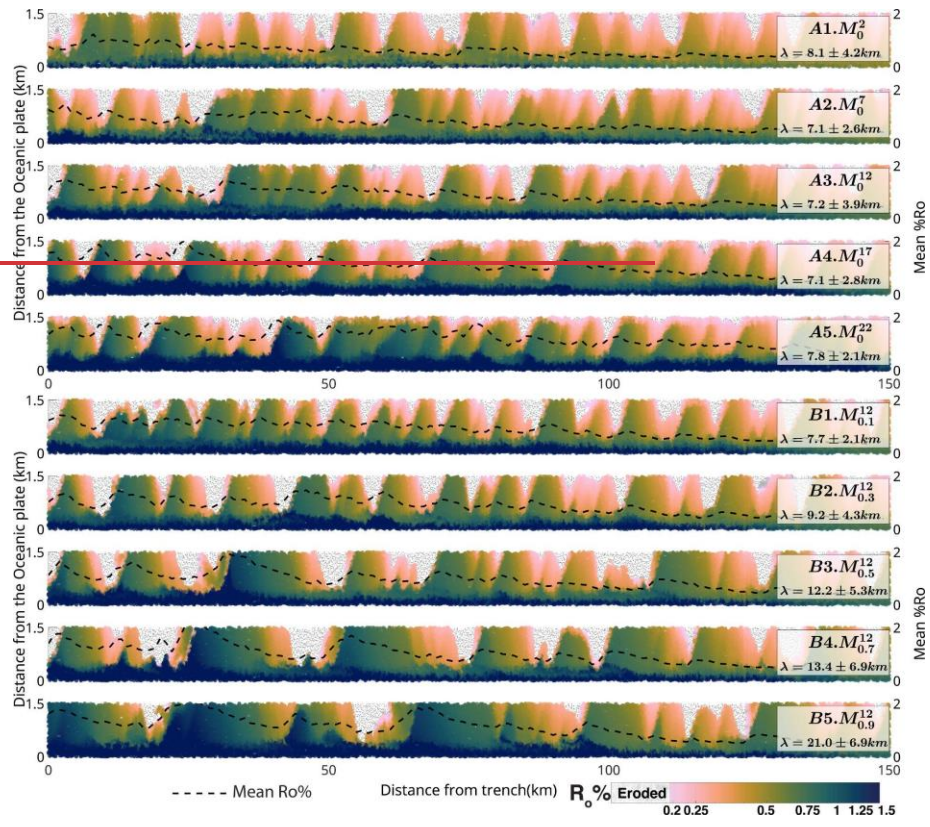
- Formatted: Space Before: 0 pt, After: 0 pt, Line spacing: single
- Formatted: Font: Bold
- Formatted: Normal
- Formatted: No Spacing

- Formatted: Font: 10 pt, English (United Kingdom), Subscript
- Formatted: Font: 10 pt, English (United Kingdom), Subscript

- Formatted: Font color: Auto
- Formatted: Border: Top: (No border), Bottom: (No border), Left: (No border), Right: (No border), Between : (No border), Tab stops: Not at 3.13" + 6.27"

6060

133



134

135

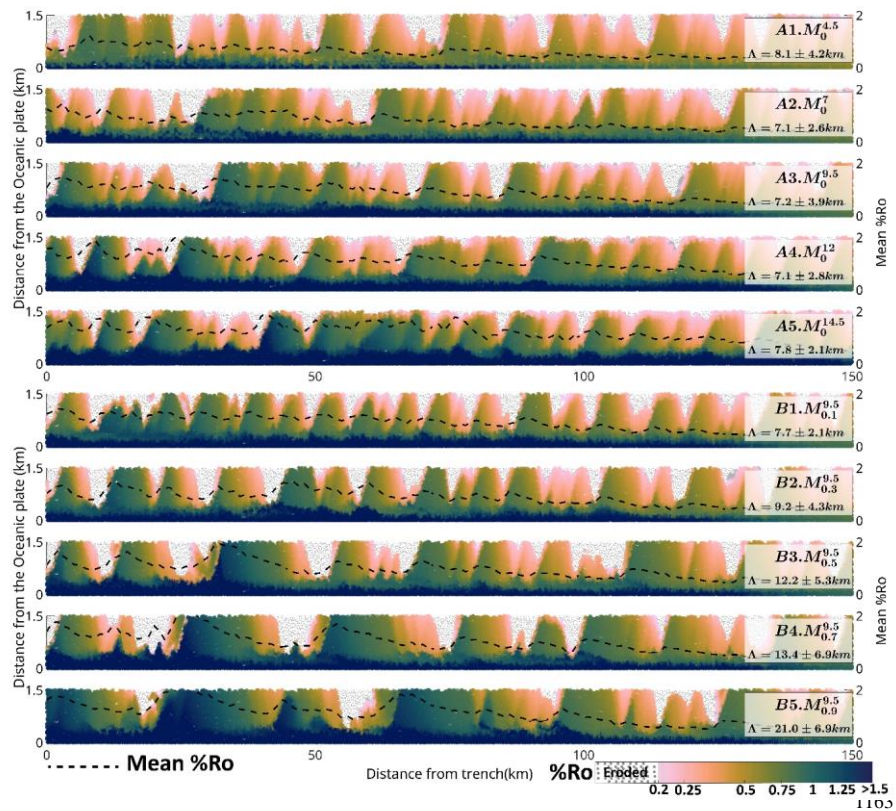
136

6461

Formatted: Font color: Auto

Formatted: Border: Top: (No border), Bottom: (No border), Left: (No border), Right: (No border), Between : (No border), Tab stops: Not at 3.13" + 6.27"

137
138



164
165

166 **Fig-4-6:**

167 A. Vitrinite Reflectance ($R_o\%$) ($\%R_o$) vs Maximum Exposure temperature in all models-B. The colours in panel A represent the
168 depth of the sediments at 7.5 Myr normalized by the thickness of the wedge (Y_n). B. Range of 95% CI for Easy%Ro, Simple%Ro
169 and Basin%Ro. Y_n is the depth of the marker from the surface normalized by the thickness (vertical extent) of the wedge at the
170 location of the marker. Please see panel B of Fig. S16 for computation of Y_n

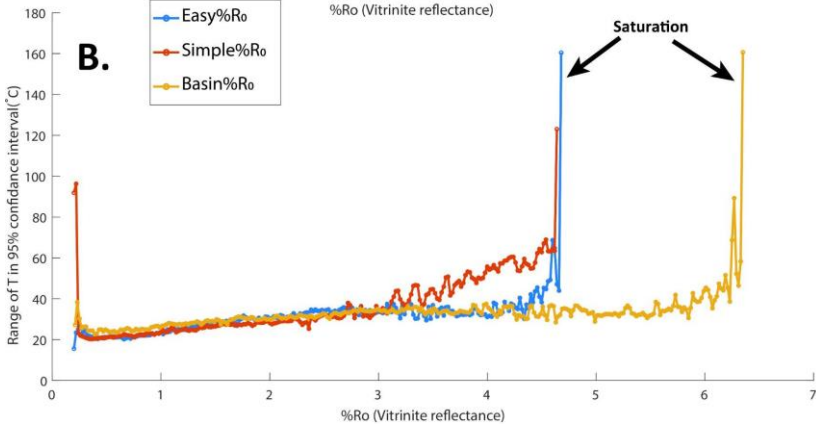
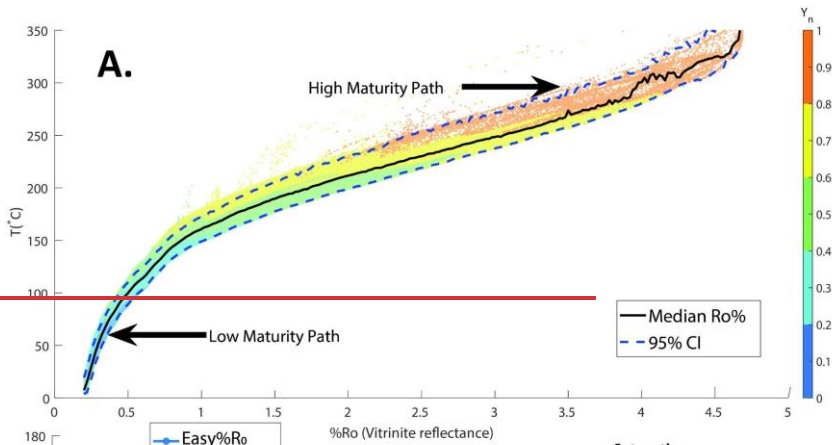
6262

Formatted: No Spacing, Line spacing: single

Commented [um59]: In Response to RIC42

Formatted: Font color: Auto

Formatted: Border: Top: (No border), Bottom: (No border), Left: (No border), Right: (No border), Between : (No border), Tab stops: Not at 3.13" + 6.27"



171

172

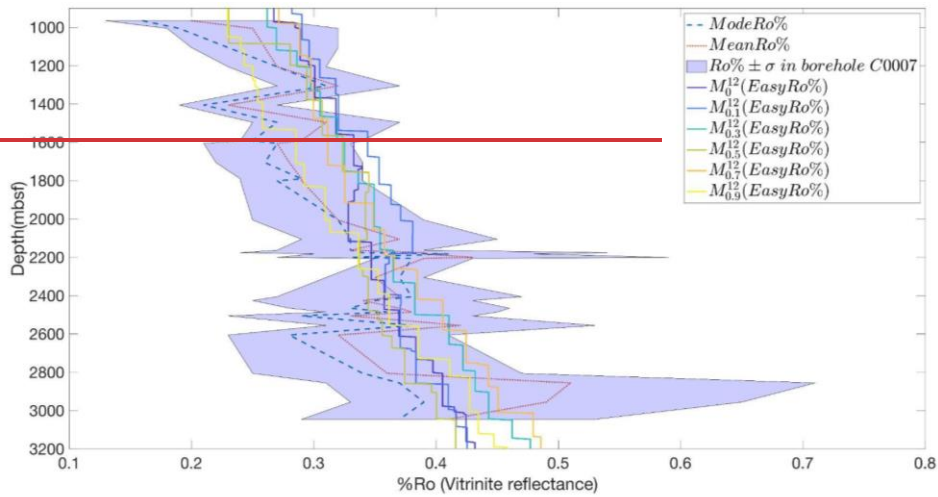
173

6363

Formatted: Font color: Auto

Formatted: Border: Top: (No border), Bottom: (No border), Left: (No border), Right: (No border), Between : (No border), Tab stops: Not at 3.13" + 6.27"

174 *Fig.5: Depth vs Thermal maturity(%Ro). The shaded (in violet) region shows the range of observed*
 175 *Ro% (mean \pm 1SD) from the C0007 borehole (Fukuchi et al., 2017), colored lines represent the thermal maturity*
 176 *values in models M_0^{12} , $M_{0.1}^{12}$, $M_{0.3}^{12}$, $M_{0.5}^{12}$, $M_{0.7}^{12}$, $M_{0.9}^{12}$ for synthetic boreholes at a distance of 20 kms from the*
 177 *seaward edge of the continental plate.*



Formatted: Font color: Auto

Formatted: Border: Top: (No border), Bottom: (No border), Left: (No border), Right: (No border), Between : (No border), Tab stops: Not at 3.13" + 6.27"

188
189
190
191
192
193
194
195
196
197
198
199
200
201
202
203

6565

Formatted: Font color: Auto
Formatted: Border: Top: (No border), Bottom: (No border), Left: (No border), Right: (No border), Between : (No border), Tab stops: Not at 3.13" + 6.27"

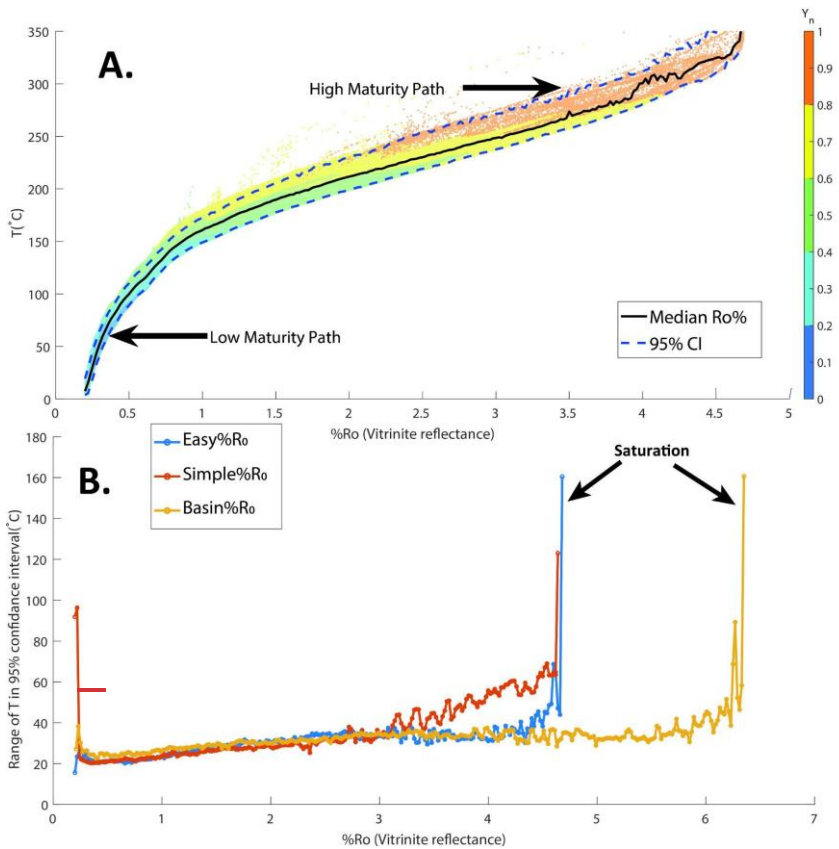


Fig. 6: Panel A7:

Mapping of eventual thermal maturity (vitrinite reflectance at 7.5Myr) to a frontal thrust the location of same markers at ~4Myr in model $M_{6.3}^{12}$. The Panel A shows the values of thermal maturity for the markers while the lithology of the wedge is shown in panel B. The half arrow represents the active frontal thrust. The sediments which were eroded by 7.5Myr but exist at 4Myr have been markers eroded using dotted grey points.

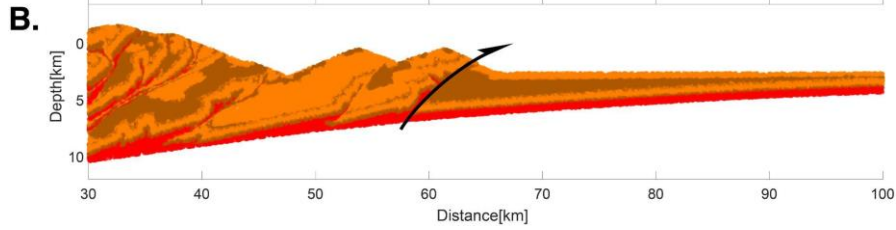
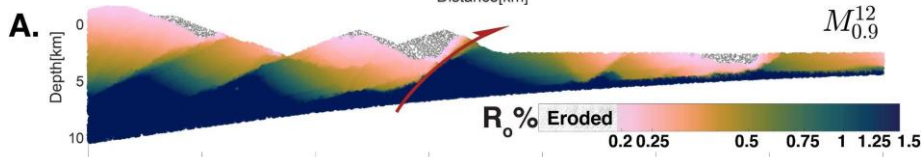
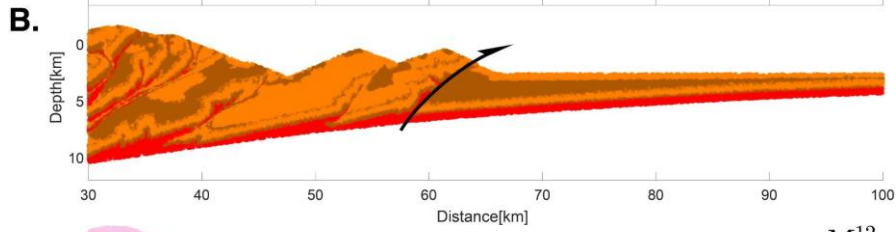
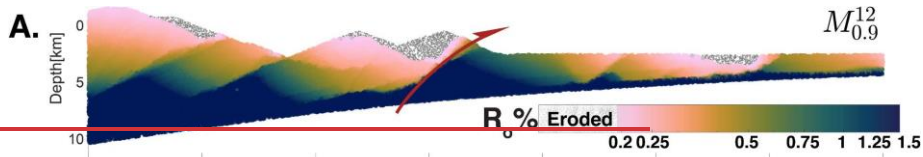
Formatted: No Spacing

Commented [um60]: In Response to R1C66

Formatted: Font color: Auto

Formatted: Border: Top: (No border), Bottom: (No border), Left: (No border), Right: (No border), Between : (No border), Tab stops: Not at 3.13" + 6.27"

6666



Formatted: Font color: Auto

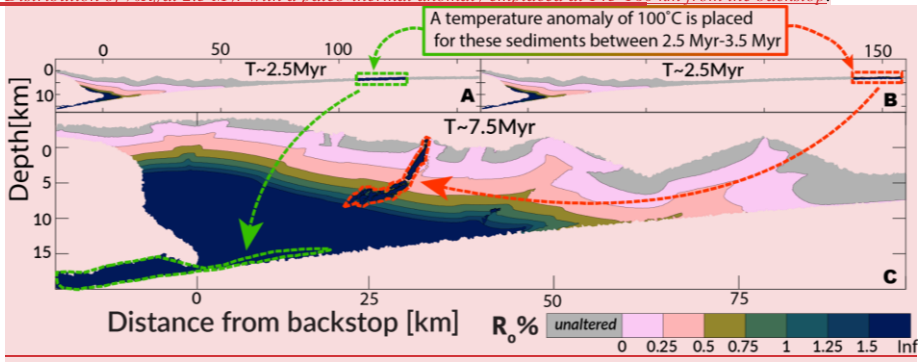
Formatted: Border: Top: (No border), Bottom: (No border), Left: (No border), Right: (No border), Between : (No border), Tab stops: Not at 3.13" + 6.27"

6767

1219
1220
1221
1222
1223
1224
1225
1226
1227
1228
1229
1230
1231
1232
1233
1234
1235
1236
1237
1238
1239
1240
1241

Fig. 7+8:

Position dependency of thermal maturity preservation. Panel A. Model state A1. Distribution of R_o at ~2.5 Myr with a paleo-thermal anomaly placed at 110-125 km from the backstop. Panel B. Model state at ~2.5 Myr with a paleo-thermal anomaly placed at 140-155 km from the backstop. Panel C. Model state at ~7.5 Myr with a paleo-thermal anomaly placed at 145-160 km from the backstop. Panel A3. Distribution of R_o at 2.5 Myr. B1. Distribution of R_o at 2.5 Myr with a paleo-thermal anomaly placed at 145-160 km from the backstop. C. Model state at ~7.5 Myr. B2. The evolution of the emplaced paleo-thermal anomaly from 2.5 Myr to 6.5 Myr in case 2. B3. Distribution of R_o at 2.5 Myr with a paleo-thermal anomaly placed at 145-160 km from the backstop.



Formatted: Font: Not Bold
Formatted: Space Before: 0 pt, After: 0 pt, Line spacing: single
Formatted: Normal

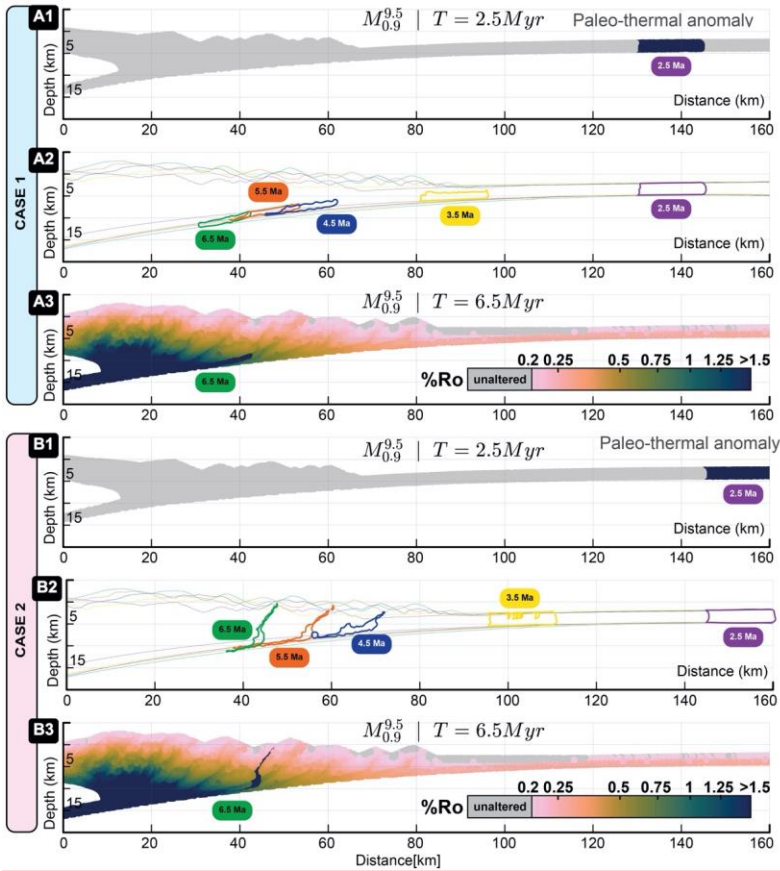
Formatted: Font: 10 pt, English (United Kingdom), Subscript
Formatted: No Spacing, Line spacing: single

Formatted: Font color: Auto
Formatted: Border: Top: (No border), Bottom: (No border), Left: (No border), Right: (No border), Between : (No border), Tab stops: Not at 3.13" + 6.27"

242
243
244
245
246
247
248
249
250
251

6969

Formatted: Font color: Auto
Formatted: Border: Top: (No border), Bottom: (No border), Left: (No border), Right: (No border), Between : (No border), Tab stops: Not at 3.13" + 6.27"



Commented [um61]: In Response to R2C14

Formatted: Font color: Auto

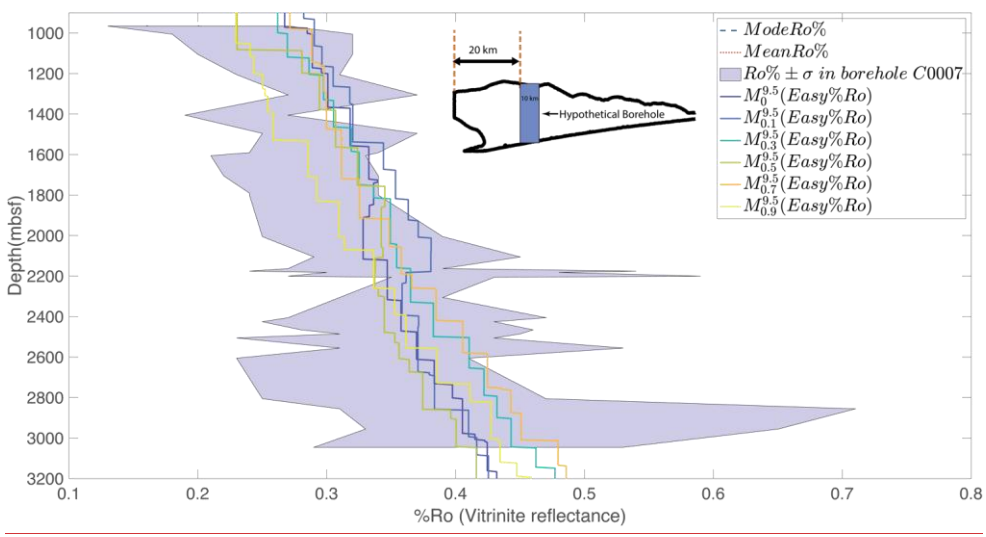
Formatted: Border: Top: (No border), Bottom: (No border), Left: (No border), Right: (No border), Between : (No border), Tab stops: Not at 3.13" + 6.27"

7070

252
253
254
255

1256
1257
1258
1259
1260

Fig. 9:
Depth vs Thermal maturity (%Ro). The shaded (in violet) region shows the range of observed Ro% (mean±1SD) from the C0002 borehole, colored lines represent the values in models sampled from a 10 km wide hypothetical borehole 20km seaward of the backstop as shown in the inset .



1261
1262
1263
1264

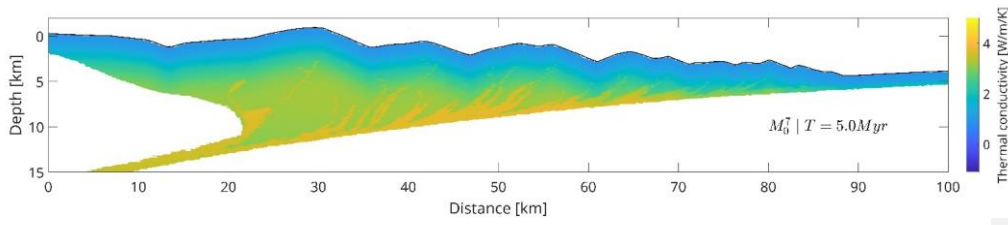
7171

Formatted: Font color: Auto
Formatted: Border: Top: (No border), Bottom: (No border), Left: (No border), Right: (No border), Between : (No border), Tab stops: Not at 3.13" + 6.27"

265 Supplementary Figures

266 Fig. S1:

267 *Typical Distribution of thermal conductivity in wedge*



Formatted: Font color: Auto

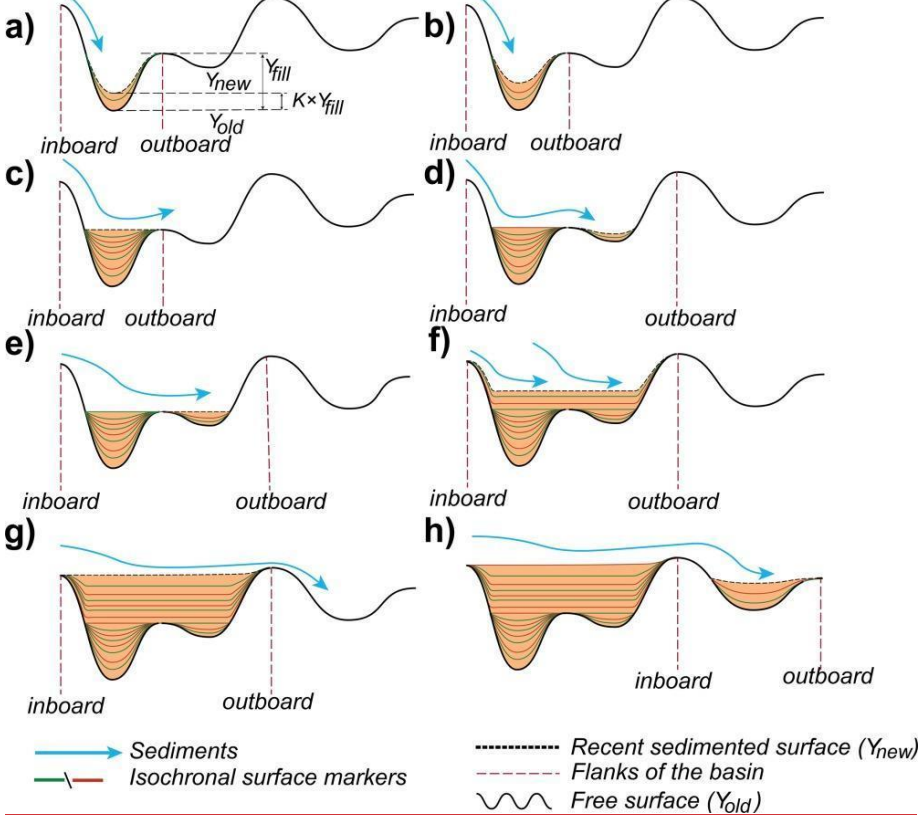
Formatted: Border: Top: (No border), Bottom: (No border), Left: (No border), Right: (No border), Between : (No border), Tab stops: Not at 3.13" + 6.27"

7272

1283
1284
1285
1286
1287
1288
1289
1290

Fig. S2:

Scheme of trench sedimentation in models (taken from (Mannu et al., 2017))

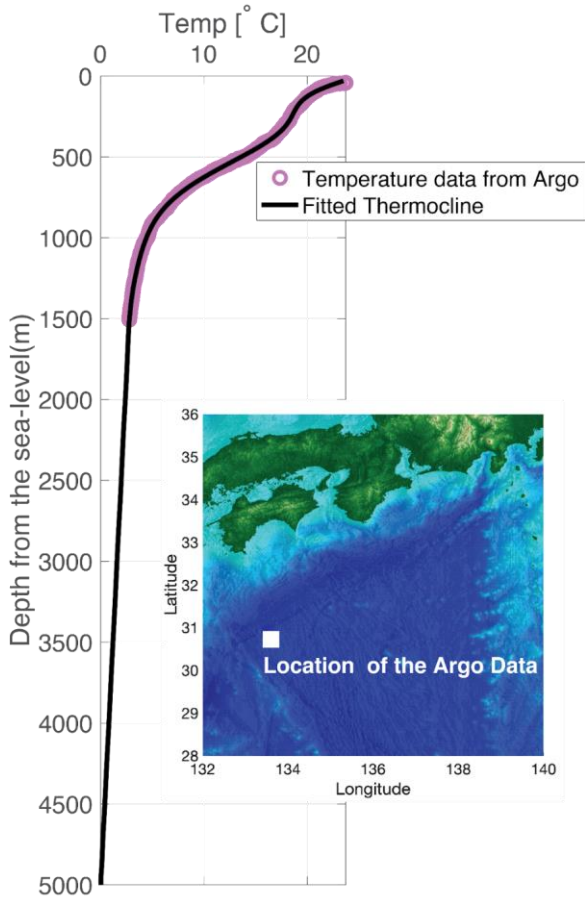


7373

Formatted: Font color: Auto
Formatted: Border: Top: (No border), Bottom: (No border), Left: (No border), Right: (No border), Between : (No border), Tab stops: Not at 3.13" + 6.27"

291 **Fig. S3:**

292 *Plot of Temperature vs Depth profile in for water-sediment interaction using the data from the International Argo Program*
293 *and the national programs that contribute for the location(represented by the white square) given in the inset The magenta*
294 *circle represents the Temperature vs Depth profile from the data while the black line is the fitted thermocline used in our*
295 *models for water-sediment thermal interaction.*
296

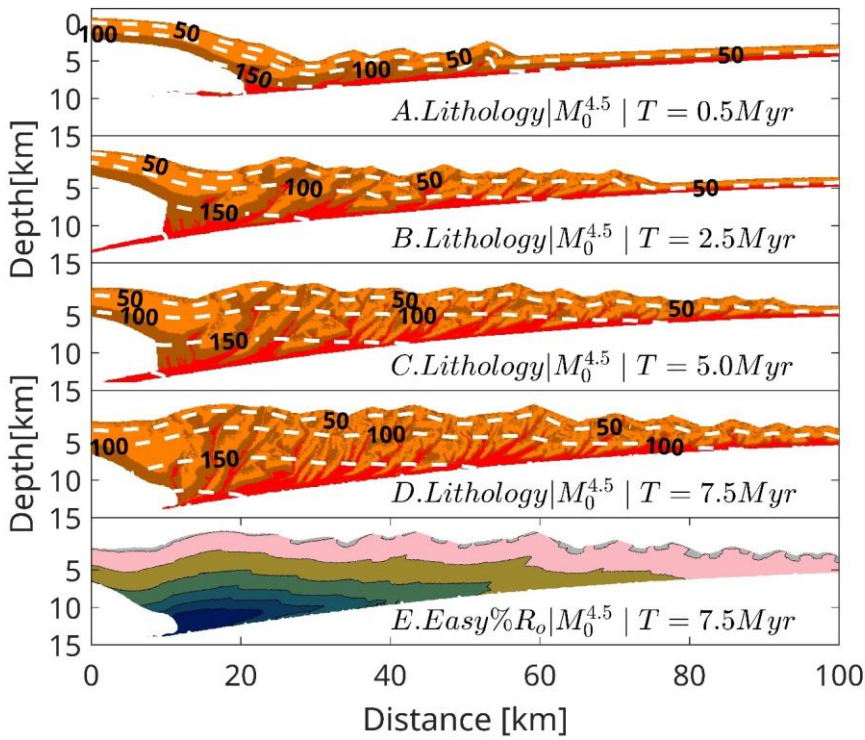


7474
Formatted: Font color: Auto

Formatted: Border: Top: (No border), Bottom: (No border), Left: (No border), Right: (No border), Between : (No border), Tab stops: Not at 3.13" + 6.27"

298 **Fig. S4:**

299 Typical thermomechanical evolution of the accretionary wedge for model $M_0^{4.5}$ at 0.5 Myr, 2.5 Myr, 5.0 Myr and 7.5 Myr of
300 lithological evolution (Panel A-D). The dashed white lines represent the contours of the temperature field. The colormap for
301 the first 4 panels is same as Figure 1. The last panel represents thermal maturity values at ~7.5 Myr computed using Easy% R_o .
302 The colormap for Panel E is same as that of Figure 3.
303



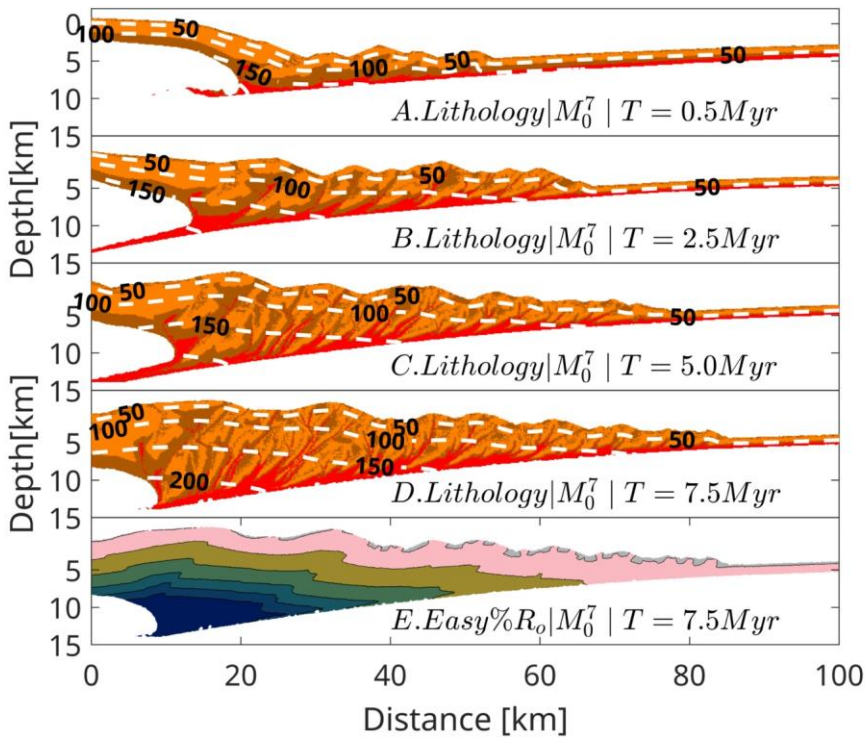
305 **Formatted:** Font color: Auto

306 **Formatted:** Border: Top: (No border), Bottom: (No
307 border), Left: (No border), Right: (No border), Between :
308 (No border), Tab stops: Not at 3.13" + 6.27"

7575

309 **Fig. S5:**

310 Typical thermomechanical evolution of the accretionary wedge for model M_0^7 at 0.5 Myr, 2.5 Myr, 5.0 Myr and 7.5 Myr of
311 lithological evolution (Panel A-D). The dashed white lines represent the contours of the temperature field. The colormap for
312 the first 4 panels is same as Figure 1. The last panel represents thermal maturity values at ~ 7.5 Myr computed using Easy% R_o .
313 The colormap for Panel E is same as that of Figure 3.



315

316

317

318

319

320

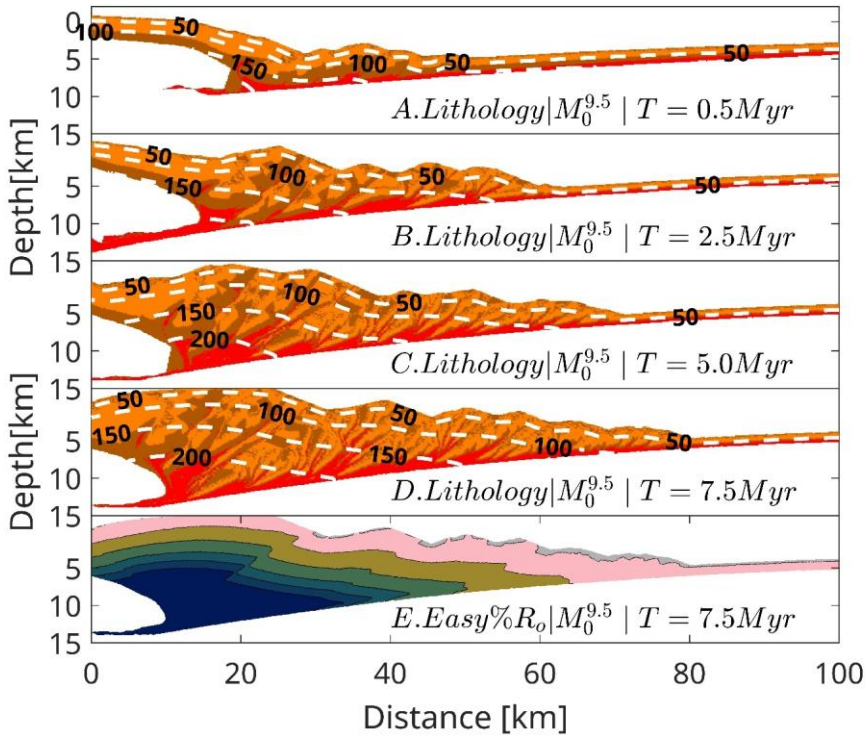
Formatted: Font color: Auto

Formatted: Border: Top: (No border), Bottom: (No border), Left: (No border), Right: (No border), Between : (No border), Tab stops: Not at 3.13" + 6.27"

7676

321 **Fig. S6:**

322 Typical thermomechanical evolution of the accretionary wedge for model $M_0^{9.5}$ at 0.5 Myr, 2.5 Myr, 5.0 Myr and 7.5 Myr of
323 lithological evolution (Panel A-D). The dashed white lines represent the contours of the temperature field. The colormap for
324 the first 4 panels is same as Figure 1. The last panel represents thermal maturity values at ~7.5 Myr computed using Easy% R_o .
325 The colormap for Panel E is same as that of Figure 3.
326



328

329

330

331

332

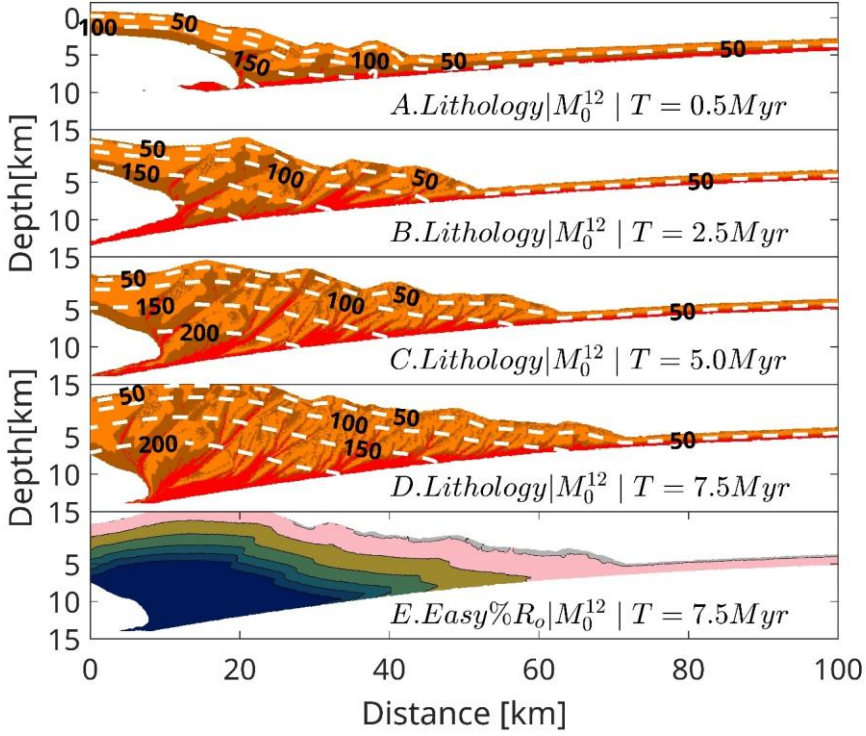
7777

Formatted: Font color: Auto

Formatted: Border: Top: (No border), Bottom: (No border), Left: (No border), Right: (No border), Between : (No border), Tab stops: Not at 3.13" + 6.27"

1333
1334
1335
1336
1337
1338
1339
1340

Fig. S7:
Typical thermomechanical evolution of the accretionary wedge for model M_0^{12} at 0.5 Myr, 2.5 Myr, 5.0 Myr and 7.5 Myr of lithological evolution (Panel A-D). The dashed white lines represent the contours of the temperature field. The colormap for the first 4 panels is same as Figure 1. The last panel represents thermal maturity values at ~7.5 Myr computed using Easy% R_o . The colormap for Panel E is same as that of Figure 3.



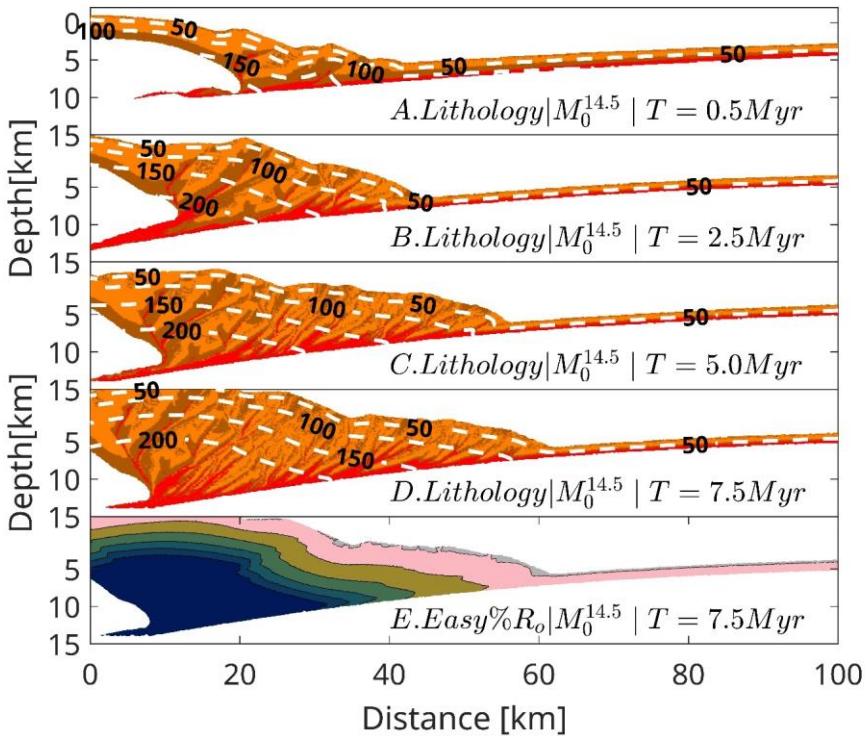
1341
1342
1343
1344

Formatted: Font color: Auto
Formatted: Border: Top: (No border), Bottom: (No border), Left: (No border), Right: (No border), Between : (No border), Tab stops: Not at 3.13" + 6.27"

7878

1345
1346
1347
1348
1349
1350
1351

Fig. S8: Typical thermomechanical evolution of the accretionary wedge for model $M_0^{14.5}$ at 0.5 Myr, 2.5 Myr, 5.0 Myr and 7.5 Myr of lithological evolution (Panel A-D). The dashed white lines represent the contours of the temperature field. The colormap for the first 4 panels is same as Figure 1. The last panel represents thermal maturity values at ~7.5 Myr computed using Easy% R_o . The colormap for Panel E is same as that of Figure 3.



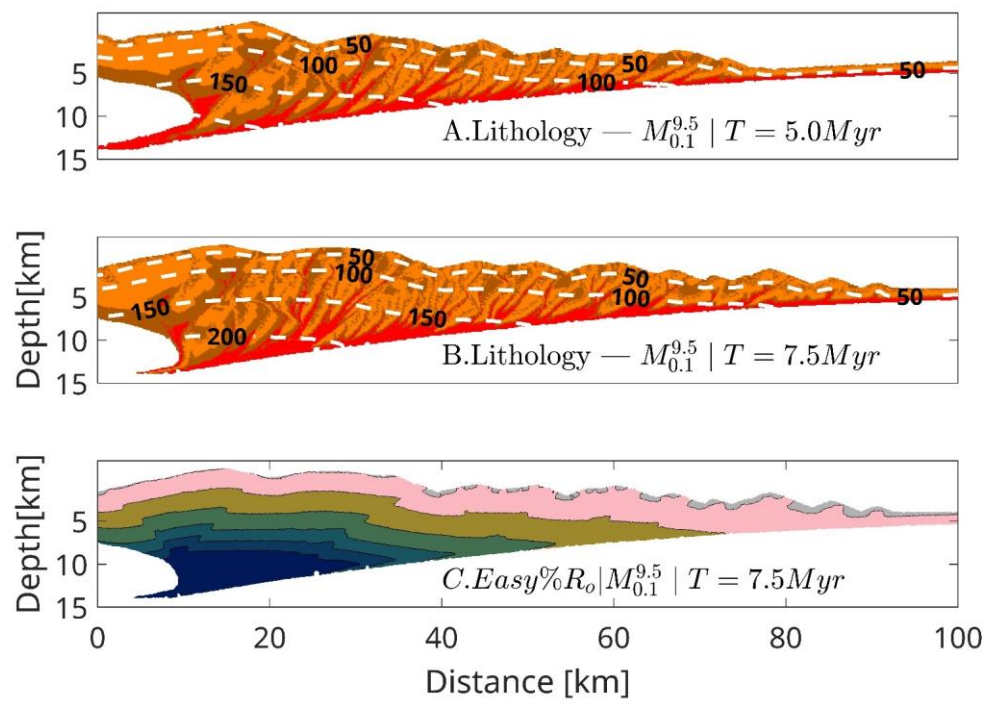
1352
1353
1354
1355

Formatted: Font color: Auto
Formatted: Border: Top: (No border), Bottom: (No border), Left: (No border), Right: (No border), Between : (No border), Tab stops: Not at 3.13" + 6.27"

7979

356
357
358
359
360
361
362
363

Fig. S9: Typical thermomechanical evolution of the accretionary wedge for model $M_{0.1}^{9.5}$ at 5.0 Myr and 7.5 Myr of lithological evolution (Panel A-B). The dashed white lines represent the contours of the temperature field. The colormap for the first 2 panels is same as Figure 1. The Panel C represents thermal maturity values at ~7.5 Myr computed using Easy%R_o. The colormap for Panel E is same as that of Figure 3.



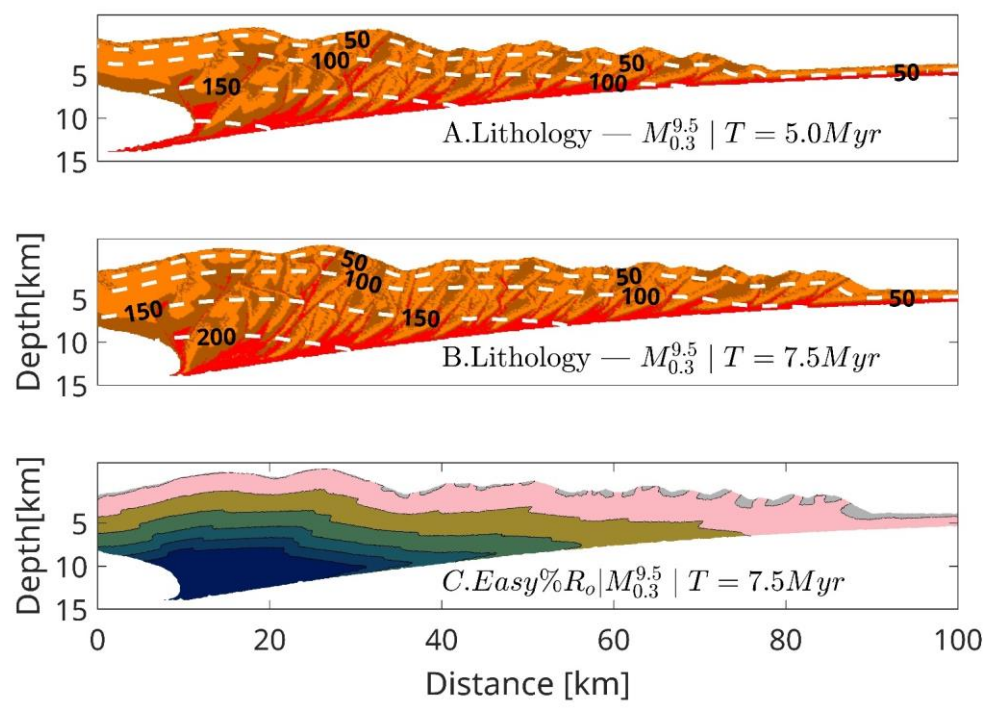
364
365
366
367

8080

Formatted: Font color: Auto
Formatted: Border: Top: (No border), Bottom: (No border), Left: (No border), Right: (No border), Between : (No border), Tab stops: Not at 3.13" + 6.27"

368
369
370
371
372
373
374
375
376
377

Fig. S10:
Typical thermomechanical evolution of the accretionary wedge for model $M_{0.3}^{9.5}$ at 5.0 Myr and 7.5 Myr of lithological evolution (Panel A-B). The dashed white lines represent the contours of the temperature field. The colormap for the first 2 panels is same as Figure 1. The Panel C represents thermal maturity values at ~7.5 Myr computed using Easy% R_o . The colormap for Panel E is same as that of Figure 3.



378
379

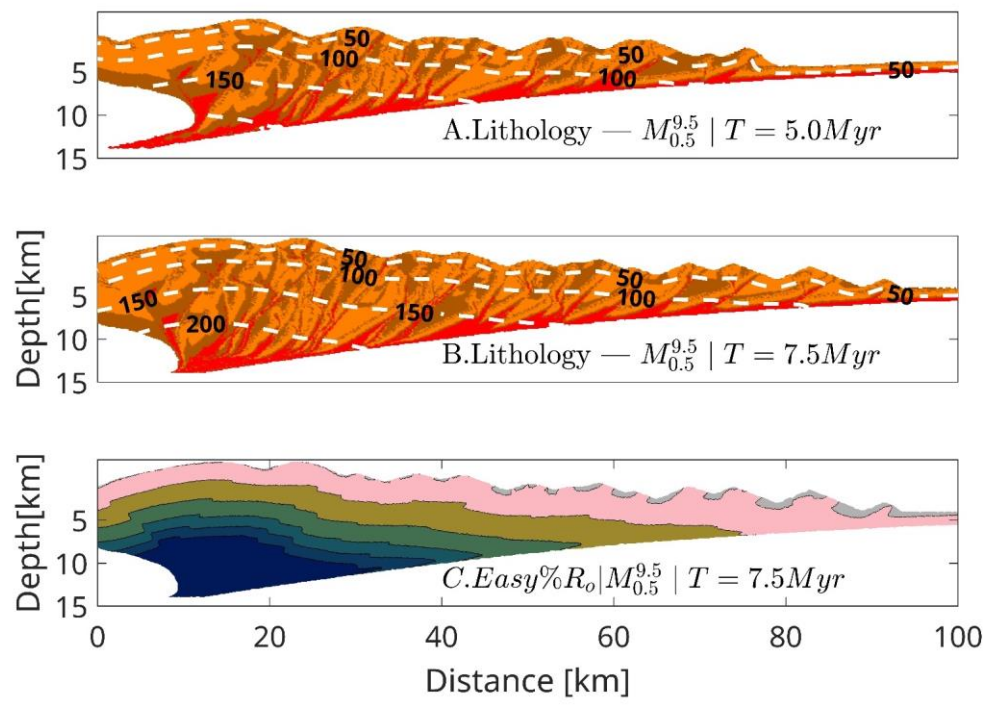
Formatted: Font color: Auto
Formatted: Border: Top: (No border), Bottom: (No border), Left: (No border), Right: (No border), Between : (No border), Tab stops: Not at 3.13" + 6.27"

8481

380
381
382
383
384
385
386
387
388
389
390

Fig. S11:

Typical thermomechanical evolution of the accretionary wedge for model $M_{0.5}^{4.5}$ at 5.0 Myr and 7.5 Myr of lithological evolution (Panel A-B). The dashed white lines represent the contours of the temperature field. The colormap for the first 2 panels is same as Figure 1. The Panel C represents thermal maturity values at ~7.5 Myr computed using Easy%Ro. The colormap for Panel E is same as that of Figure 3.



391

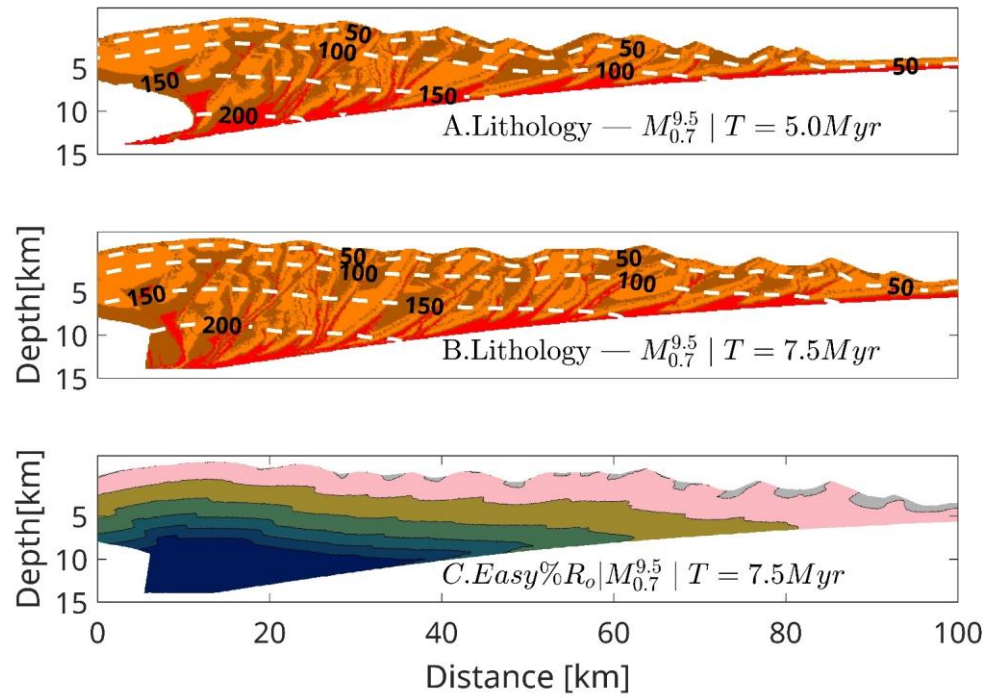
Formatted: Font color: Auto
Formatted: Border: Top: (No border), Bottom: (No border), Left: (No border), Right: (No border), Between : (No border), Tab stops: Not at 3.13" + 6.27"

8282

392
393
394
395
396
397
398
399
400
401
402

Fig. S12:

Typical thermomechanical evolution of the accretionary wedge for model $M_{0.7}^{9.5}$ at 5.0 Myr and 7.5 Myr of lithological evolution (Panel A-B). The dashed white lines represent the contours of the temperature field. The colormap for the first 2 panels is same as Figure 1. The Panel C represents thermal maturity values at ~ 7.5 Myr computed using Easy%Ro. The colormap for Panel E is same as that of Figure 3.



403

Formatted: Font color: Auto
Formatted: Border: Top: (No border), Bottom: (No border), Left: (No border), Right: (No border), Between : (No border), Tab stops: Not at 3.13" + 6.27"

8383

404
405
406
407
408
409
410
411
412
413
414
415

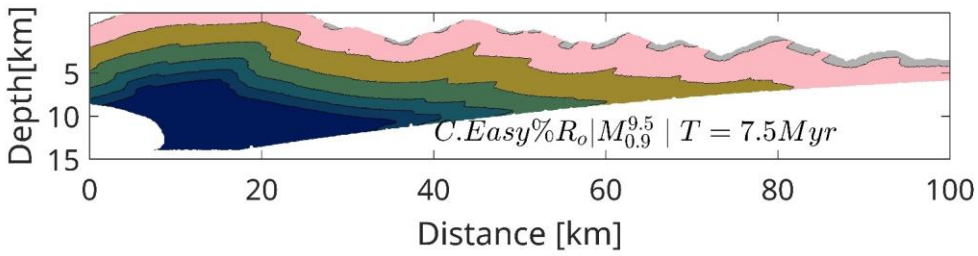
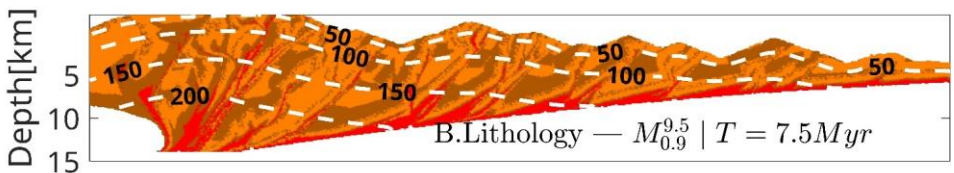
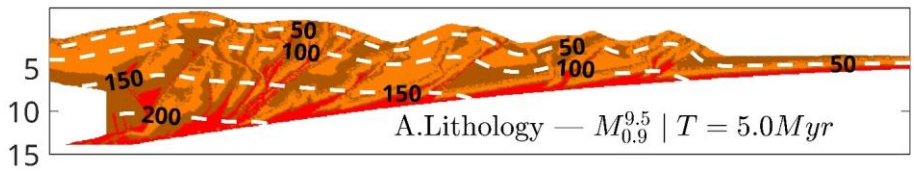
Fig. S13:

Typical thermomechanical evolution of the accretionary wedge for model $M_{0.9}^{0.5}$ at 5.0 Myr and 7.5 Myr of lithological evolution (Panel A-B). The dashed white lines represent the contours of the temperature field. The colormap for the first 2 panels is same as Figure 1. The Panel C represents thermal maturity values at ~7.5 Myr computed using Easy%R_o. The colormap for Panel E is same as that of Figure 3.

8484

Formatted: Font color: Auto
Formatted: Border: Top: (No border), Bottom: (No border), Left: (No border), Right: (No border), Between : (No border), Tab stops: Not at 3.13" + 6.27"

416



417
418
419
420
421
422
423
424
425
426

Commented [um62]: In Response to R1C34, R2C14

Formatted: Font color: Auto
Formatted: Border: Top: (No border), Bottom: (No border), Left: (No border), Right: (No border), Between : (No border), Tab stops: Not at 3.13" + 6.27"

8585

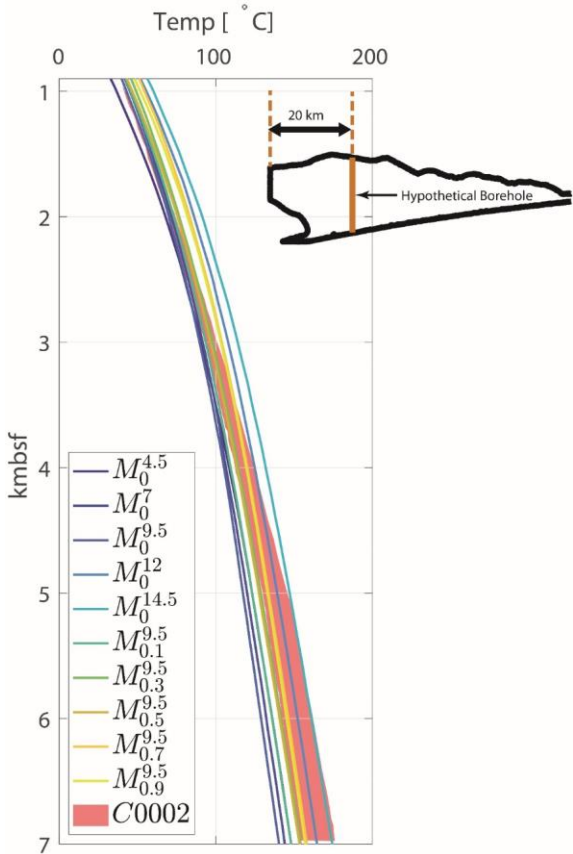
427
428
429
430
431
432
433
434
435
436
437
438
439
440
441

8686

Formatted: Font color: Auto
Formatted: Border: Top: (No border), Bottom: (No border), Left: (No border), Right: (No border), Between : (No border), Tab stops: Not at 3.13" + 6.27"

1442
1443
1444
1445
1446
1447

Fig. S14:
Plot of Temperature vs Depth profile in all models compared to Temperature-depth profile based on in-situ temperature from the long-term borehole monitoring system (indicated red patch is the range of temperature estimated by (Sugihara et al., 2014)). The temperature vs depth profiles for the models are computed for 20 kms from the backstop as shown in the inset.



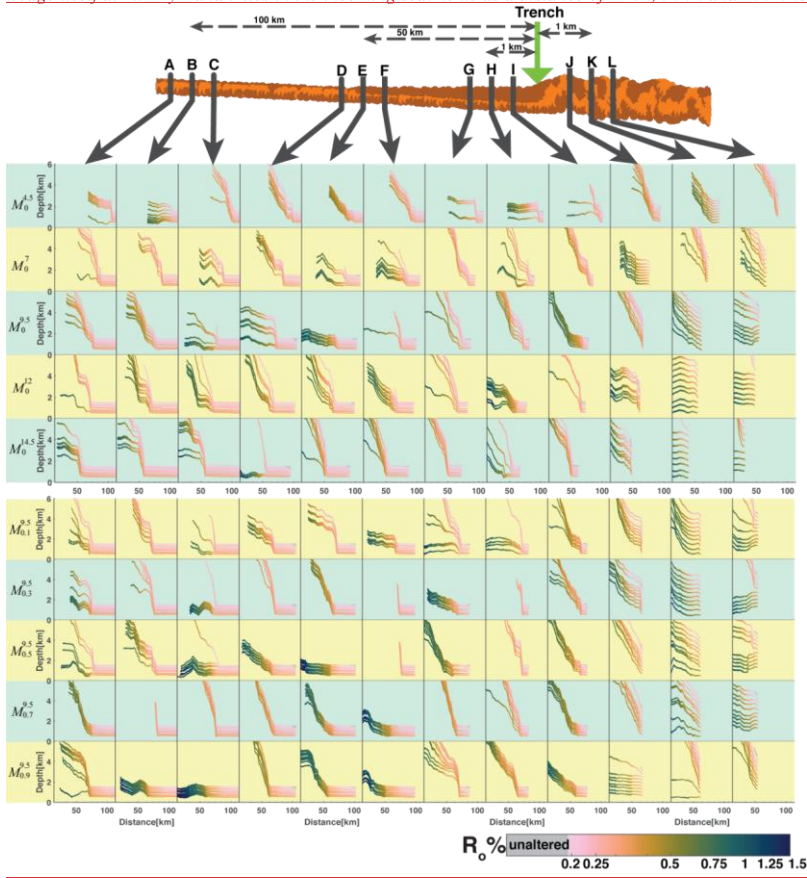
1448

8787

Formatted: Font color: Auto
Formatted: Border: Top: (No border), Bottom: (No border), Left: (No border), Right: (No border), Between : (No border), Tab stops: Not at 3.13" + 6.27"

1449 **Fig. S15**

1450 *Trajectory of sediments in model. The wedge on top shows the location of individual boreholes relative to the position of the*
1451 *trench at 2.5 Myr. In each borehole, A-L 10 points are plotted for their trajectories between 2.5 Myr and 7.5 Myr. The color*
1452 *of markers in the trajectories represent the evolution of thermal maturity on individual sediment markers while undergoing*
1453 *evolution. The image of the wedge on top is a representative image showing the relative location of boreholes with respect to*
1454 *the trench and each other. We present 4 set of boreholes (each having 3 boreholes separated by a km), one of which lies in the*
1455 *wedge itself at 2.5 Myr and 3 lies in the incoming sediments as a distance of 1 km, 50km and 100 kms from trench.*



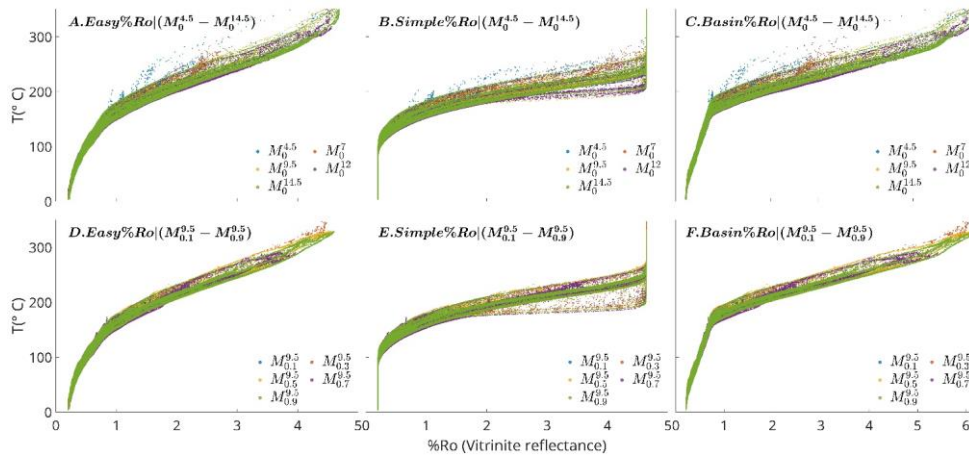
Formatted: Font color: Auto

Formatted: Border: Top: (No border), Bottom: (No border), Left: (No border), Right: (No border), Between : (No border), Tab stops: Not at 3.13" + 6.27"

8888

1458 **Fig. S16**

1459 *Vitrinite Reflectance(%R_v) vs Maximum Exposure temperature in models. Panel A, B and C show the Temperatures as a*
1460 *function of %R_v computed from Easy%R_v, Simple%R_v, Basin%R_v for models M₀^{4.5} – M₀^{14.5}. Similarly panels D, E and F show*
1461 *the Temperatures as a function of %R_v computed from Easy%R_v, Simple%R_v, Basin%R_v for models M_{0.1}^{9.5} – M_{0.9}^{9.5}.*
1462
1463



1464
1465
1466
1467
1468
1469
1470
1471
1472
1473
1474
1475
8989

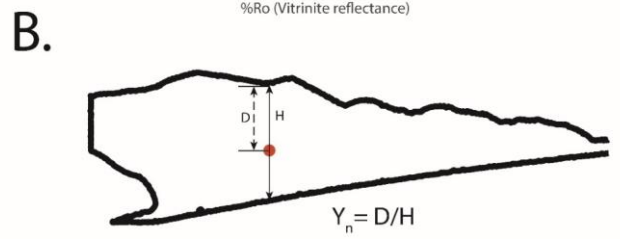
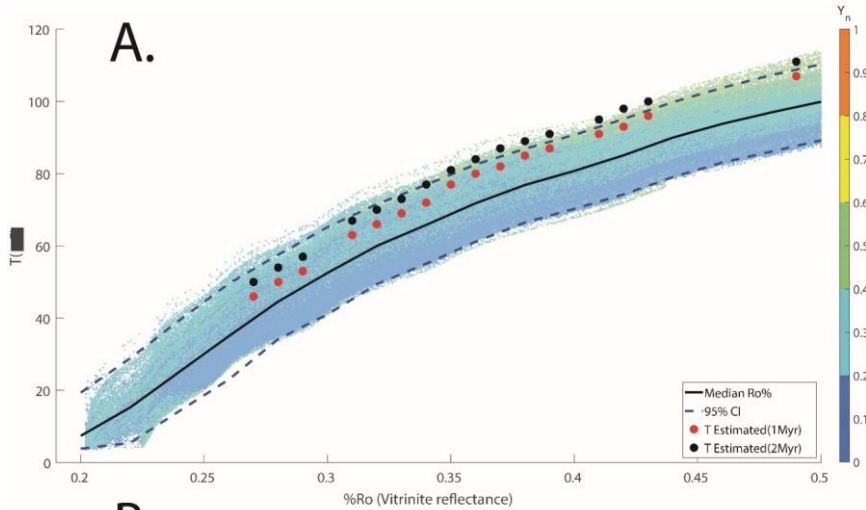
Formatted: Font color: Auto

Formatted: Border: Top: (No border), Bottom: (No border), Left: (No border), Right: (No border), Between : (No border), Tab stops: Not at 3.13" + 6.27"

1476
1477
1478
1479
1480

Fig. S17:
Panel A shows %R_v vs T for model (shown by smaller markers) and C0002 borehole (shown by large circular markers) (Fukuchi et al., 2017). Y_n is the depth of the marker from the surface normalized by the thickness (vertical extent) of the wedge at the location of the marker as illustrated in Panel B.

Commented [um63]: In Response to R1C42, R2C48, R2C49



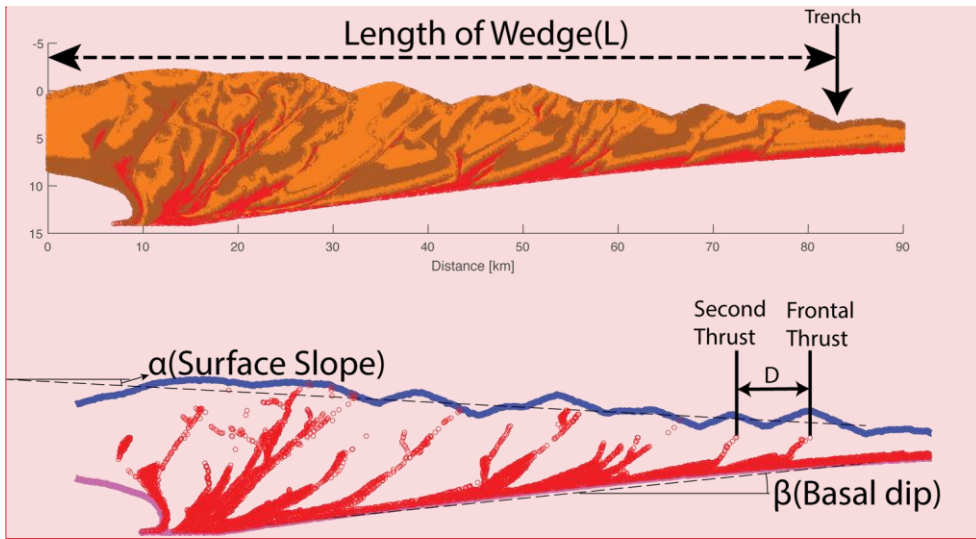
1481
1482
1483
1484
1485

9090

Formatted: Font color: Auto
Formatted: Border: Top: (No border), Bottom: (No border), Left: (No border), Right: (No border), Between : (No border), Tab stops: Not at 3.13" + 6.27"

486 **Fig. S18:**

487 Illustration to show the measurement of L (length of wedge), α (surface slope), β (basal dip) and D (Distance between the first
488 and second frontal thrust).



Commented [um64]: In Response to R1C30, R2C23

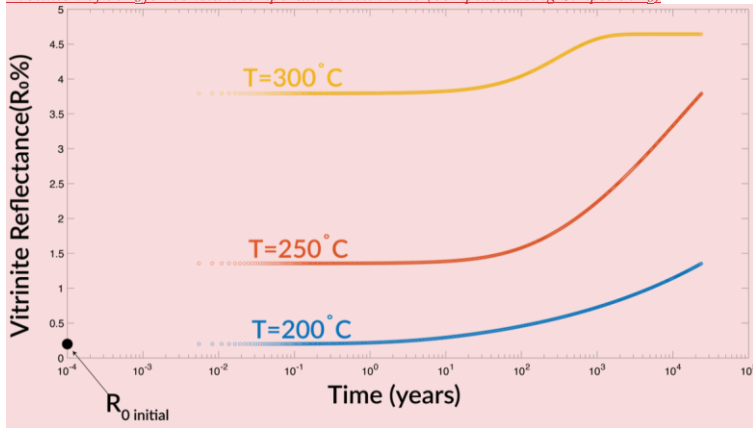
Formatted: Font color: Auto

Formatted: Border: Top: (No border), Bottom: (No border), Left: (No border), Right: (No border), Between : (No border), Tab stops: Not at 3.13" + 6.27"

9191

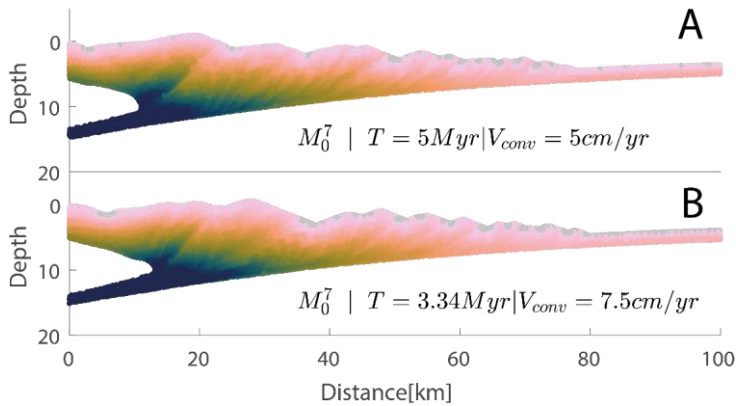
502 **Fig S19:**

503 Evolution of % R_0 for constant temperatures with time (computed using Simple % R_0)



504 **Fig S20:**

505 Thermal maturity distribution in two models with different convergent velocity. Panel A and B shows a models with convergent velocity of 5 cm/yr and 7.5 cm/yr respectively. The colormap for the images is same as for Figure 3. The comparison between the models has been shown for different time to keep the volume of incoming sediments ($T \cdot V_{conv}$) similar.



Commented [um65]: In Response to R1C43

Commented [um66]: In Response to R2C9

Formatted: Font: Not Bold, Font color: Auto

Formatted: No Spacing, Space After: 0 pt, Border: Top: (No border), Bottom: (No border), Left: (No border), Right: (No border), Between : (No border)

Formatted: Font color: Auto

Formatted: Border: Top: (No border), Bottom: (No border), Left: (No border), Right: (No border), Between : (No border), Tab stops: Not at 3.13" + 6.27"